# Paving the path between low- and high-mass star formation : dynamics probed by Herschel far-infrared spectroscopy

San Jose Garcia, I.

# 5

# *An unbiased view of the link between low- and high-mass star formation: Herschel-HIFI observations of $H_2O$ and CO from the WILL and Cygnus samples*

*I. San José-García, J. C. Mottram, S. Bontemps, et al.*
*in preparation*

## Abstract

Water line transitions uniquely trace the dynamical conditions in young stellar objects (YSOs), in particular shocks in the outflows (Kristensen et al. 2012; Mottram et al. 2014; Santangelo et al. 2014). Several *Herschel* key programmes, such as WISH, have targeted this important molecule, but their samples are a selection of peculiar sources which might not represent the general picture of the star formation process.

We aim to characterise $H_2O$ and CO line profiles as a function of luminosity (in the range 0.4 to $10^3$ $L_\odot$) for a well-selected sample of YSOs, obtained by including the WILL (low-mass) and Cygnus (intermediate-mass) follow-up programs. *Herschel*-HIFI spectra of $H_2O$ $1_{10}$-$1_{01}$, $2_{02}$-$1_{11}$, $1_{11}$-$0_{00}$, $^{12}$CO $J = 10$–9, $^{13}$CO $J = 10$–9, and C$^{18}$O $J = 9$–8 are decomposed into velocity components thought to be associated with different physical structures within protostellar systems, such as shocked gas along the outflow cavity wall, entrained outflowing material and the quiescent envelope. For each line, the widths, peak velocities and luminosities are calculated.

Following the methods used on the WISH sample, all water transitions for each WILL or Cygnus source are decomposed into the same component types. However, while in the WILL sample we detect three types of velocity components, corresponding to quiescent envelope, cavity shocks and spot shocks, for the Cygnus sample only the envelope and the cavity shocks are identified. We exclude that the absence of spot shock components in the Cygnus sample is due to insufficient *S/N*. Instead, the Cygnus sources are either in a later evolutionary stage or the emission is beam diluted due to their large distances.

For both WILL and Cygnus, more than 80% of the water emission comes from shocked material along the outflow cavity. While for the WILL Class 0 sample the rest of the emission belongs to spot shocks, for the WILL Class I and Cygnus sample this remaining emission is mostly generated by the envelope, consistent with previous analysis on the WISH sample. The percentage of WILL Class 0 sources for which a broad component is detected in the $^{12}$CO $J = 10$–9 line profiles is lower than for WISH low-mass Class 0 sources (42% versus 72% of the detected spectra) and the width of this component is generally narrower (by $\sim$5 km s$^{-1}$) for the WILL Class 0 protostars. While the *FWZI* of the 557 GHz water line is similar for both WILL and WISH Class 0 objects, the other transitions show narrower *FWZI* values for the WILL sources. These results suggest that the WISH Class 0 sub-sample contains sources with more energetic outflows. In contrast, the intrinsic properties of Class I sources seem more uniform across the two samples.

Based on the similarity of the line properties between the WISH and Cygnus samples, we suggest that the latter is mostly composed of Class I low- and intermediate-mass YSOs. Finally, a strong correlation is measured between the luminosity of all studied lines and the bolometric luminosity of the source. The implications of this correlation are currently under investigation. Therefore, apart from minor differences between the intrinsic properties of the YSOs constituting the studied surveys, overall the conclusions derived from WISH hold and are confirmed by the $H_2O$ and CO observations of the WILL and Cygnus samples.

# 5.1. Introduction

In previous chapters we investigated the physical properties of the sample of embedded young stellar objects (YSOs) constituting the "Water In Star forming regions with *Herschel*" (WISH; van Dishoeck et al. 2011) key programme. The ultimate purpose is to derive a comprehensive picture of the star formation process without mass boundaries, focusing on comparing the dynamical conditions in the warm inner regions of the protostellar environments of low-, intermediate- and high-mass YSOs.

The YSOs within the WISH sample were selected because they have been well studied. They are usually bright or somehow peculiar sources with unusual and unique properties and so may not be representative of the global conditions where stars form. Even if the characterisation of these types of objects is an important step towards the understanding of the star formation process, it is crucial to build a more unbiased sample of YSOs to test the acquired knowledge of the physics of protostellar systems without being dominated by the specific properties of outliers in the sample.

In addition, the WISH survey is composed of a relatively small number of YSOs, of the order of 50 in total, and much less if distinctions between mass and evolutionary stages are made. Therefore, a larger and more varied sample of YSOs will allow us to interpret the outcomes in a more solid and statistically supported framework.

Finally, the aim of this work is to investigate whether massive star-forming regions can be considered scaled-up versions of low-mass protostars. Within this context, intermediate-mass sources play a pivotal role in bridging the gap between low- and high-mass YSOs. These objects share many properties with their less and more massive counterparts, from both the theoretical and observational point of view. However, the WISH survey only included six intermediate-mass YSOs, leaving the range of bolometric luminosities between few $10^2$ to $10^4$ $L_\odot$ largely unsampled.

In order to strengthen the study initiated by the WISH key programme on the characterisation of star formation as a function of luminosity (San José-García et al. 2013, & subm., Karska et al. 2014a, Benz et al. subm.], the data from two *Herschel* follow-up projects are analysed in this chapter. The aim is not only to extend the sample of studied YSOs, but also validate previous results with a larger statistical base and complement the WISH survey by overcoming the weaknesses described above.

The first of the two follow-up projects is "The William Herschel Line Legacy" survey (WILL; PI.: E. F. van Dishoeck). This programme targeted 45 embedded low-mass Class 0/I protostars selected from photometric surveys with *Spitzer* and *Herschel* of major star-forming regions located within 450 pc. The luminosities of sources in this sample range from 0.4 to ∼30 $L_\odot$. Further information about the WILL survey such as selection criteria (infrared slope, bolometric temperature), observed lines and follow-up ground-based JCMT and APEX observations is presented in Mottram et al. in prep.

The second *Herschel* follow-up programme is titled "Water emission from outflows and hot cores in the Cygnus X protostars" (PI: S. Bontemps). It targets the Cygnus X star-forming region, which is more distant (∼1.4 kpc) and massive (total molecular mass of $3{\times}10^6$ $M_\odot$; Schneider et al. 2006) than those targeted in WILL. It contains multiple OB associations (Comerón & Pasquali 2012, and references therein) and several massive YSOs (Motte et al. 2007; Reipurth & Schneider 2008). This project selected the 86 most luminous embedded YSOs in Cygnus by combining the results from the *Spitzer* Cygnus X Legacy Survey (PI.: J. Hora) and the IRAM MAMBO2 survey (Motte et al. 2007) in order to observe intermediate- and high-mass Class 0- and Class I-type objects. The sample covers a range of bolometric luminosities between $10^2$ to $10^3$ $L_\odot$ (preliminary $L_{\rm bol}$ values taken from Kryukova et al. 2014) and complements the interval of luminosities poorly represented by WISH. One of the goals of this programme is to investigate the outflow energetics and explore chemically rich protostars, for which water plays a key role. Information about the survey, its goal, sample and line selection are discussed in Bontemps et al. in prep. Taken together, Cygnus X not only constitutes an ideal laboratory of embedded low-, intermediate- and high-mass sources linked by their likely common origin, but also satisfies the requirement to create a comprehensive sample of YSOs together with the WISH and WILL surveys. Finally, this survey allows a deeper analysis of the protostellar conditions by removing any possible bias related to

source distance (Malmquist bias) since all observed Cygnus YSOs are located at similar distances.

The importance of defining a complete sample of YSOs goes together with selecting appropriate molecular tracers to characterise the specific physical and chemical conditions of YSO environments. As discussed in chapter 4, the energetics and dynamics of molecular outflows, which are critical in the formation of young stars, are unambiguously probed by water emission (van Dishoeck et al. 2011). The Heterodyne Instrument for the Far-Infrared (HIFI; de Graauw et al. 2010) on board of the *Herschel* Space Observatory (Pilbratt et al. 2010) provides velocity-resolved water spectra with unprecedented spectral resolution, probing the excitation and kinematics of the gas. Complementing the analysis of the water emission, mid-$J$ ($J \leq 10$) $^{12}$CO, $^{13}$CO and C$^{18}$O observations help to create a more complete picture of the dynamical structure of protostellar environments, since these species probe entrained outflowing material and the quiescent warm inner envelope (see chapter 2 and 3).

Therefore, the aim of this work is to investigate whether the dynamics of outflows vary as a function of luminosity by comparing the water and CO emission of a large, unbiased sample of low-, intermediate- and high-mass YSOs. In addition, the results derived from WISH (San José-García et al. 2013, & subm., Mottram et al. 2014) will be tested in the context of the WILL and Cygnus surveys to confirm the statistical significance of these conclusion within a more uniform framework.

In Sect. 5.2, the sample and line selection as well as the reduction and decomposition methods applied to the HIFI data are described. The results from the basic analysis of the water and CO observations for the WILL and Cygnus YSOs are presented in Sect. 5.3. In addition, the outcomes are compared to those obtained from the WISH survey, in particular those regarding the dynamical structure of molecular outflows. The implications of these outcomes and a more throughout study of the Cygnus X environment are discussed in Sect 5.4. Finally, the conclusions are summarised in Sect. 5.5.

## 5.2. Observations

### 5.2.1. Sample

The entire sample of sources presented in this chapter is composed of 131 YSOs. For the WILL survey, the 24 Class 0 and 21 Class I protostars are located in several well-known low-mass star-forming regions such as Perseus, Taurus, Ophiucus, Scorpius and Serpens. These targets have an infrared index, $\alpha$, above 0.3 and bolometric temperatures, $T_{\rm bol}$, smaller than 350 K. This latter parameter is used to distinguish between the two evolutionary stages: sources with $T_{\rm bol}$<70 K are classified as Class 0 and those with larger values as Class I protostars. The velocities of the WILL sources with respect the standard of rest, $v_{\rm LSR}$, have been determined with C$^{18}$O and C$^{17}$O low-$J$ lines observed with the JCMT (Mottram et al. in prep.).

In the case of the Cygnus sample, 8 of the 86 sources can be considered equivalent to low-mass Class 0 protostars and the remaining 78 are more evolved objects (Class I and II type with no radio emission). The division between these two stages and their analogy with those of low-mass YSOs is based on their infrared colours and the spectral energy distribution (SED) type of the Cygnus objects. Their bolometric luminosity is taken from Kryukova et al. (2014) or Motte et al. (2007) when the *Spitzer* emission was saturated. Therefore, both the rough evolutionary classification and their $L_{\rm bol}$ values are preliminary and will be constrained with complementary techniques in future work. In particular, $L_{\rm bol}$ will be re-calculated from more complete SEDs including *Herschel* PACS and SPIRE flux densities. Finally, the source velocity, $v_{\rm LSR}$, of several Cygnus YSOs has been taken to be that of the C$^{18}$O $J = 9$–8 line. If this transition was not detected, $^{13}$CO $J = 10$–9 was used. This means that $v_{\rm LSR}$ could be determined for only a sub-sample of observed Cygnus YSOs. The $v_{\rm LSR}$ values are found to cover four main velocity ranges: one around -5 km s$^{-1}$ and the others between 2 and 20 km s$^{-1}$, consistent with the results of Schneider et al. (2006). In that paper, the authors discussed the presence of structures in the North cloud of Cygnus with different $v_{\rm LSR}$ and located in the same line of sight. Further information about the source properties and the criteria

Table 5.1: Properties of the studied lines observed with HIFI.

| Species | Transition | Freq.[a] | $E_u/k_b$ | $n_{cr}$ | $\eta_{mb}$[b] | $\theta_{mb}$[b] | WBS res. | Observation Time[c] | | | |
|---|---|---|---|---|---|---|---|---|---|---|---|
| | | | | | | | | WILL | Cygnus | W LM | W HM |
| | | (GHz) | (K) | ($cm^{-3}$) | | ($''$) | (km $s^{-1}$) | (min) | (min) | (min) | (min) |
| o-$H_2O$ | $1_{10}$-$1_{01}$ | 556.9 | 61.0 | $1\times10^7$ | 0.62 | 38.1 | 0.27 | 38 | – | 21 | – |
| | $3_{12}$-$2_{21}$ | 1153.1 | 249.4 | $8\times10^6$ | 0.59 | 18.4 | 0.13 | 13 | – | 13 | |
| p-$H_2O$ | $1_{11}$-$0_{00}$ | 1113.3 | 53.4 | $1\times10^8$ | 0.64 | 19.0 | 0.13 | 28 | 9 | 44 | 7 |
| | $2_{02}$-$1_{11}$ | 987.9 | 100.8 | $4\times10^7$ | 0.64 | 21.5 | 0.15 | 36 | 9 | 23 | 12 |
| o-$H_2^{18}O$ | $1_{10}$-$1_{01}$ | 547.7 | 60.5 | $1\times10^7$ | 0.62 | 38.7 | 0.27 | 38 | – | 33 | – |
| $C^{18}O$ | 9–8 | 987.6 | 237.0 | $2\times10^5$ | 0.64 | 21.5 | 0.15 | 36 | 9 | 23 | 12 |
| $^{13}CO$ | 10–9 | 1101.3 | 290.8 | $3\times10^5$ | 0.64 | 19.3 | 0.13 | 28 | 9 | 44 | 59 |
| $^{12}CO$ | 10–9 | 1151.9 | 304.2 | $3\times10^5$ | 0.59 | 18.4 | 0.13 | 13 | – | 10 | 20 |

**Notes.** W LM stands for WISH low-mass protostars and W HM for WISH high-mass YSOs.
[a] Rest frequency taken from the JPL database (Pickett et al. 2010). [b] Values recently updated and provided by the HIFI wikipage[1], which replace those presented in Roelfsema et al. (2012). [c] Total observation time including on+off source and overheads.

on the selection will be presented in Bontemps et al. in prep.

To summarise, the composed sample of low-, intermediate- and high-mass YSOs covers a range of luminosities between 0.4 to $10^3$ $L_\odot$, filling the gap between $10^2$ and $10^3$ $L_\odot$ left by the WISH sample. In addition, the statistics of the analysis is improved due to the increase of the number of available objects by a factor of two. As in previous chapters, the study is focused on characterising the physical properties of YSO systems across the luminosity range. More detailed analysis based on the different evolutionary stages for each luminosity bin will be presented in Mottram et al. in prep. for the WILL sample, in Bontemps et al. in prep. for the Cygnus YSOs.

## 5.2.2. HIFI observations

Water was the primary targeted molecule for both WILL and Cygnus X surveys, but the selected HIFI settings serendipitously covered some CO transitions. For WILL, the para-$H_2O$ $1_{11}$-$0_{00}$ (1113 GHz) and $2_{02}$-$1_{11}$(988 GHz); the ortho-$H_2O$ $1_{10}$-$1_{01}$ (557 GHz) and $3_{12}$-$2_{21}$ (1153 GHz); and the ortho-$H_2^{18}O$ $1_{10}$-$1_{01}$ (548 GHz) transitions were observed as well as $^{12}CO$ $J = 10$–9, $^{13}CO$ $J = 10$–9 and $C^{18}O$ $J = 9$–8. Within the Cygnus program, the three brightest water transitions were selected after taking into account the first WISH results (see e.g. Chavarría et al. 2010; Kristensen et al. 2010; Marseille et al. 2010). In this work we present the para-$H_2O$ $1_{11}$-$0_{00}$ (1113 GHz) and $2_{02}$-$1_{11}$(988 GHz) transitions and $^{13}CO$ $J = 10$–9, $C^{18}O$ $J = 9$–8, observed together, as for the WILL sample.

Table 5.1 shows the rest frequency, upper energy level ($E_u$), critical density ($n_{cr}$) of each line together with the beam efficiency ($\eta_{mb}$), beam size ($\theta_{mb}$), spectral resolution of each HIFI line and observing time. The beam efficiencies of each HIFI band have been recently updated and the adopted values are those provided by the HIFI wikipage[1]. The observation times of the WISH low-mass and high-mass YSOs are also included in Table 5.1 for comparison. Since the WILL sources are generally fainter than their WISH analogues, the exposure times were increased for WILL in order to get similar signal-to-noise ratios, $S/N$=$T_{peak}/\sigma_{rms}$. While comprable rms values are achieved for both WILL and WISH low-mass samples, WILL observations generally show lower $S/N$ than those of WISH. This difference is not significant for the 557 GHz water line, for which the averaged $S/N$ is ∼20 and ∼26 for the WILL and WISH low-mass samples respectively. However, for the 1113 GHz line there is a factor of ∼2 difference in $S/N$ between the two samples. The

[1]Further information regarding the updated beam efficiencies values is presented in the technical note "Measured beam efficiencies on Mars (revision v1.1, 1 October 2014)" of the HIFI wikipage:
http://herschel.esac.esa.int/twiki/bin/view/Public/HifiCalibrationWeb? template=viewprint

integration time for the Cygnus objects was selected with the purpose of achieving a 5$\sigma$ detection of the $H_2O$ lines for a source such as NGC 7129 FIRS2 (part of the WISH intermediate-mass subsample) but located at 1.3 kpc. The achieved *S/N* on sources where the lines are detected is similar to that of the WISH intermediate-mass YSOs (*S/N*~47) and only slightly lower than that obtained for the WISH high-mass objects (*S/N*~60). This difference is less relevant given the overall higher *S/N* of the Cygnus sample.

As for previous HIFI observations (see Sections 2.2.2 and 4.2.2), the data were taken with the Wide Band Spectrometer (WBS) and the High Resolution Spectrometer (HRS) backends, in both vertical (V) and horizontal (H) polarisations (Roelfsema et al. 2012). We present the WBS observations because they have the best compromise between noise and resolution, especially for the studied molecular lines. For all targets, single-pointing observations were performed in dual-beam-switch (DBS) mode.

### 5.2.3. Reduction of the HIFI data

The applied reduction process is the same as that explained in Sections 2.2.2 and 4.2.5 of previous chapters. All HIFI observations were calibrated using the *Herschel* Interactive Processing Environment (HIPE[2]; Ott 2010). The flux was converted to the antenna temperature $T_A^*$ scale and the velocity calibrated with a $v_{\rm LSR}$ precision of a few m s$^{-1}$, after which the data were exported to GILDAS-CLASS[3] format for further analysis. The signal-to-noise ratio of the spectra was improved by averaging together the observations of the H and V polarisations. Then, the line intensities were converted to main-beam brightness temperatures, $T_{\rm MB}$, applying the specific beam efficiencies, $\eta_{\rm MB}$, of each HIFI band. Finally, the baseline of each spectrum was subtracted by a linear polynomial.

For consistency with previous WISH studies (San José-García et al. 2013 and San José-García et al. subm.), all reduced data were resampled to 0.27 km s$^{-1}$ and the rms noise of the spectra calculated at this resolution. The maximum peak brightness temperature, $T_{\rm peak}$, the full width at zero intensity, *FWZI*, and the total integrated intensity, $W = \int T_{\rm MB} {\rm d}v$, were derived using the method adopted by Mottram et al. (2014), which is briefly explained in Sect. 4.2.4 of this thesis. To compare the presented WILL and Cygnus observations with those of WISH, previous WISH intensity-based measurements ($T_{\rm peak}$, $W$, etc.) have been corrected to account for the updated values of $\eta_{mb}$ adopted in this work (see corrector factors in Table 4.1). The $^{13}$CO and C$^{18}$O spectra and the water data of a few Cygnus objects are resampled to 1 km s$^{-1}$ bins in order to calculate the *FWZI* because the lines are too narrow to use with 3 km s$^{-1}$ binning, the value adopted for the water and $^{12}$CO data. These parameters are presented in Tables 5.11 to 5.12 for the WILL samples and in Tables 5.21 to 5.20 for the Cygnus YSOs.

### 5.2.4. Decomposition method

Similarly as for the WISH observations (Kristensen et al. 2010, 2012; van der Tak et al. 2013; Mottram et al. 2014, San José-García et al. subm.), the complex $H_2O$ and CO line profiles can be decomposed into several Gaussian components. These different velocity components trace specific physical and kinematical conditions within the protostellar environments, so it is important to accurately characterise the line profiles. The number of velocity components needed to reproduce the profiles differs for each object but the basic types of profiles are the same for all sources.

The procedure to constrain the parameters of the different Gaussian profiles (i.e. position, amplitude and *FWHM* of each component) is the same as that presented in Sect. 3.2.1 of Mottram et al. (2014). An example of the Gaussian decomposition procedure and residual from the fitting is shown in Fig. 2.1 in chapter 2. The spectra are fitted by providing initial guess values of the Gaussian components creating the line profiles to an ordinary least-squares solver in the PYTHON

[2]HIPE is a joint development by the *Herschel* Science Ground Segment Consortium, consisting of ESA, the NASA Herschel Science Centre, and the HIFI, PACS and SPIRE consortia.

[3]http://www.iram.fr/IRAMFR/GILDAS/

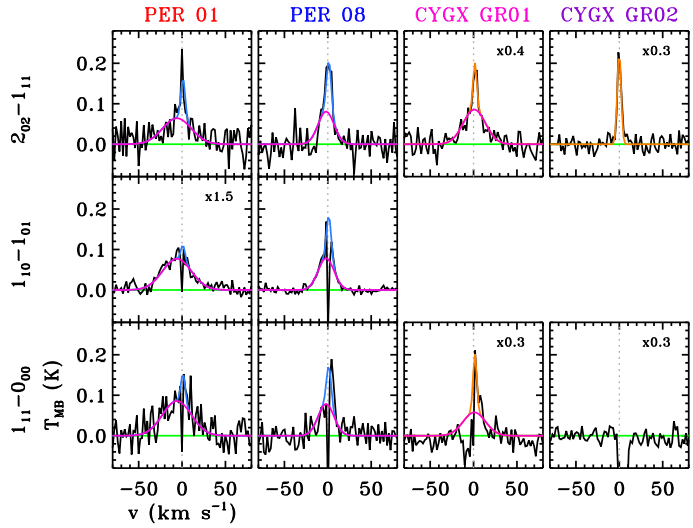


Figure 5.1: Spectra of the $H_2O$ $1_{11}$-$0_{00}$ (1113 GHz; *bottom*-row), $1_{10}$-$1_{01}$ (557 GHz; *middle*-row) and $2_{02}$-$1_{11}$ (988 GHz; *top*-row) for the WILL Class 0 protostar Per 01 (first column), the WILL Class I object Per 08 (second column) and the equivalent of Class 0 and Class I for the Cygnus sources GR01 03 and GR02 01 (third and forth columns respectively) binned to 2 km s$^{-1}$. The different velocity components in which the spectra are decomposed are indicated with different colours: the broad cavity shock component is drawn with the pink line, the medium-broad spot shock component is shown in blue and the narrow quiescent envelope emission in orange (see Sect 5.2.5 for explanation of these components). All spectra have been shifted to 0 km s$^{-1}$ (dotted grey line) and resampled to 2 km s$^{-1}$. The baseline is indicated in green. Further explanation of these components is given in Sect 5.2.5

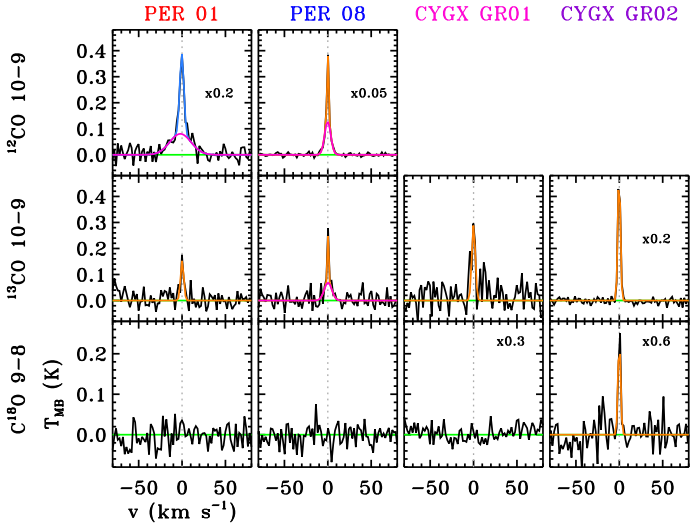


Figure 5.2: Same as Fig. 5.1 but for the C$^{18}$O $J = 9$–8 (*bottom*-row), $^{13}$CO $J = 10$–9 (*middle*-row) and $^{12}$CO $J = 10$–9 (*top*-row) spectra of the same sources. For these lines, the velocity components in which the spectra are decomposed correspond to the broad entrained outflowing component (in pink), the medium-broad spot shock component (in blue) and the quiescent envelope emission (in orange). Further explanation of these components is given in Sect 5.2.5.

module SCIPY.ODR[4]. The number of velocity components is determined by analysis of the residual after fitting the line to a single Gaussian line and adding an extra Gaussian profile until no features are measured above 3 $\sigma_{\rm rms}$. In the case of the water lines, the *FWHM* and central position of each Gaussian component is forced to be the same for all transitions and these parameters are constrained simultaneously by all available $H_2O$ spectra of a given source (i.e. the amplitudes of each Gaussian component are free parameters that can vary for each water transitions). For a given source, the number of components can vary per transition because of their different rms and *S/N* level. The different CO isotopologue transitions are fitted independently because these species are tracing different physical structures in the YSO than water and potentially each other.

The fitting procedure are applied to all water and CO spectra. Four different types of velocity components have been identified: narrow centred near the source velocity, broad at the source $v_{\rm LSR}$ or within few km s$^{-1}$ (usually fitting the line-wings of the spectra), medium-broad offset from the source velocity and medium-broad but offset from $v_{\rm LSR}$ by a large value (>10 km s$^{-1}$). The narrow components can appear in emission or absorption while the other components are always in emission for this sample. In Sect. 5.2.5 the type of gas probed by each of these velocity components is explained depending on the studied molecule.

The narrow component (*FWHM*<5 km s$^{-1}$) present in the water transitions of the WILL protostars has not been fitted. The main reason is that, in general, the ground-state $H_2O$ lines show an absorption feature centred near the source $v_{\rm LSR}$ which appears together with a weak narrow emission also around $v_{\rm LSR}$. The combination of absorption and emission creating the narrow velocity component of the line is difficult to reproduce with a single Gaussian component and the best-fit parameters (amplitude and width) have some associated uncertainty. Therefore, for this version of the data analysis, the range of velocities including both the absorption and narrow weak emission features has been masked out as in previous analysis (Kristensen et al. 2012, 2013; Mottram et al. 2014). This masking does not affect the best-fit parameters of the Gaussian profiles of the broader velocity components.

Examples of the Gaussian decomposition for the studied water lines (1113, 557 and 988 GHz) of Class 0 and Class I type YSO for the WILL and Cygnus samples are shown in Fig. 5.1, and for the observed CO isotopologue transitions in Fig. 5.2. Three velocity components can be identified: the very broad centred near the source velocity, the medium broad offset from $v_{\rm LSR}$ and the narrow component. Finally, the result from the Gaussian fit decomposition of each observed line is presented in Tables 5.13 to 5.17 for the WILL protostars and in Tables 5.24 to 5.23 for the Cygnus YSOs.

### 5.2.5. Linking velocity and physical components

As introduced in Sect. 4.2.6, each velocity component in the water and CO spectra can be associated with a different physical component and structure within the protostellar environment (Kristensen et al. 2012; Mottram et al. 2014; Yıldız et al. 2010, 2013; San José-García et al. 2013, & subm., chapter 4). To simplify the distinction between the different types of components, Table 5.2 summarises their main phenomenological characteristics as well as the physical YSO structures associated with them.

The narrow Gaussian component centred near the source velocity in both $H_2O$ and CO lines is generated by quiescent envelope gas. While this component is generally seen in emission for the excited transitions, it usually appears in absorption in the ground-state optically thick lines because the colder outer parts of the envelope absorb part of this emission. The upper limit of the width of this component differs from low- to high-mass YSOs. In the case of low-mass protostars (i.e. WILL sample) the narrow envelope component is characterised with a *FWHM* less than 5 km s$^{-1}$, consistent with the WISH low-mass study presented in Mottram et al. (2014). On the other hand, for intermediate- and high-mass YSOs (i.e. Cygnus sources), the interval of *FWHM* values for the envelope component is extended up to 10 km s$^{-1}$. This limit is based on the maximum width measured in the $C^{18}O$ $J = 9$–8 transition for the Cygnus sample, which uniquely traces the quiescent

[4] http://scipy.org/

Table 5.2: Name and main characteristic of the fitted velocity components for the $H_2O$ and CO lines together with their physical associations according to Fig. 6 of Mottram et al. (2014).

| Molecule | Observed characteristics | | Physical component |
|---|---|---|---|
| | Width | Offset from $v_{LSR}$? | |
| $H_2O$ | Narrow | No | Quiescent envelope |
| | Broad | No | Outflow cavity shocks |
| | Medium/Broad | Yes, significant | Spot shocks: bullets or EHV[a] |
| | Medium (broad also present) | Yes | Spot shocks: at the base of outflow cavity[b] |
| $^{12}CO$ | Narrow | No | Quiescent envelope |
| | Broad | No | Entrained material in outflow cavity wall |
| | Medium/Broad | Yes, significant | Spot shocks: bullets or EHV[a] |
| $^{13}CO$ | Narrow | No | Quiescent envelope and UV-heated gas[c] |
| | Broad | No | Entrained material in outflow cavity wall |
| $C^{18}O$ | Narrow | No | Quiescent envelope |

**Notes.** Cavity shocks are non-dissociative shocks, while spot shocks are generally dissociative.
[(a)] Extremely high velocity (EHV) emission component (Bachiller et al. 1990; Tafalla et al. 2010; Kristensen et al. 2011). They are considered shocks along the jet. [(b)] Previously called medium-broad offset component in Kristensen et al. (2013). Shocks are caused by the impact of the jet or stellar wind at the base of the outflow cavity wall. [(c)] The narrow $^{13}CO$ emission is associated with the quiescent envelope and the excess emission comes from UV-heated gas along inner regions of the outflow cavity wall (van Kempen et al. 2009a; Yıldız et al. 2012, 2015).

envelope. A larger velocity interval for the envelope emission of the high-mass YSOs is consistent with the picture in which massive YSOs are characterised with more turbulent envelopes (San José-García et al. subm.). In the case of $^{13}CO$, part of the narrow emission is associated to UV-heated gas along inner regions of the outflow cavity walls (Spaans et al. 1995; van Kempen et al. 2009a; Yıldız et al. 2015). This particular case will not be discussed further in this chapter.

The broad velocity component centred at the source velocity (or offset few km $s^{-1}$) is designated using the suffix "b" for consistency with previous studies (chapters 2 and 4 of this thesis), and generally reproduces the line-wings of the spectra (Kristensen et al. 2013; Yıldız et al. 2013; van der Tak et al. 2013). This component is associated with gas within the outflow of different nature depending on the studied molecule (see Fig. 1.1 of chapter 1). In the case of $H_2O$, the emission from the broad component is caused by non-dissociative shocks in layers along the outflow cavity wall (Kristensen et al. 2010, 2013; van Kempen et al. 2010; Nisini et al. 2010; Santangelo et al. 2013). This component is also called "cavity shock component" for the water lines, as introduced by Mottram et al. (2014). On the other hand, for low- and mid-$J$ ($J \leq 10$) $^{12}CO$ and $^{13}CO$ transitions, the broad velocity component is associated with colder entrained outflowing gas (Yıldız et al. 2013; San José-García et al. 2013). This gas is part of the intermediate layer between the outflow cavity and the envelope. Summarising, and as explained in Table 5.2, the broad component detected in the water and low-mid-$J$ CO transitions do not trace the same material within the outflow (Kristensen et al. 2012; Santangelo et al. 2013). Even if phenomenologically we designate these two velocity components as broad, their physical origin is different and should be distinguished.

The velocity component detected largely offset from the source velocity both in $H_2O$ and $^{12}CO$ spectra is associated with hot (up to thousands of K) and energetic dissociative shocks taking place in small and localised regions along the bipolar jets (see Bachiller et al. 1990; Tafalla et al. 2010; Kristensen et al. 2011, for more details). In previous studies, these components were named "bullets" or extremely-high velocity (EHV) components given the large velocity reached by the gas involved in these shocks. In the case of the velocity component detected in the water lines with smaller *FWHM* value and centred at more offset velocities than the broad cavity shock component, this emission is then associated with dissociative shocks occurring at the base of the outflow cavity. This component was perviously known as medium-broad or offset component (Kristensen et al. 2013). Adopting the same terminology as in Mottram et al. (2014) and San José-García et al.

subm., the velocity components tracing the emission from both types of hot and dissociative shocks are designated as "spot shock components" because both of them take place in small localised regions within the outflow.

The focus of this chapter is the study of the broad velocity component detected in the $H_2O$ lines, i.e. the emission from cavity shocks along the outflow cavity wall, across a large range of luminosities. We prioritise the analysis of this component because it is the most commonly detected across the water lines and it probes specific dynamical conditions within the outflow present in low-, intermediate- and high-mass YSOs (see chapter 4). The parameters characterising the other types of velocity components are also included for comparison with previous studies.

# 5.3. Results

First, we present the basic general results of the $H_2O$, $^{12}CO$, $^{13}CO$ and $C^{18}O$ spectra focusing on the number of detections for each studied sample of YSOs, on the shape of the line profiles and on intrinsic parameters of the data such as the *FWZI*(Sect. 5.3.1). Then, we summarise the outcomes from the line decomposition method of the observed lines. The number and contribution of the different velocity components detected in the profiles of the water and CO lines are calculated and the results analysed together with those derived for WISH (Sect. 5.3.2). In addition, a deeper study on the emission coming from the cavity shock component, i.e. the broad velocity component fitted for the water lines, is presented and trends with bolometric luminosity investigated (Sect. 5.3.3). Finally, the derived line luminosity of the $H_2O$ and CO spectra simultaneously observed for the WILL and Cygnus data are studied as a function of $L_{\rm bol}$ (Sect. 5.3.4).

## 5.3.1. Characterisation of the line profiles

The observed $H_2O$ and $H_2^{18}O$ transitions for the WILL and Cygnus samples are presented in Figs. 5.14 to 5.24 and Figs. 5.31 to 5.37, respectively. The $^{12}CO$ $J = 10$–9, $^{13}CO$ $J = 10$–9 and $C^{18}O$ $J = 9$–8 spectra are shown in Figs. 5.25 to 5.30 for the WILL protostars and the $^{13}CO$ $J = 10$–9 and $C^{18}O$ $J = 9$–8 observations in Fig. 5.38 to 5.44 for the Cygnus YSOs.

#### $H_2O$ data

Within the WILL sample, the $H_2O$ $1_{10}$-$1_{01}$ (557 GHz), $1_{11}$-$0_{00}$ (1113 GHz), $2_{02}$-$1_{11}$ (988 GHz) and $3_{12}$-$2_{21}$ (1157 GHz) transitions are detected for 34, 23, 25 and 8 sources out of 45, respectively, while the isotopologue line ($H_2^{18}O$ $1_{10}$-$1_{01}$) is detected for only 2 protostars. As further explained in Appendix 5.B.1, the observations of eight WILL protostars are excluded from the data analysis. In the case of the Cygnus sample, the observed $H_2O$ $1_{11}$-$0_{00}$ (1113 GHz) and $2_{02}$-$1_{11}$ (988 GHz) lines are both detected for 25 out of 86 YSOs. Table 5.3 includes the number of detections of each observed water line, the averaged rms and the mean and median values of the derived *FWZI* for each sub-sample of YSOs.

As for the WISH sample (see Mottram et al. 2014 and Sect. 4.3.1), the line profiles of the different $H_2O$ transitions for a given source are similar, i.e. the spectra with sufficient *S/N* can be fitted with the same number of Gaussian components with a common velocity and width. Absorption features are present in the $H_2O$ ground-state lines for 26 out of 45 WILL sources (76% of the detected 557 GHz lines and 65% of the detected 1113 GHz line) and in 23 out of 86 YSOs for the $H_2O$ $1_{11}$-$0_{00}$ data of Cygnus (i.e. 92% of the detected 1113 GHz spectra). The larger percentage of absorption features measured for the Cygnus YSOs with respect the WILL protostars is consistent with the expected picture of massive star forming region having more absorption from their colder dense envelopes and from foreground clouds along the line of sight than lower-mass objects (Schneider et al. 2006). The Class 0 objects across both samples show a larger percentage of water detections, ~80%, than their more evolved counterparts, ~33%, which agrees with previous results (Mottram et al. 2014).

Table 5.3: Detection statistics, averaged rms and mean and median (M.) values of the *FWZI* for the $^{12}$CO $J = 10$–9, $^{13}$CO $J = 10$–9 and C$^{18}$O $J = 9$–8 spectra and for all observed $H_2O$ transition across the Class 0 and Class I WILL and Cygnus sample of YSOs.

| Line | WILL Class 0 | | | | WILL Class I | | | | Cygnus Class 0 | | | | Cygnus Class I | | | |
|---|---|---|---|---|---|---|---|---|---|---|---|---|---|---|---|---|
| | D/O[a] | $\overline{\sigma_{\rm rms}}$ (mK) | $\overline{FWZI}$ (km s$^{-1}$) | M. *FWZI* (km s$^{-1}$) | D/O[a] | $\overline{\sigma_{\rm rms}}$ (mK) | $\overline{FWZI}$ (km s$^{-1}$) | M. *FWZI* (km s$^{-1}$) | D/O[a] | $\overline{\sigma_{\rm rms}}$ (mK) | $\overline{FWZI}$ (km s$^{-1}$) | M. *FWZI* (km s$^{-1}$) | D/O[a] | $\overline{\sigma_{\rm rms}}$ (mK) | $\overline{FWZI}$ (km s$^{-1}$) | M. *FWZI* (km s$^{-1}$) |
| $^{12}$CO $J = 10$–9 | 19/24 | 98 | 34±6 | 24.0 | 17/21 | 98 | 19±2 | 18.0 | – | – | – | – | – | – | – | – |
| $^{13}$CO $J = 10$–9 | 12/24 | 27 | 16±2 | 13.7 | 8/21 | 26 | 10±2 | 8.7 | 6/8 | 56 | 8±1 | 7.1 | 35/78 | 51 | 7±1 | 5.4 |
| C$^{18}$O $J = 9$–8 | 1/24 | 25 | 7.2[b] | 7.2 | 0/21 | – | – | – | 1/8 | 44 | 7[b] | 6.8 | 10/78 | 49 | 5±1 | 3.6 |
| $H_2O$ $1_{10}$-$1_{01}$ | 19/24 | 9 | 75±10 | 72 | 15/21 | 7 | 37±5 | 27 | – | – | – | – | – | – | – | – |
| $H_2O$ $1_{11}$-$0_{00}$ | 16/24 | 26 | 59±11 | 46 | 7/21 | 25 | 43±5 | 39 | 7/8 | 50 | 49±14 | 28 | 18/78 | 50 | 31±5 | 28 |
| $H_2O$ $2_{02}$-$1_{11}$ | 16/24 | 28 | 56±11 | 47 | 9/21 | 25 | 31±3 | 33 | 7/8 | 26 | 56±8 | 59 | 18/78 | 25 | 36±5 | 40 |
| $H_2O$ $3_{12}$-$2_{21}$ | 6/24 | 124 | 55±16 | 56 | 2/21 | 116 | 21[c] | 21 | – | – | – | – | – | – | – | – |
| $H_2^{18}O$ $1_{10}$-$1_{01}$ | 2/24 | 7 | 35[c] | 35 | 0/21 | – | – | – | – | – | – | – | – | – | – | – |

**Notes.** [(a)] Number of detected sources with respect to the total number of observed YSOs for each line. See Appendix 5.B.1 for further information about the WILL protostars not considered in the analysis. [(b)] No standard deviation is given for detections in less than four sources.

For the WILL Class 0 objects, the mean and median *FWZI* values of the $H_2O$ transitions are similar among the observed lines, except for the 557 GHz transition, characterised with the widest profiles and the highest *S/N*. This transition is the only one that shows similar mean and median *FWZI* values as those measured for the WISH Class 0, while for the other $H_2O$ transitions these parameters are smaller for the WILL sample by ∼15 km s$^{-1}$. In the case of the WILL Class I protostars, the derived mean and median *FWZI* values are similar within the uncertainty among the $H_2O$ transitions with more than three detections and to those constrained for the WISH Class I objects.

Moving to the Cygnus YSOs, the derived mean *FWZI* values of the two water transitions are comparable within the Class 0 and Class I-type sub-samples. The mean and median *FWZI* parameters for the Cygnus Class 0 sources are more similar to those obtained for the WISH high-mass YSOs than for the other WISH sub-group of objects while the results obtained for the Cygnus Class I are comparable to those from the WISH and WILL Class I protostars.

The derived *FWZI* values for the WILL and Cygnus water observations are scatted across a large range of velocities (from 5 to ∼160 km s$^{-1}$) and no trend with luminosity is measures, consistent with the WISH results. A more detailed analysis of the *FWZI* values across the WILL, Cygnus and WISH samples and as a function of $L_{\rm bol}$ is presented in Appendix 5.A.

**CO data**

The $^{12}$CO $J = 10$–9 line is detected in emission for 26 out of 45 WILL protostars, where 19/24 are Class 0 sources and 17/21 are Class I YSOs. This line was not observed for the Cygnus sample. The detection statistics of the $^{12}$CO $J = 10$–9 data, the averaged rms of the spectra and the mean and median values of the *FWZI* parameter for each WILL sub-sample of sources are presented in Table 5.3. As for the WISH low-mass observations, the mean and median *FWZI* values are larger for the Class 0 objects than for the Class I since in general the Class 0 protostars show broader and more complex (larger number of velocity components) line profiles than those of their more evolved counterparts (further discussion on this result in Appendix 5.A). While the mean and median *FWZI* values of the WILL and WISH Class 0 sources are comparable within the uncertainty, the WISH Class I objects show slightly wider line-wings than those of WILL.

In the case of the $^{13}$CO $J = 10$–9 observations, the line was detected for 20/45 WILL protostars and for 41/86 Cygnus YSOs (Table 5.3). The shapes of the profiles are similar to those observed for the WISH low-mass protostars since 90% of the detected WILL and Cygnus objects show single Gaussian-like profiles and only few sources have pronounced line wings. Therefore, the Cygnus spectra differ from those of the WISH high-mass objects, which show more complex profiles with remarkable line wings that enlarge their *FWZI* values. This is further discussed in Sect. 5.4.

Finally, the C$^{18}$O $J = 9$–8 line is detected for only one WILL source (the Class 0 object Ser 02) and for 11 Cygnus YSOs. As for the WISH sample, all spectra show narrow single Gaussian-like profiles (Table 5.3). In the case of the Cygnus sample, for which more lines have been detected, the obtained mean *FWZI* value is slightly smaller than that calculated for the WISH high-mass YSOs but comparable to the intermediate-mass objects.

## 5.3.2. Analysis of the decomposition process

**$H_2O$ line profiles**

Table 5.4 summarises the results from the profile decomposition for the WILL, Cygnus and WISH sub-samples, i.e. the detection statistics of each velocity component and their mean and median *FWHM* values. The percentage of $H_2O$ line profiles decomposed into more than one velocity component is similar for both WILL and Cygnus sample (53% versus 48% of the sources for which water lines are detected). However, while the cavity shock component (broad velocity component) is seen in all detected water lines for the WILL protostars, this component is not seen in 16% of the Cygnus spectra.

Within the WILL sample, ∼74% of the detected water lines for the Class 0 protostars (14/19) can be decomposed into two or three velocity components but only 27% of the detected Class I

Table 5.4: Number of detections and mean and median *FWHM* values of each physical component in which the $H_2O$ line profiles of the WILL and Cygnus samples are decomposed. The results from the cavity shock component for the WISH low-, intermediate- and high-mass YSOs are also included.

| | observed $H_2O$ transitions | | | | | | | | |
|---|---|---|---|---|---|---|---|---|---|
| | Envelope comp. | | | Cavity shock comp. | | | Spot shock comp. | | |
| | D[a] | $\overline{FWHM}$ (km s$^{-1}$) | M. *FWHM* (km s$^{-1}$) | D[a] | $\overline{FWHM}$ (km s$^{-1}$) | M. *FWHM* (km s$^{-1}$) | D[a] | $\overline{FWHM}$ (km s$^{-1}$) | M. *FWHM* (km s$^{-1}$) |
| WILL Cl 0 | 1/19[b] | 3.5[c] | 3.5 | 19/19 | 32±4 | 26 | 15/19[d] | 21±5 | 13 |
| WILL Cl I | 1/15[b] | 4.3[c] | 4.3 | 15/15 | 17±2 | 16 | 3/15 | 6±1 | 6 |
| WISH Cl 0 | 15/15 | 3.6±0.3 | 3.5 | 15/15 | 29±3 | 24 | 10/15 | 23±5 | 18 |
| WISH Cl I | 11/11 | 3.0±0.4 | 2.6 | 11/11 | 18±2 | 15 | 3/11 | 17[c] | 26 |
| Cygnus Cl 0 | 5/7 | 6.7±1.0 | 6.0 | 7/7 | 33±5 | 37 | 0 | – | – |
| Cygnus Cl I | 11/18 | 5.0±0.6 | 5.2 | 14/18 | 28±3 | 28 | 0 | – | – |
| WISH IM | 7/7 | 5.4±0.6 | 4.6 | 7/7 | 29±2 | 32 | 1/7 | 31[c] | 31 |
| WISH HM | 19/19 | 5.3±0.2 | 5.6 | 19/19 | 27±2 | 24 | 0 | – | – |

**Notes.** Cl 0: low-mass Class 0 protostars; Cl I: low-mass Class I sources; IM: intermediate-mass; HM: high-mass

[(a)] Number of components detected over $3\sigma_{\rm rms}$ with respect the total number of sources detected in each water transition. [(b)] This should be considered as a lower limit since in general the envelope component has not been fitted for the WILL sources, as explained in Sect. 5.2.4. [(c)] No standard deviation is given if the number of detected sources is less than three. [(d)] The spectra of three objects show two spot shock components, so the actual number of YSOs with this type of velocity component is 12 instead of 15.

line profiles (4/15) have two velocity components. For both sub-groups of YSOs, the combination of a cavity shock and a spot shock component dominates (in 12 of those 14 Class 0 and three out of those four Class I sources). No spot shock components largely offset from $v_{\rm LSR}$ are detected for the Class I objects. The spectra fitted with a single Gaussian-like profile (the remaining 26% and 73% of the Class 0 and Class I protostars respectively) show always a broad profile i.e. cavity shock emission.

For the Cygnus $H_2O$ data, the spectra of five out of the seven Class 0-type objects show two velocity components profile (71% of the detected data) versus only 7/18 Class I Cygnus objects (39%). These line profiles are always decomposed into an envelope and a cavity shock component. In the case of the spectra fitted with a single velocity component (13/25), a broad Gaussian profile is found for most of these spectra except for four Class I-type sources which show surprisingly narrow ($FWHM < 8$ km s$^{-1}$) and bright Gaussian-like profiles. This type of narrow profile has not been observed for any water spectra of the WISH sample (further discussion in Sect. 5.4). No spot shock components, especially largely offset from the source velocity, are detected in any of the Cygnus observations. This latter result is consistent with the outcomes from the excited water line analysis of all WISH high-mass sample and most of the intermediate-mass YSOs. Spot shock components were detected in absorption in the ground-state lines of most but not all WISH high-mass objects (see van der Tak et al. 2013), while they are seen neither in absorption nor emission for the Cygnus ground-state $H_2O$ transition (1113 GHz line).

Summarising, the water line profiles of the WILL Class 0 sources present a larger number of velocity components than those of the WILL Class I and Cygnus objects. A combination of cavity and spot shock components is in general the configuration most common for the WILL Class 0 data and only a cavity shock component that for the WILL Class I sources. For the Cygnus sample, combination of the envelope and cavity shock components is more frequently seen in the Class 0-type objects and only a cavity shock component or the combination of an envelope plus cavity shock have equal detection rates for the Class I-type objects.

In the following, we focus the analysis on the cavity shock component which is detected in most of the studied observations. The mean *FWHM* values of this component for the WILL Class 0

Table 5.5: Average fraction of the integrated intensity that each velocity components, $W_{\rm comp.}$, contribute to the total integrated intensity, $W$, of the $H_2O$ $1_{10}$-$1_{01}$ (557 GHz), $H_2O$ $1_{11}$-$0_{00}$ (1113 GHz), $H_2O$ $2_{02}$-$1_{11}$ (988 GHz) and $H_2O$ $3_{12}$-$2_{21}$ (1157 GHz) lines for the WILL Class 0, WILL Class I, Cygnus Class 0 and Cygnus Class I sources.

| | Envelope | | Cavity | | Spot | | Envelope | | Cavity | | Spot | |
|---|---|---|---|---|---|---|---|---|---|---|---|---|
| | D[a] | $W_{\rm comp.}/W$ | D[a] | $W_{\rm comp.}/W$ | D[a] | $W_{\rm comp.}/W$ | D[a] | $W_{\rm comp.}/W$ | D[a] | $W_{\rm comp.}/W$ | D[a] | $W_{\rm comp.}/W$ |
| Line | WILL Class 0 | | | | | | WILL Class I | | | | | |
| $H_2O$ $1_{10}$-$1_{01}$ | 19 | -0.1±0.1 | 19 | 1.0±0.1 | 7 | 0.1±0.1 | 15 | -0.2±0.1 | 15 | 1.2±0.1 | 3 | 0.1±0.1 |
| $H_2O$ $1_{11}$-$0_{00}$ | 12 | 0.1±0.5 | 12 | 0.8±0.5 | 4 | 0.1±0.1 | 5 | -0.2±0.1 | 5 | 1.1±0.1 | 1 | 0.1[c] |
| $H_2O$ $2_{02}$-$1_{11}$ | 11 | 0.0±0.1 | 11 | 0.8±0.1 | 5 | 0.2±0.1 | 5 | 0.0±0.1 | 5 | 0.9±0.1 | 1 | 0.1[c] |
| $H_2O$ $3_{12}$-$2_{21}$ | 4 | 0.0±0.1 | 4 | 0.8±0.1 | 2 | 0.2±0.1 | 1 | -0.1[b] | 1 | 1.1[b] | – | – |
| Line | Cygnus Class 0 | | | | | | Cygnus Class I | | | | | |
| $H_2O$ $1_{11}$-$0_{00}$ | 5 | -0.4±1.1 | 4 | 1.4±1.1 | 0 | – | 12 | -3.1±2.7 | 12 | 4.1±2.7 | 0 | – |
| $H_2O$ $2_{02}$-$1_{11}$ | 7 | 0.0±0.1 | 7 | 1.0±0.1 | 0 | – | 15 | 0.1±0.2 | 15 | 0.9±0.2 | 0 | – |

**Notes.** The envelope contribution is calculated as: $W_{\rm envelope} = W - W_{\rm cavity\,shock} - W_{\rm spot\,shock}$.
[a] Number of sources which spectra show contribution for each indicated component. [b] No standard deviation is given for detections in less than four sources.

and Cygnus objects are similar within the uncertainty. These numbers are comparable to those calculated for the WISH low-mass Class 0, intermediate- and high-mass YSOs (Table 5.4). Interestingly, the median *FWHM* values of the Cygnus Class 0 and WISH intermediate-mass objects are the largest across the entire WILL, WISH and Cygnus samples. The mean and median *FWHM* values of the Class I protostars of both WILL and WISH are similar. These two sub-groups of objects have the narrowest line profiles.

The average fraction of the integrated intensity that the envelope, cavity shock and spot shock components contribute to the total integrated intensity of the observed $H_2O$ lines is presented for the entire WILL and Cygnus sample of YSOs in Table 5.5. This contribution is calculated as explained in Mottram et al. (2014) and Sect. 4.3.1. In the case of the ground-state water lines, in particular the $H_2O$ $1_{11}$-$0_{00}$ (1113 GHz) transition, the contribution of the cavity shock component can be above 1 because the strong envelope absorption features in these spectra reduce the total integrated intensity. Thus the envelope component has a negative intensity.

The contribution from the different types of velocity components for the $H_2O$ $2_{02}$-$1_{11}$ (988 GHz) spectra of the WILL and Cygnus YSOs are compared to those of WISH (see Table 4.2 of this thesis and Table 4 of Mottram et al. 2014). On average, the cavity shock component contributes with more than 80% to the total integrated intensity of the line. These values are consistently larger than those obtained from WISH, especially for the intermediate- and high-mass sub-samples for which that fraction constitutes 60% of the total integrated intensity. In general, the remaining contribution from the water spectra of the WILL Class 0 protostars comes from the spot shock component, while for more massive or evolved objects, such as the WILL Class I and Cygnus YSOs, it seems to come from the envelope. This result is consistent with that derived from the excited water lines of the WISH sample (see Sect. 4.3.1).

### CO line profiles

The $^{12}$CO $J = 10$–9 spectra of 42% (8/19) WILL Class 0 protostars show more than two velocity components, where the combination of a narrow and a broad component is the most common (a summary of the decomposition result for this transition in are given Table 5.6). These profiles most resemble those observed for the WISH low-mass Class 0 objects. Only two sources (Per 03, also known as L1448-C(S), and Per 20) have additional EHV emission features. The profiles with a single velocity component are either narrow or broad. On the other hand, only 29% (5/17) of the $^{12}$CO $J = 10$–9 WILL Class I spectra can be decomposed into two velocity components (narrow and broad) while the spectra of the other protostars show a single narrow line profile. No spot

Table 5.6: Number of detections and mean and median *FWHM* values of each velocity component in which the $^{12}$CO $J = 10$–9 line profiles of the WILL protostars are decomposed.

| | $^{12}$CO $J = 10$–9 | | | | | | | | |
|---|---|---|---|---|---|---|---|---|---|
| | Envelope comp. | | | Broad comp. | | | Spot shock comp. | | |
| | D[a] | $\overline{FWHM}$ (km s$^{-1}$) | M. *FWHM* (km s$^{-1}$) | D[a] | $\overline{FWHM}$ (km s$^{-1}$) | M. *FWHM* (km s$^{-1}$) | D[a] | $\overline{FWHM}$ (km s$^{-1}$) | M. *FWHM* (km s$^{-1}$) |
| WILL Cl 0 | 11/19 | 3.0±0.3 | 3.1 | 13/19 | 15±3 | 10.1 | 6/19[c] | 13±3 | 9 |
| WILL Cl I | 15/17 | 3.3±0.2 | 3.0 | 7/17 | 10±1 | 8.7 | 0/17 | – | – |
| WISH Cl 0 | 14/15 | 4.0±0.5 | 4.0 | 12/15 | 20±3 | 17.8 | | | |
| WISH Cl I | 11/11 | 3.5±0.3 | 3.7 | 3/11 | 11[b] | 12.7 | | | |

**Notes.** Cl 0: low-mass Class 0 protostars; Cl I: low-mass Class I sources.
[a] Number of components detected over $3\sigma_{\rm rms}$ with respect the total number of protostars with detected $^{12}$CO $J = 10$–9 emission. [b] No standard deviation is given for detections in less than four sources. [c] The spectra of two sources show two spot shock components, so the actual number of protostars presenting this component is four.

Table 5.7: Number of detections and mean and median *FWHM* values of each velocity component in which the $^{13}$CO $J = 10$–9 and C$^{18}$O $J = 9$–8 line profiles for the WILL and Cygnus samples are decomposed.

| | $^{13}$CO $J = 10$–9 | | | | | | C$^{18}$O $J = 9$–8 | | |
|---|---|---|---|---|---|---|---|---|---|
| | Narrow comp. | | | Broad comp. | | | Narrow comp. | | |
| | D[a] | $\overline{FWHM}$ (km s$^{-1}$) | M. *FWHM* (km s$^{-1}$) | D[a] | $\overline{FWHM}$ (km s$^{-1}$) | M. *FWHM* (km s$^{-1}$) | D[a] | $\overline{FWHM}$ (km s$^{-1}$) | M. *FWHM* (km s$^{-1}$) |
| WILL Cl 0 | 7/12 | 3.0±0.5 | 2.7 | 2/12 | 11.5[b] | 11.5 | 1/1 | 5.4[b] | 5.4 |
| WILL Cl I | 7/8 | 2.2±0.2 | 2.2 | 3/8[c] | 7.3 | 6.5 | 0/1 | – | – |
| WISH Cl 0 | 13/13 | 2.7±0.5 | 2.3 | 2/13 | 11.9[b] | 11.9 | 2/2 | 2.5[b] | 2.5 |
| WISH Cl I | 7/7 | 3.9±0.6 | 2.2 | 0/7 | – | – | 3/3 | 3.1[b] | 3.1 |
| Cygnus Cl 0 | 6/6 | 4.5±0.7 | 4.9 | 1/6 | 8.0[b] | 8.0 | 1/1 | 7.1[b] | 7.1 |
| Cygnus Cl I | 33/35 | 2.7±0.2 | 2.5 | 2/35 | 11.2[b] | 11.2 | 10/10 | 2.8±0.3 | 2.7 |
| WISH IM | 6/6 | 5.0±0.3 | 4.8 | 1/6 | 14.7[b] | 14.7 | 4/4 | 4.0±0.5 | 3.9 |
| WISH HM | 18/19 | 5.9±0.3 | 4.8 | 13/19 | 14.1±1.0 | 13.6 | 19/19 | 5.0±0.3 | 5.0 |

**Notes.** Cl 0: low-mass Class 0 protostars; Cl I: low-mass Class I sources; IM: intermediate-mass; HM: high-mass.
[a] Number of components detected over $3\sigma_{\rm rms}$ with respect the total number of YSOs detected on $^{13}$CO $J = 10$–9 and C$^{18}$O $J = 9$–8. [b] No standard deviation is given for detections in less than four sources. [c] The line profile of two of those three sources can be decomposed into a two Gaussian components: a broad and a narrow component.

shock components offset from the source velocity are detected.

The left-column histograms of Fig. 5.3 compare the *FWHM* values of the broad velocity component, $FWHM_{\rm b}$, across the WILL and WISH low-mass protostars. Both histograms and mean and median $FWHM_{\rm b}$ calculations indicate that this velocity component is narrower (by ~5 km s$^{-1}$) for the WILL Class 0 than for their WISH analogues. In addition, the percentage of broad component detections (as well as detected spectra decomposed into more than one velocity component) is larger (>72%) for the WISH Class 0 protostars. This suggest some differences between the intrinsic properties of the objects constituting both WILL and WISH Class 0 samples (more details in Sect. 5.4). On the other hand, the percentage of detected broad velocity components and the $FWHM_{\rm b}$ values are similar for the Class I protostars of both WILL and WISH sub-samples, as the bottom-left histogram of Fig. 5.3 and Table 5.6 confirm.

Table 5.7 summarises the mean and median *FWHM* values of the velocity components detected

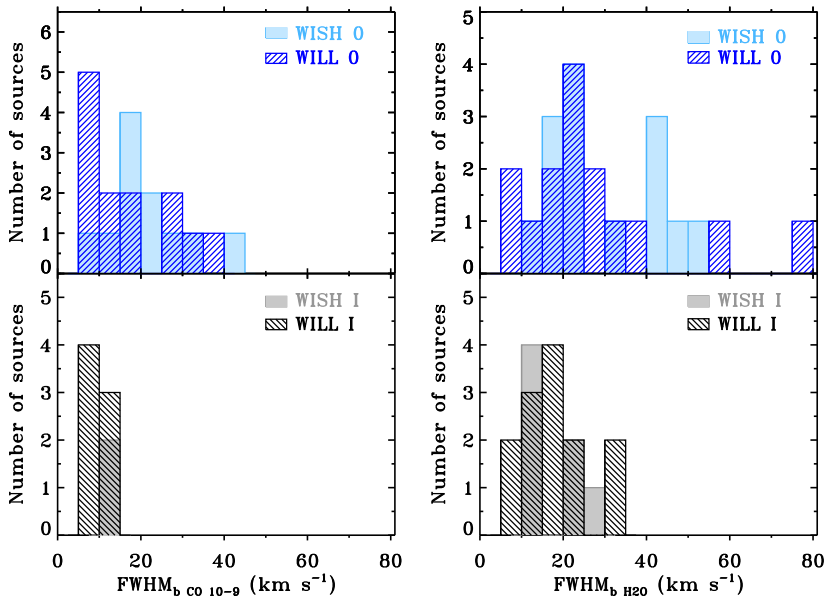


Figure 5.3: Histograms comparing the calculated $FWHM_b$ values of the $^{12}$CO $J = 10$–9 spectra (*left*-column) and the $H_2O$ lines (*right*-column) across the WILL and WISH samples. *Top*-panels: WILL and WISH Class 0 protostars (dashed blue and light blue bars, respectively). *Bottom*-panels: WILL and WISH Class I objects (dashed grey and light grey bars, respectively).

for the $^{13}$CO $J = 10$–9 and C$^{18}$O $J = 9$–8 spectra of the WILL, Cygnus and WISH samples. For the $^{13}$CO $J = 10$–9 data, the percentage of spectra decomposed into two velocity components is almost the same for the WILL and WISH low-mass protostars (3/20 versus 2/20 respectively). Similarly, the $^{13}$CO $J = 10$–9 spectra of only two out of 41 Cygnus YSOs can be decomposed into two velocity components. Therefore, the majority of the detected spectra for the WILL and Cygnus YSOs show narrow Gaussian-like profiles. None of the two types of spot shock component is detected across these data. Focusing on the envelope (narrow) component, the mean and median $FWHM_n$ values are similar, within the uncertainty, for the WILL, Cygnus Class I and WISH low-mass samples. The $FWHM_n$ of the Cygnus Class 0 and those of the WISH intermediate- and high-mass samples are comparable and broader than those of the other sub-samples of YSOs. These results are confirmed by Fig. 5.4, which presents the constrained $FWHM_n$ for the Cygnus YSOs together with those derived from the WISH high-mass objects. This figure shows that the $FWHM_n$ distribution peaks at different velocities for the Class 0 and Class I-type objects (5 km s$^{-1}$ and 1 km s$^{-1}$ respectively). Interestingly, the $FWHM_n$ of this transition for the WISH intermediate- and high-mass YSOs is always larger than 3 km s$^{-1}$. This analysis suggests that the $FWHM_n$ increases with $L_{bol}$ for the Class 0-type objects.

As for the previous analysed transition, C$^{18}$O $J = 9$–8 $FWHM_n$ values for the WISH low-mass protostars are similar to those measured for the Cygnus Class I YSOs (see Table 5.7) and smaller to those obtained across the WISH intermediate- and high-mass sub-samples. No further conclusions can be extracted from the WILL and Cygnus Class 0 samples due to the small number of detections.

### 5.3.3. Analysis of the broad velocity component for $H_2O$ spectra

Figure 5.3 compares the $FWHM_b$ results from the $H_2O$ data of the WILL (dashed bins) and WISH Class 0 and Class I objects (right-top and -bottom panels respectively). The distribution of the values for the Class 0 and Class I objects seems to peak at similar $FWHM_b$ values (~25 km s$^{-1}$). While ~35% of the WISH Class 0 protostars show $FWHM_b$ larger than 40 km s$^{-1}$, only the $FWHM_b$

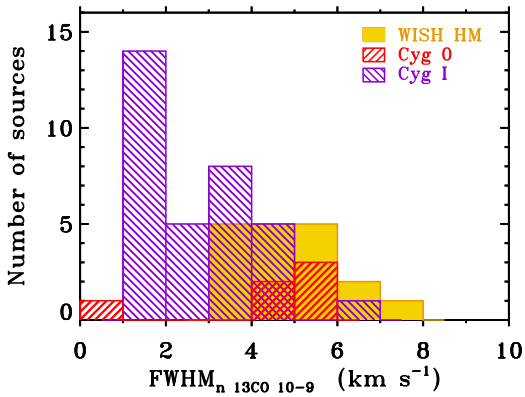


Figure 5.4: *FWHM* of the narrow component ($FWHM_n$) constrained for the $^{13}CO$ $J = 10$–9 spectra of the Cygnus Class 0 (Cyg 0: right-dashed red) and Class I type (Cyg I: left-dashed purple) YSOs and the $FWHM_n$ of the WISH high-mass YSOs (yellow).

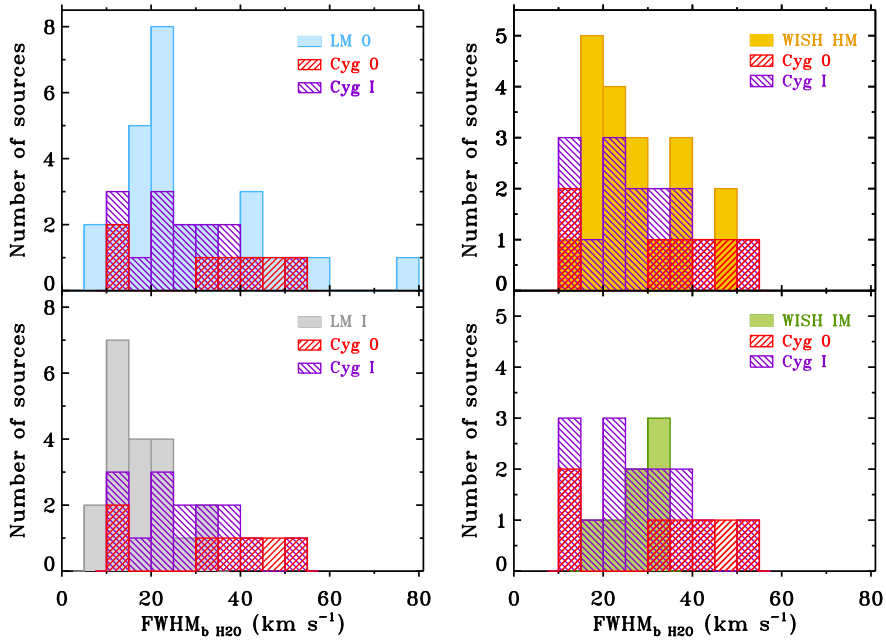


Figure 5.5: (*Left*) $FWHM_b$ of the $H_2O$ spectra calculated for the Cygnus Class 0 (Cyg 0: dashed red bars) and Class I-type (Cyg I: dashed purple bars) YSOs and the $FWHM_b$ of the low-mass Class 0 (LM 0: light blue) protostars (*top*) and Class I (LM I: light grey) objects (*bottom*). The low-mass Class 0 and Class I values are a combination of the results from the WILL and WISH samples shown in Fig. 5.3. (*Right*) Same as *left* histograms but the Cygnus $FWHM_b$ values are plotted together with those of the WISH high-mass (WISH HM: yellow bars) YSOs (*top*) and the WISH intermediate-mass (WISH IM: light green bars) objects (*bottom*).

of ~15% of the WILL Class 0 objects exceeds that velocity. As the central column of Table 5.4 shows, the cavity shock component is similar for the studied water lines of the WILL and WISH low-mass protostars and the results derived from the WISH YSOs are consistent with those obtained from WILL.

In Fig. 5.5, the $FWHM_b$ results from the Cygnus $H_2O$ observations are compared to those obtained from combining the WILL and WISH low-mass values for the Class 0 and Class I objects respectively (left-column histograms) and to the $FWHM_b$ derived from the WISH intermediate- and high-mass YSOs (right-column panels). The $FWHM_b$ values of the Cygnus Class 0 type YSOs are

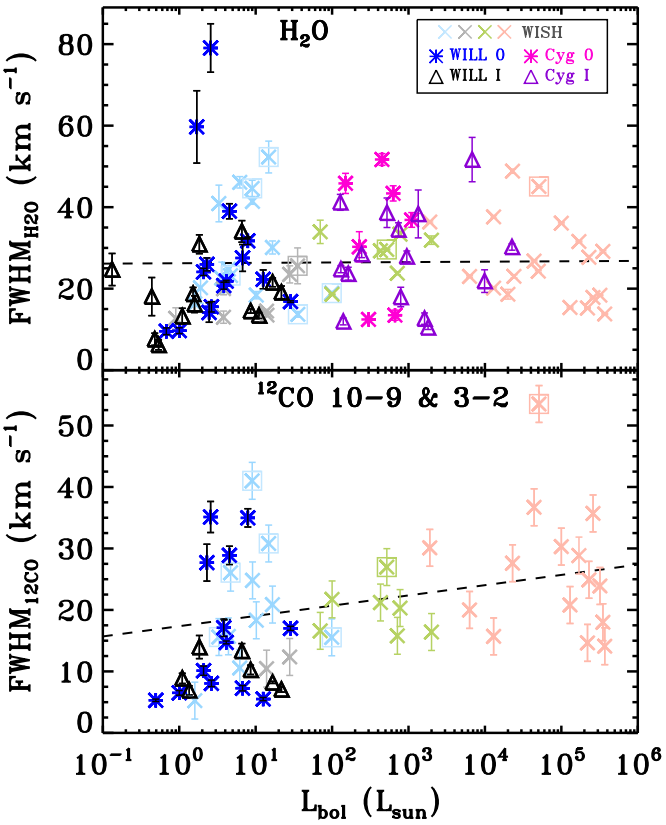


Figure 5.6: (*Top*) $FWHM_{\rm b}$ of the $H_2O$ observations (same for all transitions) for the WILL and Cygnus YSOs versus their bolometric luminosity over-plotted together with those of WISH. (*Bottom*) Same as top panel but for the $^{12}$CO $J = 10$–9 and $J = 3$–2 observations of the WILL and WISH objects. The blue and pink asterisk symbols correspond to the WILL and Cygnus Class 0 YSOs (WILL 0 and Cyg 0). The black and purple triangle symbols to the WILL and Cygnus Class I-type objects (WILL I and Cyg I). The light blue, grey, green and red crosses show the WISH low-mass Class 0, Class I, intermediate- and high-mass YSOs respectively (see Fig. 2 of San José-García et al. subm.). The low- and intermediate-mass WISH sources with detected EHV components are surrounded by a box, as well as the high-mass YSO with triangular water line profiles. The variation of $FWHM_{\rm b}$ with $L_{\rm bol}$ considering the WILL, Cygnus and WISH surveys are indicated with a dash line.

comparable to the wider cavity shock component detected within the low-mass Class 0 protostars. The small number of available Cygnus Class 0 sources complicates the comparison of these results with those of the other samples. In the case of the Cygnus Class I type YSOs, the majority of the cavity shock components have widths between 10 and 30 km s$^{-1}$, so the distribution of their $FWHM_{\rm b}$ is comparable to that measured from the combination of the WILL and WISH low-mass Class I protostars or to that of the WISH high-mass objects.

The histograms of Figs. 5.3 and 5.5 show that the Class 0-type objects are characterised with broader cavity shock components than their more evolved counterparts independently of the mass of the sample.

Finally, Fig. 5.6 shows the $FWHM_{\rm b}$ values of the water lines for the WILL and Cygnus sources (top-panel) and those derived for the $^{12}$CO $J = 10$–9 spectra for the WILL protostars (bottom-panel) as a function of $L_{\rm bol}$. The $FWHM_{\rm b}$ measured for the WISH sample are over-plotted with lighter colours. Appendix 5.A shows the analogous figure but using the results from the *FWZI* parameter. The $FWHM_{\rm b}$ values for the water observations are spread across a large range of ve-

Table 5.8: *Left-column:* Number of considered sources (D), slope ($m$), intercept ($n$), and Pearson correlation coefficient ($r$) of the power-law fit to the logarithm of the line luminosity versus the logarithm of the bolometric luminosity ($L_{bol}$). *Right-column:* Same as above, but for the correlation between the luminosity corresponding to the broad velocity component and $L_{bol}$. The parameters from the correlation have been calculated considering only the WILL and Cygnus samples (*top*-lines) and including the results from the WISH YSOs (*bottom*-lines).

| Line | WILL + Cygnus | | | | | | | |
|---|---|---|---|---|---|---|---|---|
| | $\log(L) = n + m \cdot \log(L_{bol})$ | | | | $\log(L_{broad}) = n + m \cdot \log(L_{bol})$ | | | |
| | D[a] | $m$ | $n$ | $r$ | D[a] | $m$ | $n$ | $r$ |
| $H_2O$ $1_{11}$-$0_{00}$ | 41 | 0.58±0.08 | -3.24±0.17 | 0.74/4.7$\sigma$ | 33 | 0.81±0.07 | -3.24±0.15 | 0.89/5.0$\sigma$ |
| $H_2O$ $2_{02}$-$1_{11}$ | 50 | 0.78±0.12 | -3.25±0.14 | 0.85/6.0$\sigma$ | 38 | 0.77±0.07 | -3.04±0.15 | 0.89/5.4$\sigma$ |
| $^{13}CO$ 10–9 | 60 | 0.87±0.10 | -3.85±0.13 | 0.90/7.0$\sigma$ | 8 | 0.95±0.25 | -4.23±0.32 | 0.94/2.3$\sigma$ |
| | WILL + Cygnus + WISH | | | | | | | |
| $H_2O$ $2_{02}$-$1_{11}$ | 103 | 0.83±0.04 | -3.34±0.11 | 0.92/9.2$\sigma$ | 85 | 0.78±0.03 | -3.17±0.10 | 0.92/8.5$\sigma$ |
| $^{13}CO$ 10–9 | 107 | 0.92±0.03 | -4.04±0.10 | 0.95/9.8$\sigma$ | | – | – | – |

**Notes.** [a] Number of YSOs with positive integrated intensity considered in the correlation calculation.

locities (from 5 to ~80 km s$^{-1}$), a scatter which may be related to the intrinsic properties of the source such as inclination of the outflows, opening angle, etc. The scatter and range of velocities are comparable to that measured for the WISH low-mass protostars, with the difference that the separation between the Class 0 and Class I objects is more obvious within WISH, i.e. the bulk of the $FWHM_b$ results for the WILL Class 0 protostars are located across a velocity interval similar to that occupied by the WILL Class I objects. For the $^{12}CO$ $J = 10$–9 spectra, the range of WILL and WISH low-mass $FWHM_b$ parameters is comparable and no Class I objects are seen as outliers for either of these sub-samples.

The ratio between the broad velocity component of the $H_2O$ and $^{12}CO$ observations is calculated for the WILL protostars and the averaged value for the Class 0 objects is 0.7±0.1 and for the Class I protostars is 0.5±0.1. This ratio is generally smaller than unity, which means that for the low-mass protostars $FWHM_b$ of $H_2O$ is wider than that of $^{12}CO$ $J = 10$–9, consistent with the results of the WISH results in chapter 4 (see Table 4.3) and Kristensen et al. (2012). For both samples, only those sources with prominent outflows, such as L1448-MM, show ratios above unity. Since the $^{12}CO$ $J = 10$–9 transition was not observed for the Cygnus objects, we cannot extend this analysis to these YSOs.

## 5.3.4. Line luminosity study

The total integrated intensity, $W$, of the WILL and Cygnus $^{13}CO$ $J = 10$–9, $H_2O$ $1_{11}$-$0_{00}$ and $2_{02}$-$1_{11}$ lines are converted to line luminosity, $L_{^{13}CO}$ and $L_{H_2O}$, using the same method as in Sects. 2.3.2 and 4.3.3. This parameter accounts for the difference in distance between these two samples of objects and allows us to compare these results with those obtained for WISH and extragalactic objects (see Sect. 2.4.3 and 4.4.3 of this thesis).

Figure 5.7 shows the line luminosity of the $H_2O$ $1_{11}$-$0_{00}$ transition (top panel), the $2_{02}$-$1_{11}$ line (middle panel) and the $^{13}CO$ $J = 10$–9 data (bottom panel) as a function of $L_{bol}$ for the WILL and Cygnus YSOs, and their log($L$)-log($L_{bol}$) relation is indicated with a solid line. This type of correlation was previously measured for the WISH sample (see chapters 2 and 4). The WISH values are then over-plotted in lighter colours for the $H_2O$ $2_{02}$-$1_{11}$ and $^{13}CO$ $J = 10$–9 transitions and their relation with $L_{bol}$ shown with a grey dotted line, together with the correlation measured when combining all WILL, Cygnus and WISH YSOs (dashed line). The parameters of these relations and the Pearson correlation coefficients, $r$, are summarised for these lines in Table 5.8, left-column. The significance of these correlations, determined as in Marseille et al. (2010), is larger than 4.8$\sigma$.

The slope is close to unity, especially when the WILL, Cygnus and WISH sources are combined, except for the $H_2O$ $1_{11}$-$0_{00}$ (1113 GHz) transition. As previously indicated, the WILL and

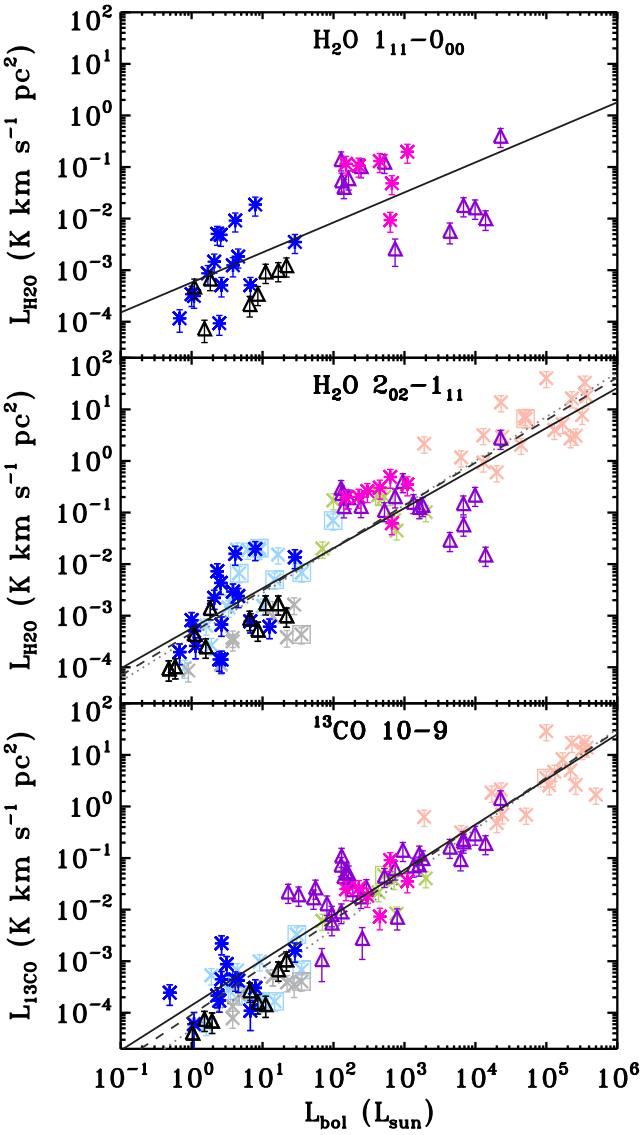


Figure 5.7: (*Top*) Line luminosity of the $H_2O$ $1_{11}$-$0_{00}$ (1113 GHz) line, (*middle*) $H_2O$ $2_{02}$-$1_{11}$ (988 GHz) transition and (*bottom*) $^{13}CO$ $J = 10$–9 spectra versus the source bolometric luminosity. The line luminosity for the WISH sources are over-plotted. The symbol code is the same as in Fig. 5.6. The solid line indicates the correlation of the logarithm of the total line luminosity, log($L$), and log($L_{bol}$) considering only the WILL and Cygnus samples while the dashed lighter line included the results from the WISH YSOs (results of the fits in Table 5.8). The dotted grey line shows the log($L$)-log($L_{bol}$) relation considering only the WISH survey.

Cygnus spectra of this water line are more affected by absorption from the colder envelope than higher excited transitions, causing the decrease of the slope value. In particular, five Class I Cygnus YSOs with relatively high $L_{bol}$ are characterised with low $L_{H_2O}$ values. The spectra of three of these outliers show strong absorptions and the other two objects (Cyg GR06 03 and Cyg GR05 11) have surprisingly narrow profiles with no broad component. These two sources are also outliers for the $H_2O$ $2_{02}$-$1_{11}$ transition due to their narrow profiles.

Within the WILL sample, a separation between the Class 0 and Class I protostars is observed for both water transitions. The Class I objects have lower $L_{H_2O}$ values than their less evolved counterparts, as already seen for the WISH low-mass protostars. In the case of the Cygnus sample, no significant distinction between the Class 0 and Class I-type objects is seen, although the former YSOs have larger $L_{H_2O}$ values. Regarding the $^{13}$CO $J = 10$–9 transition, the $L_{^{13}CO}$ values do not show a segregation between Class 0 and I objects.

In general, the WILL and Cygnus results overlap to those obtained for the WISH YSOs with similar $L_{bol}$ with fit results which are similar within the uncertainties (solid, dashed and dotted lines in Fig. 5.7). Therefore, the comparison with WISH confirms that the results derived in chapter 4 hold for a larger sample of sources, strengthening, from the statistical point of view, the conclusions derived from the line luminosity analysis. The $^{13}$CO $J = 10$–9 line shows the largest significance and $r$ coefficient (as well as number of detected sources).

As for the WISH data, the integrated intensity of the area constituting the broad velocity component of the $H_2O$ and $^{13}$CO $J = 10$–9 spectra is converted to line luminosity, $L_{broad}$. A correlation between this parameter and $L_{bol}$ is also measured for the $H_2O$ $1_{11}$-$0_{00}$, $2_{02}$-$1_{11}$ and $^{13}$CO $J = 10$–9 lines but with lower significance because the number of Cygnus sources considered has decreased (see parameters in right-column of Table 5.8 and Fig. 5.13 in the Appendix). In the case of the $H_2O$ $1_{11}$-$0_{00}$ transition, the slope of the correlation increases if just $L_{broad}$ is considered, becoming similar to that measured for the other studied transitions. The reason is that the previous outlier Cygnus Class I sources do not contribute to this calculation since their profiles do not show a broad velocity component. The parameters of the log-log correlations for the $H_2O$ $2_{02}$-$1_{11}$ line considering either $L_{H_2O}$ or $L_{broad}$ are similar within the uncertainty. This result confirms that the total water emission is dominated by the cavity shock component (see Table 5.5).

The $^{13}$CO $J = 10$–9 $L_{broad}$ does not significantly correlate with $L_{bol}$ because the number of spectra with detected line wings is small (eight out of 61). Therefore, the $^{13}$CO $J = 10$–9 line luminosity is dominated by envelope emission rather than by entrained outflowing gas emission.

## 5.4. Discussion

### 5.4.1. Comparison with WISH results

Most of the results obtained from the analysis and interpretation of the $H_2O$ and CO observations for the WISH sample have been evaluated and confirmed with the study of the WILL and Cygnus data. Starting with the shapes of the water spectra, we also concluded that the profiles for a given source are similar but scaled up or down in intensity with a consistent set of kinematic components. This indicates that the dynamical properties of the gas probed by the observed transitions are similar for each YSO and that in principle just the line with the highest signal-to-noise can be chosen to characterise the outflow/shock-related kinematics (see Table 5.2 and Mottram et al. 2014). Three types of kinematical components, corresponding to quiescent envelope, cavity shock and spot shock, are detected in the WILL sources. On the other hand, only envelope and cavity shocks emission are identified in the studied water observations of the Cygnus sample. We can exclude that the absence of spot shock components in the Cygnus observations is due to *S/N* limitations because, as presented in Sect. 5.2.2, these data have at least comparable (1113 GHz line) or a factor of >3 higher (988 GHz line) *S/N* than that of WILL. This is in line with the conclusions of chapter 4 based on the study of the excited water lines. In that case, the spectra of only one intermediate-mass YSO NGC 2071, a bright object located at half the distance of Cygnus, showed conclusive evidence of a spot shock component (EHV feature type). Therefore, the spot shock emission may not be detected in YSOs located further than 1 kpc away because this concentrated emission is affected by beam dilution. Alternatively, the absence of spot shock components could also be due to the fact that most of the Cygnus YSOs are in a later evolutionary stage (Class I type) and the percentage of detections of spot shocks is generally lower than that in Class 0 sources, as confirmed by the WISH and WILL low-mass Class I protostars. A medium-broad outflow component identified by van der Tak et al. (2013) in absorption in the ground-state lines of the WISH

high-mass YSOs may also be from spot shocks. However, this component is not conclusively seen in any of the excited water lines, so the identification in these sources remains uncertain.

Regarding the width of the water line profiles, we corroborate that both $FWHM_b$ and *FWZI* values are spread across a wide range of velocities (∼5–80 km s$^{-1}$ and ∼5–150 km s$^{-1}$, respectively), a similar interval to that measured for WISH, and with no trend with luminosity over 5 orders of magnitude. The scatter may be related to the geometry and intrinsic properties of each source (inclination of the outflows, opening angle, etc.). Despite the scatter, the line profiles of the WILL and Cygnus Class 0 type objects are broader than those of their more evolved Class I counterparts by typically 5–10 km s$^{-1}$, especially for the broad velocity component. As concluded from the WISH YSOs, this suggest differences in the dynamical conditions dominating the shocked material of Class 0 and Class I YSOs. This decrease of the line profile with the evolution is independent of the mass of the studied sample and of the excitation of the water lines (Mottram et al. 2014).

Moving to the cavity shock component, the average contribution of this component to the total integrated intensity of the WILL and Cygnus water lines is larger than that measured for WISH. The remaining fraction of intensity mainly comes from the spot component in the case of the low-mass Class 0 protostars and from the envelope for the other sub-samples of YSOs, as we concluded from WISH (Mottram et al. 2014). Interestingly, the results obtained from the cavity shock component are in general similar across a large and diverse sample of YSOs. This may indicate that common physical (dynamical) processes are taking place along the outflow system, shaping the water line profiles, which do not seem to depend on the luminosity or envelope mass of the source.

Finally, a strong correlation between the line luminosity, $L$, and $L_{bol}$ is measured across the WILL and Cygnus samples, as for WISH. This relation holds and becomes more statistically significant when the three surveys are combined. Similarly, the fraction of the luminosity corresponding to the cavity shock component, $L_{broad}$, correlates with $L_{bol}$ for the WILL and Cygnus samples. However, when considering only the WILL and Cygnus surveys, the obtained slope from the log($L$)-log($L_{bol}$) relation is smaller than that obtained for WISH. In addition, a separation between the line luminosity of the WILL Class 0 and Class I protostars is observed for the $H_2O$ transition but not for the $^{13}$CO line. This, together with the reduction of spot shock component detections in more evolved sources, suggests that the decrease in water emission, $L_{H_2O}$, from Class 0 to Class I objects is caused by a drop of the velocity of the gas constituting the outflow at later evolutionary stages (i.e. outflows become less energetic) rather than by the decrease of the envelope mass and density, as Mottram et al. (2014) concluded.

### 5.4.2. WILL and Cygnus samples

The water and CO observations allow us to compare the type of YSOs composing the WILL, Cygnus and WISH samples as well as derive some particular properties about these groups of objects.

The studied CO and $H_2O$ line profiles of the WILL Class 0 protostars are in general narrower (from 5 to 20 km s$^{-1}$) than those of their WISH low-mass analogues (see Fig. 5.3). The percentage of $^{12}$CO $J = 10$–9 spectra decomposed into several velocity components is significantly smaller as well (42% versus 72%). These results and the fact that the CO and $H_2O$ $1_{10}$-$1_{01}$ (557 GHz) data have comparable *S/N* to those of WISH suggest that the WISH low-mass Class 0 sample contains a larger number of sources with unusually energetic outflows. Therefore, the intrinsic properties of the WISH and WILL Class 0 objects may be different. On the other hand, the results from the WISH and WILL Class I protostars are comparable, suggesting that the type of objects composing both samples could be similar. A difference between the WISH and WILL Class I observations is that spot shock components offset from the source velocity are detected for three sources of the former sub-sample but have not been identified in any YSO from the latter sub-group.

In the case of the Cygnus Class 0 objects, the line profiles of the C$^{18}$O $J = 9$–8 line and envelope component of the $^{13}$CO $J = 10$–9 transition show similar *FWHM* values as those measured for the WISH high-mass YSOs, which are generally classified as Class 0 type objects. However, given the small number of Cygnus Class 0 sources, no further comparison can be performed between these objects. On the other hand, the line profiles of the $^{13}$CO, C$^{18}$O and $H_2O$ observations

for the Cygnus Class I YSOs are comparable to those measured for the WISH intermediate-mass and low-mass Class I objects. The number of Cygnus sources whose $^{13}$CO $J = 10$–9 spectra show a broad velocity component is smaller than that measured for the WISH high-mass YSOs, for which is present in all line profiles. In addition, the $^{13}$CO $J = 10$–9 transition was detected for half of observed Cygnus sources, a similar percentage as that found for the WISH low-mass Class I protostars. Therefore, we conclude that the Cygnus sample is mainly composed by a collection of intermediate- and even low-mass YSOs in a Class I type evolutionary stage, i.e. sources with less massive envelopes and especially less energetic outflows.

### 5.4.3. Environmental exploration of the Cygnus X region

The Cygnus survey allows us to investigate whether the specific physical conditions of different parts across this star-formation region are reflected in the observed $^{13}$CO and $H_2O$ spectra. As indicated in the introduction, Cygnus X is a perfect laboratory to perform environment studies due to the heterogeneity of its structure and the possibility of removing biases related to distance. Ultimately, the information extracted from the observed line profiles contributes to the characterisation of the region.

Starting with $^{13}$CO $J = 10$–9, Fig. 5.8 shows the location of the observed YSOs on the 24 $\mu$m map of the Cygnus X region. The different evolutionary stages of these objects are indicated with two types of symbols: circles are Class 0 and triangles Class I YSOs. Non-detections are presented in green. Most of the targeted YSOs of this survey as well as most of the detections and Class 0 type objects (7/8) are located in the CygX-North cloud (targets designed as "GR01"). In this region, characterised by filamentary structure and large chains of protostellar candidates, star formation is more active than in the South cloud, influenced by the Cyg OB2 association (Kryukova et al. 2014, and references therein). Interestingly, the YSOs with detection in $^{13}$CO located in the North cloud show negative and positive $v_{\rm LSR}$, which means that these objects belong to different structures present along the light of sight (see also Schneider et al. 2006). As expected, the non-detected YSOs of this GR01 are those with the lowest $L_{\rm bol}$ values and later evolutionary stage. Due to the lack of information about their $v_{\rm LSR}$ values, we cannot determine whether the sources with non-detection in $^{13}$CO $J = 10$–9 situated in the CygX-North are equally distributed across the different velocity structures or are mostly located in either of these layers. This analysis will be useful to further characterise these structures and have a better understanding of this region. Regarding those YSOs not detected in $^{13}$CO and located in the center and south of Cygnus, they are generally in a late Class I type evolutionary stage but with different luminosities.

Figure 5.9 presents the sources with detection in the $H_2O$ $2_{02}$-$1_{11}$ (988 GHz) transition. The symbol code is the same as in Fig. 5.8 (green also indicates non-detections). In pink are shown the Cygnus sources for which the *FWZI* is lower than 40 km s$^{-1}$ and in cyan those with *FWZI* above that velocity. The orange triangle symbols highlight the four YSOs with bright and surprisingly narrow profiles (*FWZI* $\leq$ 12 km s$^{-1}$ and *FWHM* $\leq$ 8 km s$^{-1}$) with no broad component. Consistent with the previous discussion, this plot shows that most of the cyan symbols (wider profiles) are concentrated in the northern cloud of Cygnus, where a larger number of YSOs with energetic outflows are forming. In general the water line profiles of these objects can be decomposed into two velocities components, i.e. a cavity shock component is identified. Regarding the detection statistics across the sample, we previously indicated that most of the Class 0 objects detected in water (7/8) are located in the North region. For the Class I sub-sample, almost half of these detected YSOs belong to that region as well, while the remaining Class I sources are spread across the other regions of Cygnus X. Independently of the evolutionary stage, the sources detected in water are generally luminous objects ($L_{\rm bol}$>100 $L_\odot$). Similarly as for the $^{13}$CO $J = 10$–9 line, the non-detections are predominantly less massive sources in Class I or even later evolutionary stages.

Finally, the preliminary study of the four YSOs with particularly narrow profiles (orange triangles of Fig. 5.9) suggests that the water emission is caused by a PDR rather than coming from the protostar itself. The lack of broad velocity component for those profiles supports the idea that the emission does not come from an actual YSO. Therefore, these sources are either too massive and significantly evolved, such as for GR02 01, GR04 02 or GR05 11 (Motte et al. 2007; Schneider

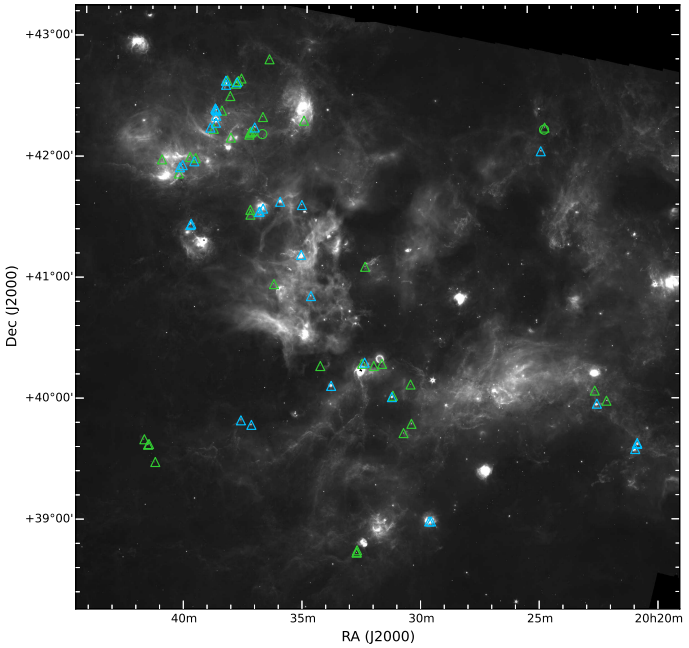


Figure 5.8: Distribution of the 41 YSOs for which the $^{13}$CO $J = 10$–9 line is detected (cyan) and those objects with no detection (green) plotted on top of the 24 micron map of Cygnus X star formation region observed with *Spitzer*. The circle and triangle symbols tag the Class 0 and Class I type YSOs, respectively.

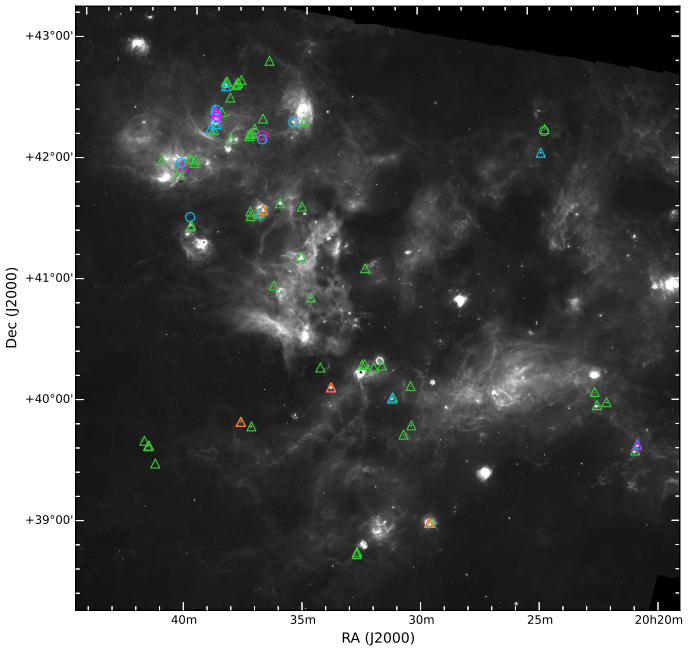


Figure 5.9: Same as Fig. 5.8 but plotting the 25 YSOs for which the $H_2O$ $2_{02}$-$1_{11}$ (988 GHz) transition is detected (cyan and magenta colours) together with those sources with no detection in this line (green). In magenta are shown the objects for which the *FWZI* of the 988 GHz spectra is $< 40$ km s$^{-1}$ and in cyan those with *FWZI* $> 40$ km s$^{-1}$. The four Class I YSOs with surprisingly narrow line profiles (*FWZI* $\leq 12$km s$^{-1}$) and without cavity shock component are plotted in orange.

et al. 2012), or have a nearby HII region which affects their excitation conditions (as for GR06 03; Motte et al. 2007). Further investigation is therefore required to unveil the properties and true nature of these sources.

To summarise, from the preliminary characterisation of the Cygnus X region, we confirm that the studied sample of YSOs is constituted by low- and intermediate-mass Class I objects. The majority of the detections are located in the North cloud, characterised by a more recent and intense

star formation activity.

## 5.5. Conclusions

The analysis of the $H_2O$ and CO HIFI observations of the WILL protostars and the Cygnus YSOs in terms of line profile and line luminosity allows us to evaluate previous results obtained for the WISH survey using a more uniform and statistically supported framework. The following results obtained for the WISH YSOs are confirmed by the studied WILL and Cygnus samples:

- The different water transitions of a given source have similar line profiles and number of velocity components. While the WILL low-mass protostars show three types of velocity components (quiescent envelope, cavity shock and spot shock), for the Cygnus low-, intermediate-mass YSOs only the envelope and cavity shock components are identified. The lack of spot shock component detections for the Cygnus observations may be due to beam dilution effects or to the fact that a large percentage of these objects are in a late evolutionary stage (Class I).

- More than 80% of the total water emission is generated by gas in (non-dissociative) shocks along the outflow cavity wall, independent of the luminosity of the source. The physical origin of the remaining emission is primarily from spot shocks in the case of the low-mass Class 0 objects and mainly envelope for the other type of YSOs.

- The results derived for the cavity shock component such as its width, the scatter of the $FWHM_b$ values and the fraction of this emission contributing to the total $L_{H_2O}$ suggest that the physical processes regulating the dynamical properties of outflow cavity walls seem independent of the luminosity or envelope mass of the source (i.e. the characteristics of the broad velocity component are similar across the studied sample of sources).

- The line emission of the $H_2O$ and $^{13}CO$ $J = 10$–9 lines strongly correlate with $L_{bol}$. The slope of this log-log relation is slightly smaller than that obtained for WISH. The interpretation of these results is ongoing.

- A decrease of $H_2O$ emission, $L_{H_2O}$, from Class 0 to Class I in the low-mass protostars is likely due to the reduction of the velocity of the gas constituting the outflow rather than by a decrease of the envelope mass and density of the object (Mottram et al. 2014).

We conclude that the WILL Class 0 sample is composed of protostars with (on-average) less energetic outflows than those constituting the WISH low-mass Class 0, while the intrinsic properties of the WILL and WISH Class I objects are more similar. On the other hand, the Cygnus survey is mostly composed of intermediate-mass (and even low-mass) YSOs in a late evolutionary stage (Class I type). This explains the relatively low percentage of $^{13}CO$ $J = 10$–9 and $H_2O$ detections (~45% of the observed sources). Finally, the preliminary environmental study of the Cygnus X region indicates that most of the $H_2O$ and $^{13}CO$ detections, Cygnus Class 0 objects and those which the broader water line profiles are generally located in the North cloud of this complex. This is consistent with the the fact that the star formation is more active and spontaneous in the North cloud than for CygX-South.

## Acknowledgments

This work is supported by the European Community's Seventh Framework Programme FP7/2007-2013 under grant agreement 238258 (LASSIE) and by the Space Research Organisation Netherlands (SRON). Astrochemistry in Leiden is supported by the Netherlands Research School for Astronomy (NOVA), by a Royal Netherlands Academy of Arts and Sciences (KNAW) professor prize, by EU A-ERC grant 291141 CHEMPLAN and by a Spinoza grant and grant 614.001.008

from the Netherlands Organisation for Scientific Research (NWO). HIFI has been designed and built by a consortium of institutes and university departments from across Europe, Canada and the United States under the leadership of SRON Netherlands Institute for Space Research, Groningen, The Netherlands and with major contributions from Germany, France and the US. Consortium members are: Canada: CSA, U.Waterloo; France: CESR, LAB, LERMA, IRAM; Germany: KOSMA, MPIfR, MPS; Ireland, NUI Maynooth; Italy: ASI, IFSI-INAF, Osservatorio Astrofisico di Arcetri- INAF; Netherlands: SRON, TUD; Poland: CAMK, CBK; Spain: Observatorio Astronómico Nacional (IGN), Centro de Astrobiología (CSIC-INTA). Sweden: Chalmers University of Technology - MC2, RSS & GARD; Onsala Space Observatory; Swedish National Space Board, Stockholm University - Stockholm Observatory; Switzerland: ETH Zurich, FHNW; USA: Caltech, JPL, NHSC.

# 5.A. *FWZI* analysis

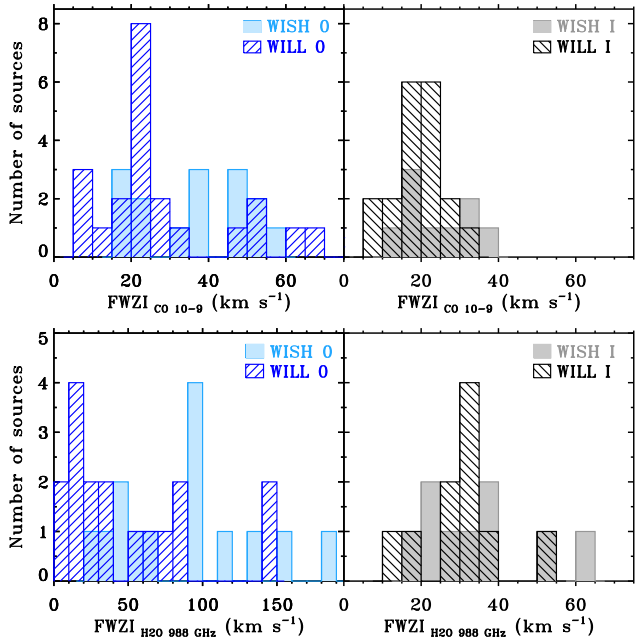


Figure 5.10: Histograms comparing the *FWZI* values for the $^{12}$CO $J = 10$–9 line (*top*-panels) and $H_2O$ $2_{02}$-$1_{11}$ (988 GHz) transition (*bottom*-panels) for the WILL and WISH samples. The *left*-panels show the *FWZI* of the WILL Class 0 protostars (dashed blue histogram) and those of the WISH low-mass Class 0 sources (light blue histograms). The *right*-panels compare the *FWZI* of the WILL low-mass Class I protostars (dashed black histogram) to those of the WISH Class I sources (light grey histogram). For the $H_2O$ $2_{02}$-$1_{11}$ transition for the Class 0 objects, the *FWZI* values are binned to 10 km s$^{-1}$. For the Class I protostars and $^{12}$CO line, the results are binned to 5 km s$^{-1}$.

## 5.A.1. $H_2O$ spectra

The *FWZI* parameter is calculated for all observed water transitions of the WILL and Cygnus surveys and the results are compared to those obtained for the WISH objects.

The bottom panels of Fig. 5.10 present the *FWZI* values calculated for the $H_2O$ $2_{02}$-$1_{11}$ (988 GHz) transition of the Class 0 protostars taken from the WILL and WISH low-mass samples (bottom-left histogram) and their Class I counterparts (bottom-right histogram). The range of velocities covered by the WISH Class 0 protostars is larger than that of the WILL analogues and ~60% of the 988 GHz WISH spectra show *FWZI* > 80 km s$^{-1}$, percentage which decreases to ~29% for the WILL Class 0 objects. The fact that the 988 GHz WILL spectra are narrower than those of WISH could be due to the difference in the *S/N* of these observations, which is higher for latter survey. However, the observations of the 557 GHz water transition have comparable *S/N* for both WILL and WISH observations and still the line wings of the WILL data are narrower than those of WISH. This suggests that the WISH low-mass Class 0 sub-sample may contain a larger number of sources with particularly energetic outflows (which show "bullet" emission) than the WILL Class 0 sub-sample. On the other hand, the *FWZI* measured for the WISH and WILL Class I objects (bottom-right histogram of Fig. 5.10) are comparable, independently of the water transition and its *S/N*. This indicates that offset spot shock components are not detected for the WILL Class I objects because this type of shocks are less common in more evolved YSOs. Both results are in line with the $FWHM_b$ analysis.

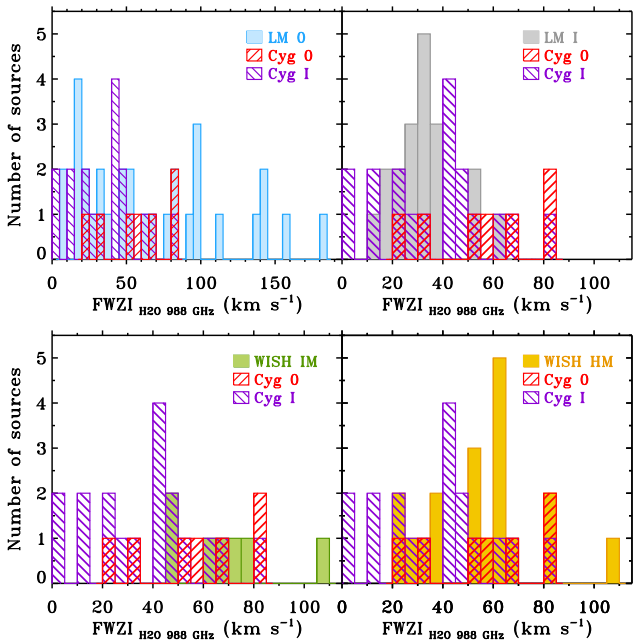


Figure 5.11: Same as Fig. 5.5, but comparing the $H_2O$ $2_{02}$-$1_{11}$ (988 GHz) *FWZI* of the Cygnus Class 0 (Cyg 0) and Cygnus Class I (Cyg I) samples to WILL and WISH low-mass Class 0 protostars (LM 0; *top-left*), WILL and WISH low-mass Class I objects (LM I; *top-right*), WISH intermediate-mass (WISH IM; *bottom-left*) and high-mass (WISH HM; *bottom-right*) YSOs.

The *FWZI* values calculated for the $H_2O$ $2_{02}$-$1_{11}$ (988 GHz) spectra of the Cygnus sources are compared to those of the WILL and WISH low-mass sample of protostars, and to the WISH intermediate- and high-mass sub-samples in Fig. 5.5. The spectra of the Cygnus Class 0 YSOs (red dashed histogram) show *FWZI* values comparable to those measured for the WISH intermediate- (green histogram) and high-mass (yellow histogram) YSOs (bottom panels of Fig. 5.5 and Table 5.3). On the other hand, the data of the Cygnus Class I objects (purple dashed lines) are characterised by narrower profiles and the distribution of the *FWZI* is similar to that of the low-mass Class I protostars, but shifted by ∼10 km s$^{-1}$ to larger velocities (top-right histogram). Therefore, these results suggests that the bulk of the Cygnus sample is constituted of low- and intermediate-mass YSOs in a late evolutionary stage (Class I-type).

## 5.A.2. CO spectra

The *FWZI* values constrained for the $^{12}$CO $J = 10$–9 data of the WILL Class 0 and Class I protostars are compared to those constrained for the WISH low-mass analogues in the top histograms of Fig. 5.10. For the Class 0 protostars (top-left histogram), the range of velocities covered by the WILL spectra (blue dashed lines) is larger than that measured for their WISH equivalents (light blue lines). However, only 23% of the WILL Class 0 sources show profiles with *FWZI* > 30 km s$^{-1}$. This percentage increases up to 60% for the WISH Class 0 objects. For the Class I protostars, the distribution of the $^{12}$CO $J = 10$–9 *FWZI* values (top-right histogram) of both WILL and WISH samples peaks at similar velocities (with a shift of ∼5 km s$^{-1}$). Since the *S/N* of these observations is similar for both surveys, this confirms the results derived from the water lines: the WISH Class 0 sample may be composed by a larger number of sources with energetic outflows than their WILL analogues, while both WILL and WISH Class I samples have protostars with similar characteristics.

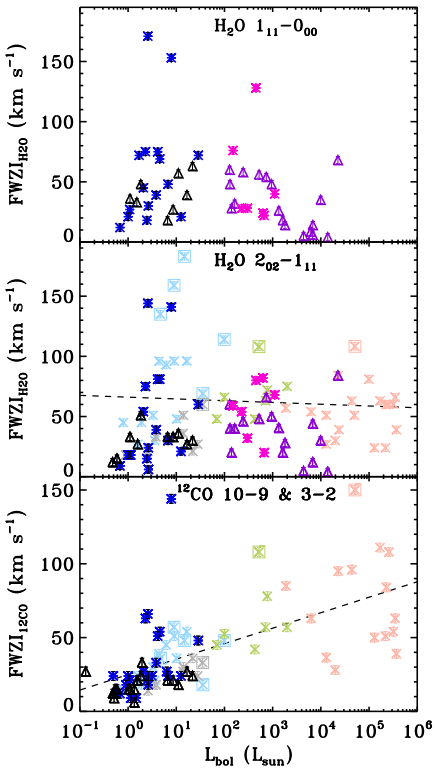


Figure 5.12: *FWZI* of the $H_2O$ $1_{11}$-$0_{00}$ (1113 GHz) line (*top*), the $H_2O$ $2_{02}$-$1_{11}$ (557 GHz) transition (*middle*) and the $^{12}CO$ $J = 10$–9 and $J = 3$–2 line (*bottom*) derived for the WILL, Cygnus and WISH YSOs as a function of source bolometric luminosity. The symbols and colour codes are the same as in Fig. 5.6. A linear fit to the data is indicated with a dash line to highlight any possible trend of *FWZI* with $L_{bol}$.

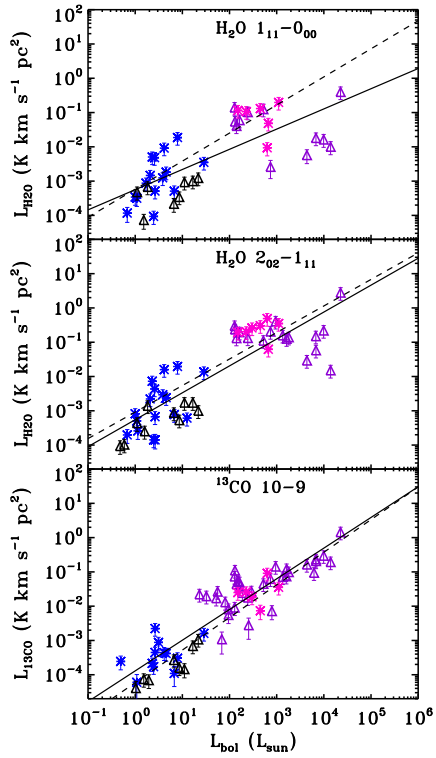


Figure 5.13: Same as Fig. 5.7 but including the relation between the line luminosity derived from the broad velocity component and $L_{bol}$ for only the WILL and Cygnus samples. The solid line indicates the linear correlation of the logarithm of the total line luminosity, log($L$), and log($L_{bol}$). The dashed line shows the log-log correlation of the luminosity measured for the broader Gaussian velocity component only ($L_{broad}$) and log($L_{bol}$).

Finally, Fig. 5.12 shows the *FWZI* values of the WILL and Cygnus objects together with those of WISH, for the $H_2O$ $1_{11}$-$0_{00}$ (1113 GHz; top), $2_{02}$-$1_{11}$ (988 GHz; middle) and $^{12}CO$ $J = 10$–9 (bottom) lines as a function of source bolometric luminosity. As already seen for the WISH water data, the scatter of the *FWZI* values is large (from ~5 to 180 km s$^{-1}$) and likely related to the intrinsic properties of the source (inclination of the outflows, etc). In general, the *FWZI* of the Cygnus sample show a smaller range in velocities than that of the low-mass Class 0 protostars. In the case of the $^{12}CO$ $J = 10$–9, the *FWZI* of the WILL and WISH low-mass protostars are similarly scattered and cover a comparable interval of velocities.

# 5.B. WILL data

## 5.B.1. Specific sources

AQU 01: in the $H_2O$ $1_{10}$-$1_{01}$ spectrum an extra velocity component not seen in the other water transitions is detected. According to the line decomposition method (Sect. 5.2.4), that component would be considered a cavity shock component due to its width and position. However, this emission may come from IRAS 4A, a close by protostar which falls into the 557 GHz beam. For smaller beams this component disappears, which means that the emission is offset from the centre of the beam, reenforcing the hypothesis that the emission comes from the nearby protostar. To conclude, the AQU 01 557 GHz spectrum is contaminated by the cavity or spot shock emission of IRAS 4A. In order to fix this issue we did not consider this component when designating the name and physical origin of the multiple velocity components also detected in the other water lines.

AQU 06: the cavity shock component is not detected over $3\sigma_{\rm rms}$ in the 557 GHz line, the only transition that seems to show a weak broad component. The spectra of the water lines is dominated by absorption and envelope emission, neither of which can be properly constrained with the line decomposition method. Therefore, other basic parameters such as *FWZI* and *W* are considered as rough estimations.

Per 02: the water spectra show a clear broad water emission coming from the outflows. However, the emission from the outflow of another source interacts with that generated by Per 02 causing a broad absorption that prevents from properly constraining the Gaussian parameters fitting the cavity shock component. Since any output value would not be reliable due to that strong and broad absorption, we exclude this protostar from our studied sample. Further details about this specific interaction and the analysis of maps of this region will be presented in the WILL overview paper (Mottram et al. in prep.).

Per 07: the $H_2O$ $1_{10}$-$1_{01}$ line is the only water transition detected and it shows an intense absorption feature along its broad velocity component. This absorption, offset from the source velocity, prevents from properly constraining the values of the Gaussian profile fitting the cavity shock component. Since no other water transition observed with a smaller beam is detected, we considered the measured value of $FWHM_{\rm b}$ as a lower limit of this parameters. Therefore, the results from the decomposition of this water line are not considered for further analysis.

Per 12: the broad cavity shock component detected in the 557 GHz is not observed in the other water transitions. This is again related to the differences in beam of those observations: in the case of the $1_{10}$-$1_{01}$ line, the beam is big enough to include a nearby source (IRAS 4A). The fitted cavity shock component does not belong to Per 12 but to IRAS 4A. For this reason, we do not consider this component in the analysis of the WILL data.

Finally, the W40 04, W40 05 and W40 07 are not considered as detections since only absorption is observed in the water lines.

Table 5.9: Observed and fitted properties of the WILL $H_2O$ $1_{11}$-$0_{00}$ and $H_2O$ $1_{10}$-$1_{01}$ lines.

| Source | $H_2O$ $1_{11}$-$0_{00}$ | | | | $H_2O$ $1_{10}$-$1_{01}$ | | | |
|---|---|---|---|---|---|---|---|---|
| | rms[a] (mK) | $T_{MB}^{peak}$ (K) | $\int T_{MB} dv$[b] (K km s$^{-1}$) | *FWZI* (km s$^{-1}$) | rms[a] (mK) | $T_{MB}^{peak}$ (K) | $\int T_{MB} dv$[b] (K km s$^{-1}$) | *FWZI* (km s$^{-1}$) |
| AQU 01 | 24 | 0.18 | 7.44 ± 0.20 | 171 | 10 | 0.19 | 6.76 ± 0.05 | 183 |
| AQU 02 | 27 | 0.17 | 1.91 ± 0.10 | 39 | 10 | 0.13 | 1.62 ± 0.03 | 51 |
| AQU 03 | 23 | < 0.07 | – | – | 5 | 0.02 | -0.07 ± 0.01 | 15 |
| AQU 04 | 26 | < 0.08 | – | – | 6 | 0.01 | -0.05 ± 0.01 | 12 |
| AQU 05 | 23 | 0.12 | 0.53 ± 0.07 | 21 | 6 | 0.06 | 0.35 ± 0.02 | 30 |
| AQU 06 | 24 | < 0.07 | – | – | 6 | 0.03 | 0.10 ± 0.02 | 21 |
| CHA 01 | 23 | < 0.07 | – | – | 5 | 0.04 | 0.32 ± 0.02 | 27 |
| CHA 02 | 24 | < 0.08 | – | – | 5 | < 0.02 | – | – |
| CRA 01 | 24 | 0.15 | 0.57 ± 0.07 | 18 | 6 | 0.07 | 0.39 ± 0.02 | 33 |
| OPH 02 | 24 | 0.22 | 2.29 ± 0.08 | 27 | 7 | 0.10 | 1.12 ± 0.02 | 39 |
| PER 01 | 24 | 0.16 | 3.45 ± 0.13 | 69 | 8 | 0.08 | 2.11 ± 0.03 | 84 |
| PER 03 | 35 | 0.69 | 35.09 ± 0.20 | 153 | 28 | 0.38 | 20.72 ± 0.04 | 159 |
| PER 04 | 24 | < 0.07 | – | – | 4 | < 0.01 | – | – |
| PER 05 | 26 | 0.17 | 1.75 ± 0.11 | 57 | 7 | 0.08 | 0.72 ± 0.02 | 27 |
| PER 06 | 26 | 0.10 | 0.41 ± 0.07 | 18 | 10 | 0.14 | 2.07 ± 0.03 | 66 |
| PER 08 | 26 | 0.20 | 1.88 ± 0.09 | 39 | 6 | 0.21 | 1.94 ± 0.02 | 48 |
| PER 09 | 27 | 0.15 | 2.32 ± 0.12 | 63 | 11 | 0.21 | 1.16 ± 0.02 | 39 |
| PER 10 | 25 | 0.11 | 0.96 ± 0.10 | 48 | 10 | 0.10 | 2.03 ± 0.03 | 75 |
| PER 11 | 24 | 1.23 | 17.26 ± 0.14 | 75 | 5 | 0.67 | 11.44 ± 0.04 | 87 |
| PER 12 | 28 | 0.11 | 0.60 ± 0.08 | 27 | 6 | 0.26 | 3.50 ± 0.03 | 66 |
| PER 13 | 25 | 0.10 | 0.22 ± 0.05 | 12 | 6 | 0.09 | 0.65 ± 0.02 | 33 |
| PER 14 | 21 | 0.10 | 1.28 ± 0.11 | 48 | 6 | 0.04 | 0.61 ± 0.03 | 63 |
| PER 15 | 25 | 0.10 | 1.64 ± 0.13 | 72 | 11 | 0.07 | 2.48 ± 0.04 | 105 |
| PER 16 | 23 | 0.05 | -0.16 ± 0.04 | 6 | 5 | 0.02 | 0.27 ± 0.03 | 72 |
| PER 17 | 28 | < 0.08 | – | – | 6 | 0.03 | 0.37 ± 0.02 | 42 |
| PER 18 | 24 | < 0.07 | – | – | 8 | 0.04 | 1.25 ± 0.04 | 123 |
| PER 19 | 26 | 0.12 | 0.90 ± 0.09 | 36 | 6 | 0.03 | 0.13 ± 0.02 | 24 |
| PER 20 | 23 | 0.40 | 9.52 ± 0.13 | 75 | 5 | 0.23 | 6.54 ± 0.03 | 75 |
| PER 21 | 26 | 0.19 | 2.75 ± 0.11 | 45 | 6 | 0.11 | 2.38 ± 0.03 | 54 |
| PER 22 | 22 | 0.13 | 0.96 ± 0.08 | 30 | 7 | 0.14 | 0.96 ± 0.02 | 42 |
| SCO 01 | 22 | < 0.07 | – | – | 5 | < 0.02 | – | – |
| SERS 01 | 23 | 0.04 | -0.49 ± 0.06 | 15 | 6 | 0.02 | 0.11 ± 0.03 | 54 |
| SERS 02 | 28 | 0.68 | 5.41 ± 0.13 | 72 | 9 | 0.73 | 9.03 ± 0.04 | 99 |
| TAU 01 | 24 | 0.12 | 0.39 ± 0.09 | 33 | 7 | 0.06 | 0.72 ± 0.03 | 78 |
| TAU 02 | 22 | < 0.07 | – | – | 5 | 0.03 | 0.14 ± 0.01 | 18 |
| TAU 03 | 22 | < 0.08 | – | – | 6 | 0.02 | 0.18 ± 0.02 | 27 |
| TAU 04 | 27 | < 0.08 | – | – | 5 | 0.02 | 0.07 ± 0.01 | 18 |
| TAU 06 | 27 | < 0.08 | – | – | 5 | 0.03 | 0.12 ± 0.01 | 12 |
| TAU 07 | 26 | < 0.08 | – | – | 6 | < 0.02 | – | – |
| TAU 08 | 23 | < 0.08 | – | – | 6 | < 0.02 | – | – |
| TAU 09 | 22 | < 0.07 | – | – | 5 | 0.03 | 0.16 ± 0.02 | 21 |
| W40 02 | 22 | 0.12 | -0.29 ± 0.07 | 21 | 7 | 0.08 | 0.47 ± 0.03 | 51 |
| W40 04 | 22 | 0.02 | -0.56 ± 0.06 | 14 | 6 | 0.03 | -0.05 ± 0.01 | 9 |
| W40 05 | 27 | 0.05 | -0.39 ± 0.06 | 15 | 6 | 0.03 | -0.14 ± 0.02 | 21 |
| W40 07 | 22 | < 0.07 | – | – | 6 | < 0.02 | – | – |

**Notes.** *FWZI* has been calculated by binning the spectra to 3 km s$^{-1}$. ($^a$) In 0.27 km s$^{-1}$ bin. ($^b$) Integrated over the interval of velocities defined by the *FWZI*.

Table 5.10: Observed and fitted properties of the WILL $H_2O$ $2_{02}$-$1_{11}$ and $H_2O$ $3_{12}$-$2_{21}$ lines.

| Source | $H_2O$ $2_{02}$-$1_{11}$ | | | | $H_2O$ $3_{12}$-$2_{21}$ | | | |
|---|---|---|---|---|---|---|---|---|
| | rms[a] (mK) | $T_{MB}^{peak}$ (K) | $\int T_{MB} dv$[b] (K km s$^{-1}$) | *FWZI* (km s$^{-1}$) | rms[a] (mK) | $T_{MB}^{peak}$ (K) | $\int T_{MB} dv$[b] (K km s$^{-1}$) | *FWZI* (km s$^{-1}$) |
| AQU 01 | 23 | 0.12 | 5.02 ± 0.17 | 144 | 111 | < 0.33 | – | – |
| AQU 02 | 22 | 0.24 | 3.41 ± 0.09 | 39 | 108 | 0.39 | 2.93 ± 0.34 | 27 |
| AQU 03 | 22 | < 0.07 | – | – | 107 | < 0.37 | – | – |
| AQU 04 | 24 | < 0.07 | – | – | 116 | < 0.35 | – | – |
| AQU 05 | 21 | 0.15 | 0.95 ± 0.06 | 18 | 102 | < 0.37 | – | – |
| AQU 06 | 20 | < 0.06 | – | – | 107 | < 0.37 | – | – |
| CHA 01 | 23 | 0.10 | 0.88 ± 0.08 | 27 | 99 | < 0.30 | – | – |
| CHA 02 | 22 | < 0.07 | – | – | 112 | < 0.34 | – | – |
| CRA 01 | 23 | 0.20 | 0.66 ± 0.06 | 15 | 99 | < 0.36 | – | – |
| OPH 02 | 22 | 0.24 | 2.68 ± 0.09 | 33 | 109 | 0.44 | 2.53 ± 0.31 | 24 |
| PER 01 | 24 | 0.24 | 3.43 ± 0.14 | 81 | 104 | < 0.31 | – | – |
| PER 03 | 40 | 0.53 | 27.89 ± 0.19 | 141 | 114 | 0.54 | 16.08 ± 0.76 | 126 |
| PER 04 | 23 | < 0.07 | – | – | 100 | < 0.30 | – | – |
| PER 05 | 25 | 0.24 | 2.46 ± 0.09 | 36 | 124 | < 0.37 | – | – |
| PER 06 | 23 | 0.16 | 1.24 ± 0.09 | 33 | 113 | < 0.35 | – | – |
| PER 08 | 26 | 0.22 | 2.45 ± 0.08 | 27 | 123 | 0.40 | 1.95 ± 0.30 | 18 |
| PER 09 | 29 | 0.19 | 1.43 ± 0.09 | 30 | 118 | < 0.35 | – | – |
| PER 10 | 22 | 0.10 | 1.11 ± 0.08 | 30 | 103 | < 0.36 | – | – |
| PER 11 | 21 | 1.47 | 22.61 ± 0.13 | 81 | 112 | 1.71 | 26.28 ± 0.51 | 63 |
| PER 12 | 25 | 0.14 | 0.72 ± 0.06 | 18 | 122 | < 0.37 | – | – |
| PER 13 | 25 | 0.12 | 0.28 ± 0.05 | 9 | 112 | < 0.34 | – | – |
| PER 14 | 23 | 0.12 | 1.99 ± 0.10 | 51 | 102 | < 0.31 | – | – |
| PER 15 | 74 | 0.12 | 2.95 ± 0.15 | 90 | 105 | < 0.32 | – | – |
| PER 16 | 22 | 0.08 | 0.37 ± 0.07 | 18 | 101 | 0.36 | 0.39 ± 0.19 | 9 |
| PER 17 | 24 | < 0.07 | – | – | 120 | < 0.35 | – | – |
| PER 18 | 24 | < 0.08 | – | – | 99 | < 0.30 | – | – |
| PER 19 | 25 | 0.09 | 0.62 ± 0.08 | 33 | 116 | < 0.35 | – | – |
| PER 20 | 24 | 0.38 | 10.39 ± 0.13 | 75 | 125 | 0.55 | 9.05 ± 0.49 | 57 |
| PER 21 | 23 | 0.16 | 3.15 ± 0.11 | 54 | 165 | < 0.50 | – | – |
| PER 22 | 22 | 0.13 | 0.96 ± 0.07 | 24 | 104 | < 0.31 | – | – |
| SCO 01 | 23 | < 0.07 | – | – | 103 | < 0.31 | – | – |
| SERS 01 | 20 | < 0.06 | – | – | 111 | < 0.33 | – | – |
| SERS 02 | 24 | 0.92 | 15.87 ± 0.11 | 60 | 117 | 0.66 | 12.37 ± 0.49 | 54 |
| TAU 01 | 23 | < 0.08 | – | – | 100 | < 0.34 | – | – |
| TAU 02 | 23 | 0.08 | 0.38 ± 0.05 | 12 | 102 | < 0.31 | – | – |
| TAU 03 | 23 | < 0.07 | – | – | 103 | < 0.31 | – | – |
| TAU 04 | 26 | < 0.08 | – | – | 114 | < 0.34 | – | – |
| TAU 06 | 26 | < 0.08 | – | – | 117 | < 0.35 | – | – |
| TAU 07 | 24 | 0.10 | 0.41 ± 0.06 | 15 | 124 | < 0.37 | – | – |
| TAU 08 | 23 | < 0.07 | – | – | 102 | < 0.31 | – | – |
| TAU 09 | 21 | < 0.07 | – | – | 106 | < 0.32 | – | – |
| W40 02 | 22 | 0.10 | 0.71 ± 0.07 | 21 | 103 | < 0.31 | – | – |
| W40 04 | 24 | 0.10 | 0.16 ± 0.04 | 6 | 107 | < 0.37 | – | – |
| W40 05 | 22 | < 0.07 | – | – | 127 | < 0.38 | – | – |
| W40 07 | 22 | < 0.07 | – | – | 91 | < 0.27 | – | – |

**Notes.** *FWZI* has been calculated by binning the spectra to 3 km s$^{-1}$. ([a]) In 0.27 km s$^{-1}$ bin. ([b]) Integrated over the interval of velocities defined by the *FWZI*.

Table 5.11: Observed and fitted properties of the WILL $^{12}$CO $J = 10$–9 and $^{12}$CO $J = 10$–9 spectra.

| Source | $^{12}$CO $J = 10$–9 | | | | $^{13}$CO $J = 10$–9 | | | |
|---|---|---|---|---|---|---|---|---|
| | rms[a] (mK) | $T_{MB}^{peak}$ (K) | $\int T_{MB} dv$[b] (K km s$^{-1}$) | *FWZI* (km s$^{-1}$) | rms[a] (mK) | $T_{MB}^{peak}$ (K) | $\int T_{MB} dv$[b] (K km s$^{-1}$) | *FWZI* (km s$^{-1}$) |
| AQU 01 | 97 | 0.53 | 8.43 ± 0.48 | 66 | 29 | < 0.09 | – | – |
| AQU 02 | 108 | 1.15 | 9.76 ± 0.34 | 33 | 30 | < 0.09 | – | – |
| AQU 03 | 89 | 0.35 | 0.80 ± 0.14 | 6 | 25 | < 0.08 | – | – |
| AQU 04 | 91 | < 0.31 | – | – | 25 | < 0.08 | – | – |
| AQU 05 | 91 | 0.73 | 4.43 ± 0.28 | 24 | 26 | < 0.08 | – | – |
| AQU 06 | 0 | 0.38 | 1.36 ± 0.25 | 18 | 0 | < 0.00 | – | – |
| CHA 01 | 104 | 0.67 | 3.90 ± 0.26 | 21 | 25 | < 0.08 | – | – |
| CHA 02 | 93 | 0.50 | 2.86 ± 0.33 | 33 | 25 | 0.10 | 0.19 ± 0.03 | 3 |
| CRA 01 | 94 | 2.84 | 10.26 ± 0.27 | 21 | 25 | 0.31 | 0.87 ± 0.04 | 6 |
| OPH 02 | 90 | 2.21 | 12.33 ± 0.26 | 21 | 26 | 0.22 | 0.87 ± 0.05 | 10 |
| PER 01 | 95 | 2.20 | 21.31 ± 0.43 | 54 | 25 | 0.18 | 0.64 ± 0.05 | 9 |
| PER 03 | 104 | 2.94 | 52.17 ± 0.69 | 144 | 30 | 0.11 | 0.47 ± 0.09 | 26 |
| PER 04 | 89 | 0.28 | 0.75 ± 0.17 | 9 | 24 | < 0.07 | – | – |
| PER 05 | 91 | 1.45 | 6.50 ± 0.25 | 18 | 25 | 0.11 | 0.22 ± 0.04 | 7 |
| PER 06 | 91 | 1.49 | 7.89 ± 0.26 | 21 | 25 | 0.15 | 0.41 ± 0.03 | 4 |
| PER 08 | 106 | 7.80 | 35.42 ± 0.30 | 27 | 27 | 0.28 | 1.06 ± 0.06 | 18 |
| PER 09 | 89 | 14.11 | 39.05 ± 0.28 | 24 | 25 | 0.74 | 1.65 ± 0.05 | 11 |
| PER 10 | 107 | 0.82 | 5.21 ± 0.29 | 24 | 25 | 0.11 | 0.17 ± 0.07 | 21 |
| PER 11 | 91 | 3.53 | 35.65 ± 0.42 | 51 | 26 | 0.15 | 0.68 ± 0.06 | 12 |
| PER 12 | 105 | 0.83 | 2.24 ± 0.26 | 21 | 29 | 0.15 | 0.09 ± 0.05 | 9 |
| PER 13 | 100 | 0.67 | 1.91 ± 0.19 | 12 | 28 | < 0.08 | – | – |
| PER 14 | 103 | 0.83 | 4.48 ± 0.28 | 24 | 28 | < 0.09 | – | – |
| PER 15 | 103 | < 0.31 | – | – | 30 | < 0.09 | – | – |
| PER 16 | 89 | 0.39 | 0.86 ± 0.17 | 9 | 25 | < 0.08 | – | – |
| PER 17 | 104 | 0.67 | 3.36 ± 0.29 | 27 | 28 | < 0.09 | – | – |
| PER 18 | 104 | 1.31 | 6.98 ± 0.28 | 24 | 28 | 0.09 | 0.38 ± 0.06 | 14 |
| PER 19 | 107 | 0.55 | 3.11 ± 0.23 | 15 | 27 | < 0.08 | – | – |
| PER 20 | 87 | 1.47 | 22.00 ± 0.44 | 63 | 24 | 0.11 | 0.33 ± 0.04 | 7 |
| PER 21 | 161 | 0.92 | 7.55 ± 0.47 | 27 | 25 | < 0.09 | – | – |
| PER 22 | 105 | 2.62 | 12.22 ± 0.25 | 18 | 23 | 0.18 | 0.69 ± 0.07 | 21 |
| SCO 01 | 104 | 0.60 | 2.12 ± 0.20 | 12 | 25 | < 0.08 | – | – |
| SERS 01 | 106 | 0.64 | 4.21 ± 0.31 | 27 | 29 | < 0.09 | – | – |
| SERS 02 | 110 | 5.71 | 61.76 ± 0.42 | 48 | 29 | 0.37 | 2.02 ± 0.09 | 29 |
| TAU 01 | 105 | 1.54 | 4.24 ± 0.26 | 21 | 29 | 0.13 | 0.33 ± 0.04 | 6 |
| TAU 02 | 92 | 0.69 | 1.90 ± 0.20 | 12 | 23 | < 0.07 | – | – |
| TAU 03 | 93 | < 0.28 | – | – | 23 | < 0.07 | – | – |
| TAU 04 | 105 | 0.52 | 2.43 ± 0.22 | 15 | 27 | < 0.08 | – | – |
| TAU 06 | 89 | 1.04 | 2.28 ± 0.22 | 15 | 24 | < 0.08 | – | – |
| TAU 07 | 104 | 0.71 | 3.04 ± 0.22 | 15 | 27 | < 0.08 | – | – |
| TAU 08 | 103 | 0.37 | 1.12 ± 0.17 | 9 | 24 | < 0.07 | – | – |
| TAU 09 | 92 | 1.18 | 4.23 ± 0.22 | 15 | 24 | 0.10 | 0.18 ± 0.07 | 22 |
| W40 02 | 94 | 6.19 | 10.80 ± 0.28 | 24 | 24 | < 0.07 | – | – |
| W40 04 | 106 | 12.13 | 28.84 ± 0.29 | 24 | 29 | 2.49 | 2.80 ± 0.06 | 12 |
| W40 05 | 105 | 7.40 | 26.73 ± 0.29 | 24 | 29 | 0.79 | 1.11 ± 0.07 | 17 |
| W40 07 | 86 | 0.32 | 0.66 ± 0.17 | 9 | 24 | < 0.07 | – | – |

**Notes.** *FWZI* has been calculated by binning the spectra to 3 km s$^{-1}$. ($^a$) In 0.27 km s$^{-1}$ bin. ($^b$) Integrated over the interval of velocities defined by the *FWZI*.

Table 5.12: Observed and fitted properties of the WILL $H_2^{18}O$ $1_{10}$-$1_{01}$ and $C^{18}O$ $J = 9$–8 lines.

| Source | $H_2^{18}O$ $1_{10}$-$1_{01}$ | | | | $C^{18}O$ $J = 9$–8 | | | |
|---|---|---|---|---|---|---|---|---|
| | rms[a] (mK) | $T_{MB}^{peak}$ (K) | $\int T_{MB} dv$[b] (K km s$^{-1}$) | *FWZI* (km s$^{-1}$) | rms[a] (mK) | $T_{MB}^{peak}$ (K) | $\int T_{MB} dv$[b] (K km s$^{-1}$) | *FWZI* (km s$^{-1}$) |
| AQU 01 | 8 | < 0.02 | – | – | 26 | < 0.08 | – | – |
| AQU 02 | 5 | < 0.02 | – | – | 26 | < 0.08 | – | – |
| AQU 03 | 5 | < 0.02 | – | – | 22 | < 0.07 | – | – |
| AQU 04 | 5 | < 0.02 | – | – | 23 | < 0.08 | – | – |
| AQU 05 | 5 | < 0.02 | – | – | 24 | < 0.07 | – | – |
| AQU 06 | 5 | < 0.02 | – | – | 0 | < 0.00 | – | – |
| CHA 01 | 5 | < 0.02 | – | – | 26 | < 0.08 | – | – |
| CHA 02 | 5 | < 0.02 | – | – | 23 | < 0.07 | – | – |
| CRA 01 | 5 | < 0.02 | – | – | 24 | < 0.08 | – | – |
| OPH 02 | 5 | < 0.02 | – | – | 23 | < 0.07 | – | – |
| PER 01 | 5 | < 0.01 | – | – | 24 | < 0.08 | – | – |
| PER 03 | 5 | < 0.02 | – | – | 30 | < 0.09 | – | – |
| PER 04 | 4 | < 0.01 | – | – | 24 | < 0.07 | – | – |
| PER 05 | 5 | < 0.02 | – | – | 24 | < 0.07 | – | – |
| PER 06 | 5 | < 0.02 | – | – | 25 | < 0.09 | – | – |
| PER 08 | 5 | < 0.02 | – | – | 26 | < 0.08 | – | – |
| PER 09 | 5 | < 0.02 | – | – | 25 | < 0.08 | – | – |
| PER 10 | 5 | < 0.02 | – | – | 24 | < 0.08 | – | – |
| PER 11 | 6 | 0.05 | 0.49 ± 0.02 | 39 | 25 | < 0.08 | – | – |
| PER 12 | 5 | < 0.02 | – | – | 25 | < 0.08 | – | – |
| PER 13 | 5 | < 0.02 | – | – | 27 | < 0.08 | – | – |
| PER 14 | 5 | < 0.02 | – | – | 26 | < 0.08 | – | – |
| PER 15 | 5 | < 0.02 | – | – | 24 | < 0.08 | – | – |
| PER 16 | 5 | < 0.02 | – | – | 23 | < 0.08 | – | – |
| PER 17 | 5 | < 0.02 | – | – | 27 | < 0.08 | – | – |
| PER 18 | 4 | < 0.01 | – | – | 27 | < 0.08 | – | – |
| PER 19 | 5 | < 0.02 | – | – | 26 | < 0.08 | – | – |
| PER 20 | 5 | < 0.02 | – | – | 24 | < 0.07 | – | – |
| PER 21 | 5 | < 0.02 | – | – | 25 | < 0.08 | – | – |
| PER 22 | 5 | < 0.02 | – | – | 27 | < 0.08 | – | – |
| SCO 01 | 5 | < 0.02 | – | – | 25 | < 0.08 | – | – |
| SERS 01 | 5 | < 0.02 | – | – | 25 | < 0.08 | – | – |
| SERS 02 | 6 | 0.02 | 0.25 ± 0.02 | 30 | 25 | 0.10 | 0.28 ± 0.03 | 5 |
| TAU 01 | 4 | < 0.01 | – | – | 25 | < 0.08 | – | – |
| TAU 02 | 5 | < 0.01 | – | – | 25 | < 0.08 | – | – |
| TAU 03 | 5 | < 0.02 | – | – | 25 | < 0.08 | – | – |
| TAU 04 | 4 | < 0.01 | – | – | 26 | < 0.08 | – | – |
| TAU 06 | 5 | < 0.02 | – | – | 23 | < 0.07 | – | – |
| TAU 07 | 5 | < 0.02 | – | – | 27 | < 0.08 | – | – |
| TAU 08 | 5 | < 0.02 | – | – | 23 | < 0.08 | – | – |
| TAU 09 | 5 | < 0.02 | – | – | 23 | < 0.07 | – | – |
| W40 02 | 5 | < 0.02 | – | – | 23 | < 0.07 | – | – |
| W40 04 | 5 | < 0.02 | – | – | 26 | 0.35 | 0.43 ± 0.04 | 7 |
| W40 05 | 6 | < 0.02 | – | – | 24 | 0.15 | 0.05 ± 0.05 | 12 |
| W40 07 | 5 | < 0.02 | – | – | 24 | < 0.07 | – | – |

**Notes.** *FWZI* has been calculated by binning the spectra to 3 km s$^{-1}$. ([a]) In 0.27 km s$^{-1}$ bin. ([b]) Integrated over the interval of velocities defined by the *FWZI*.

Table 5.13: Gaussian decomposition results for the WILL $^{12}$CO $J = 10$–9 data.

| Source | Comp.[a] | *FWHM* | $v_{\rm peak}$ | $v_{\rm LSR}$ | $^{12}$CO $J = 10$–9 | |
|---|---|---|---|---|---|---|
| | | | | | $T_{\rm MB}^{\rm peak}$ | $\int T_{\rm MB} {\rm d}v^b$ |
| | | (km s$^{-1}$) | (km s$^{-1}$) | (km s$^{-1}$) | (K) | (K km s$^{-1}$) |
| AQU 01 | C | 35.1 ± 2.5 | 1.3 ± 1.0 | 7.6 | 0.21 ± 0.01 | 7.80 ± 0.74 |
| AQU 02 | E | 3.8 ± 0.3 | 8.5 ± 0.1 | 7.9 | 0.77 ± 0.05 | 3.07 ± 0.35 |
| | C | 17.1 ± 1.4 | 9.5 ± 0.5 | 7.9 | 0.38 ± 0.04 | 6.88 ± 0.95 |
| AQU 03 | E | 3.6 ± 0.8 | 7.6 ± 0.3 | 7.2 | 0.20 ± 0.04 | 0.78 ± 0.22 |
| AQU 05 | C | 6.5 ± 0.4 | 8.0 ± 0.2 | 7.4 | 0.57 ± 0.03 | 3.95 ± 0.30 |
| CHA 01 | E | 4.7 ± 0.3 | 5.3 ± 0.1 | 4.9 | 0.63 ± 0.04 | 3.16 ± 0.29 |
| CHA 02 | E | 4.1 ± 0.4 | 2.2 ± 0.2 | 3.0 | 0.45 ± 0.04 | 1.97 ± 0.24 |
| CRA 01 | E | 3.5 ± 0.1 | 5.7 ± 0.0 | 5.6 | 2.32 ± 0.04 | 8.67 ± 0.24 |
| OPH 02 | E | 4.7 ± 0.1 | 4.0 ± 0.1 | 4.2 | 1.74 ± 0.03 | 8.62 ± 0.27 |
| | C | 10.3 ± 0.8 | 5.1 ± 0.4 | 4.2 | 0.35 ± 0.01 | 3.82 ± 0.28 |
| PER 01 | S | 5.6 ± 0.2 | 3.8 ± 0.1 | 4.1 | 1.54 ± 0.04 | 9.22 ± 0.36 |
| | C | 28.9 ± 1.5 | 2.2 ± 0.5 | 4.1 | 0.40 ± 0.03 | 12.38 ± 1.02 |
| PER 03 | E | 1.8 ± 0.1 | 5.3 ± 0.0 | 5.2 | 1.84 ± 0.09 | 3.49 ± 0.26 |
| | S | 7.0 ± 0.4 | 8.6 ± 0.2 | 5.2 | 1.20 ± 0.04 | 8.92 ± 0.57 |
| | S | 16.7 ± 0.6 | 62.1 ± 0.2 | 5.2 | 0.75 ± 0.02 | 13.27 ± 0.60 |
| | C | 35.0 ± 1.5 | 16.4 ± 0.7 | 5.2 | 0.52 ± 0.02 | 19.25 ± 1.19 |
| PER 05 | E | 4.7 ± 0.2 | 7.5 ± 0.1 | 7.2 | 1.19 ± 0.03 | 6.02 ± 0.26 |
| PER 06 | E | 3.0 ± 0.2 | 7.5 ± 0.1 | 7.3 | 1.13 ± 0.05 | 3.60 ± 0.26 |
| | C | 13.3 ± 1.2 | 6.3 ± 0.4 | 7.3 | 0.33 ± 0.04 | 4.68 ± 0.70 |
| PER 08 | E | 2.2 ± 0.0 | 7.7 ± 0.0 | 7.7 | 5.28 ± 0.09 | 12.53 ± 0.32 |
| | C | 8.2 ± 0.2 | 7.6 ± 0.0 | 7.7 | 2.56 ± 0.08 | 22.36 ± 0.84 |
| PER 09 | E | 2.4 ± 0.0 | 7.8 ± 0.0 | 7.5 | 12.30 ± 0.30 | 30.95 ± 0.21 |
| | C | 7.1 ± 0.4 | 6.8 ± 0.2 | 7.5 | 0.81 ± 0.02 | 6.09 ± 0.36 |
| PER 10 | C | 7.3 ± 0.4 | 7.4 ± 0.2 | 8.6 | 0.60 ± 0.03 | 4.63 ± 0.37 |
| PER 11 | E | 3.4 ± 0.1 | 7.3 ± 0.0 | 7.4 | 1.81 ± 0.05 | 6.57 ± 0.29 |
| | C | 14.7 ± 0.2 | 5.1 ± 0.1 | 7.4 | 1.75 ± 0.04 | 27.43 ± 0.73 |
| PER 12 | E | 3.1 ± 0.3 | 8.0 ± 0.1 | 7.8 | 0.51 ± 0.05 | 1.68 ± 0.23 |
| PER 13 | E | 2.7 ± 0.3 | 8.2 ± 0.1 | 7.9 | 0.58 ± 0.05 | 1.65 ± 0.21 |
| PER 14 | E | 2.0 ± 0.3 | 6.0 ± 0.1 | 6.2 | 0.60 ± 0.06 | 1.31 ± 0.22 |
| | C | 14.0 ± 1.9 | 6.3 ± 0.7 | 6.2 | 0.22 ± 0.03 | 3.33 ± 0.68 |
| PER 16 | E | 4.0 ± 0.7 | 7.1 ± 0.3 | 7.1 | 0.23 ± 0.04 | 0.98 ± 0.23 |
| PER 17 | E | 1.9 ± 0.3 | 6.6 ± 0.1 | 6.4 | 0.52 ± 0.06 | 1.06 ± 0.19 |
| PER 18 | C | 5.3 ± 0.2 | 7.2 ± 0.1 | 6.7 | 1.12 ± 0.04 | 6.29 ± 0.31 |
| PER 19 | C | 8.9 ± 0.8 | 8.1 ± 0.3 | 6.9 | 0.34 ± 0.03 | 3.25 ± 0.40 |
| PER 20 | E | 4.4 ± 0.2 | 9.6 ± 0.1 | 8.9 | 1.08 ± 0.05 | 5.07 ± 0.36 |
| | S | 7.2 ± 1.0 | 27.7 ± 0.3 | 8.9 | 0.33 ± 0.04 | 2.58 ± 0.46 |
| | S | 11.4 ± 1.8 | -5.3 ± 0.8 | 8.9 | 0.27 ± 0.04 | 3.27 ± 0.69 |
| | C | 27.7 ± 3.0 | 19.0 ± 2.0 | 8.9 | 0.39 ± 0.02 | 11.46 ± 1.43 |
| PER 21 | C | 10.1 ± 0.8 | 8.1 ± 0.3 | 8.7 | 0.62 ± 0.04 | 6.64 ± 0.65 |
| PER 22 | E | 2.6 ± 0.1 | 10.0 ± 0.0 | 9.8 | 1.85 ± 0.10 | 5.15 ± 0.40 |
| | C | 8.0 ± 0.5 | 10.6 ± 0.2 | 9.8 | 0.85 ± 0.10 | 7.32 ± 0.97 |
| SCO 01 | E | 3.0 ± 0.3 | 3.9 ± 0.1 | 3.4 | 0.55 ± 0.05 | 1.74 ± 0.23 |
| SERS 01 | E | 2.9 ± 0.5 | 8.4 ± 0.2 | 8.2 | 0.35 ± 0.05 | 1.10 ± 0.26 |
| SERS 02 | S | 5.8 ± 0.2 | 8.3 ± 0.0 | 7.8 | 2.91 ± 0.09 | 17.82 ± 0.72 |
| | C | 17.0 ± 0.3 | 8.5 ± 0.1 | 7.8 | 2.39 ± 0.09 | 43.27 ± 1.78 |

**Notes.** ($^a$) The types of components are: C = cavity shock; E = envelope emission; S = spot shock; A = envelope absorption. ($^b$) Integrated intensity of each velocity component approximated to the gaussian fit.

Table 5.14: Gaussian decomposition results for the WILL $^{12}$CO $J = 10$–9 data (continuation).

| Source | Comp.[a] | *FWHM* | $v_{\rm peak}$ | $v_{\rm LSR}$ | $^{12}$CO $J = 10$–9 | |
|---|---|---|---|---|---|---|
| | | | | | $T_{\rm MB}^{\rm peak}$ | $\int T_{\rm MB} {\rm d}v^b$ |
| | | (km s$^{-1}$) | (km s$^{-1}$) | (km s$^{-1}$) | (K) | (K km s$^{-1}$) |
| TAU 01 | E | 2.4 ± 0.1 | 6.8 ± 0.0 | 6.8 | 1.36 ± 0.05 | 3.50 ± 0.21 |
| TAU 02 | E | 2.2 ± 0.2 | 7.0 ± 0.1 | 7.1 | 0.61 ± 0.05 | 1.45 ± 0.18 |
| TAU 04 | C | 6.9 ± 0.7 | 6.7 ± 0.3 | 6.4 | 0.34 ± 0.03 | 2.49 ± 0.35 |
| TAU 06 | E | 2.8 ± 0.2 | 7.3 ± 0.1 | 7.0 | 0.85 ± 0.04 | 2.52 ± 0.19 |
| TAU 07 | E | 4.7 ± 0.3 | 7.2 ± 0.1 | 6.3 | 0.60 ± 0.04 | 3.04 ± 0.29 |
| TAU 08 | E | 3.9 ± 0.7 | 6.4 ± 0.3 | 5.5 | 0.27 ± 0.04 | 1.12 ± 0.26 |
| TAU 09 | E | 3.9 ± 0.2 | 5.9 ± 0.1 | 5.6 | 0.94 ± 0.04 | 3.97 ± 0.23 |
| W40 02 | E | 0.9 ± 0.0 | 5.1 ± 0.0 | 4.8 | 4.82 ± 0.09 | 4.51 ± 0.13 |
| | C | 5.5 ± 0.3 | 4.9 ± 0.1 | 4.8 | 0.95 ± 0.05 | 5.58 ± 0.40 |

**Notes.** $(^a)$ The types of components are: C = cavity shock; E = envelope emission; S = spot shock; A = envelope absorption. $(^b)$ Integrated intensity of each velocity component approximated to the gaussian fit.

Table 5.15: Gaussian decomposition results for the WILL $^{13}$CO $J = 10$–9 and C$^{18}$O $J = 9$–8 data.

| Source | Comp.[a] | *FWHM* | $v_{\rm peak}$ | $v_{\rm LSR}$ | $^{13}$CO $J = 10$–9 | |
|---|---|---|---|---|---|---|
| | | | | | $T_{\rm MB}^{\rm peak}$ | $\int T_{\rm MB} {\rm d}v^b$ |
| | | (km s$^{-1}$) | (km s$^{-1}$) | (km s$^{-1}$) | (K) | (K km s$^{-1}$) |
| CHA 02 | E | 2.2 ± 0.4 | 2.6 ± 0.2 | 3.0 | 0.08 ± 0.01 | 0.19 ± 0.04 |
| CRA 01 | E | 2.7 ± 0.1 | 5.8 ± 0.0 | 5.6 | 0.30 ± 0.01 | 0.87 ± 0.05 |
| OPH 02 | C | 6.5 ± 0.4 | 3.5 ± 0.2 | 4.2 | 0.13 ± 0.01 | 0.89 ± 0.08 |
| PER 01 | E | 4.3 ± 0.3 | 4.2 ± 0.1 | 4.1 | 0.15 ± 0.01 | 0.70 ± 0.06 |
| PER 05 | E | 2.4 ± 0.3 | 7.9 ± 0.1 | 7.2 | 0.11 ± 0.01 | 0.27 ± 0.04 |
| PER 06 | E | 3.2 ± 0.3 | 6.8 ± 0.1 | 7.3 | 0.14 ± 0.01 | 0.47 ± 0.06 |
| PER 08 | E | 2.0 ± 0.2 | 7.9 ± 0.1 | 7.7 | 0.18 ± 0.02 | 0.38 ± 0.06 |
| | C | 10.3 ± 1.4 | 8.0 ± 0.5 | 7.7 | 0.07 ± 0.01 | 0.75 ± 0.16 |
| PER 09 | E | 1.4 ± 0.1 | 7.9 ± 0.0 | 7.5 | 0.58 ± 0.02 | 0.87 ± 0.05 |
| | C | 5.3 ± 0.5 | 7.2 ± 0.2 | 7.5 | 0.14 ± 0.02 | 0.81 ± 0.13 |
| PER 10 | E | 2.7 ± 0.5 | 8.7 ± 0.2 | 8.6 | 0.07 ± 0.01 | 0.20 ± 0.05 |
| PER 11 | E | 4.9 ± 0.4 | 7.8 ± 0.2 | 7.4 | 0.12 ± 0.01 | 0.63 ± 0.07 |
| PER 12 | E | 0.8 ± 0.2 | 8.2 ± 0.1 | 7.8 | 0.16 ± 0.03 | 0.14 ± 0.04 |
| PER 20 | E | 2.8 ± 0.3 | 8.8 ± 0.1 | 8.9 | 0.10 ± 0.01 | 0.29 ± 0.04 |
| PER 22 | C | 6.9 ± 0.5 | 9.8 ± 0.2 | 9.8 | 0.10 ± 0.01 | 0.72 ± 0.07 |
| SERS 02 | E | 2.6 ± 0.2 | 8.0 ± 0.1 | 7.8 | 0.25 ± 0.01 | 0.69 ± 0.07 |
| | C | 16.1 ± 1.5 | 9.5 ± 0.6 | 7.8 | 0.08 ± 0.01 | 1.34 ± 0.19 |
| TAU 01 | E | 2.4 ± 0.3 | 7.1 ± 0.1 | 6.8 | 0.12 ± 0.01 | 0.30 ± 0.05 |
| TAU 09 | E | 1.9 ± 0.3 | 5.7 ± 0.1 | 5.6 | 0.09 ± 0.01 | 0.18 ± 0.04 |
| | | | | | C$^{18}$O $J = 9$–8 | |
| SERS 02 | C | 7.2 ± 1.1 | 8.4 ± 0.5 | 7.8 | 0.05 ± 0.01 | 0.41 ± 0.08 |

**Notes.** $(^a)$ The types of components are: C = cavity shock; E = envelope emission; S = spot shock; A = envelope absorption. $(^b)$ Integrated intensity of each velocity component approximated to the gaussian fit.

Table 5.16: Gaussian decomposition results for the WILL $H_2O$ spectra.

| Source | Comp.[a] | $FWHM$ | $v_{peak}$ | $v_{LSR}$ | $H_2O$ $1_{10}$-$1_{01}$ | | $H_2O$ $1_{11}$-$0_{00}$ | | $H_2O$ $2_{02}$-$1_{11}$ | | $H_2O$ $3_{12}$-$2_{21}$ | |
|---|---|---|---|---|---|---|---|---|---|---|---|---|
| | | | | | $T_{MB}^{peak}$ | $\int T_{MB} dv^b$ | $T_{MB}^{peak}$ | $\int T_{MB} dv^b$ | $T_{MB}^{peak}$ | $\int T_{MB} dv^b$ | $T_{MB}^{peak}$ | $\int T_{MB} dv^b$ |
| | | (km s$^{-1}$) | (km s$^{-1}$) | (km s$^{-1}$) | (K) | (K km s$^{-1}$) | (K) | (K km s$^{-1}$) | (K) | (K km s$^{-1}$) | (K) | (K km s$^{-1}$) |
| AQU 01 | S | 6.8 ± 2.5 | 0.5 ± 0.8 | 7.6 | 0.06 ± 0.02 | 0.46 ± 0.22 | 0.02 ± 0.03 | 0.14 ± 0.19 | 0.05 ± 0.03 | 0.33 ± 0.22 | < 0.33 | < 5.69 |
| | S | 45.6 ± 18.6 | 63.2 ± 7.5 | 7.6 | 0.02 ± 0.01 | 0.46 ± 0.22 | 0.02 ± 0.03 | 0.14 ± 0.19 | 0.05 ± 0.03 | 0.33 ± 0.22 | < 0.33 | < 5.69 |
| | C | 79.1 ± 6.0 | -11.1 ± 3.0 | 7.6 | 0.05 ± 0.01 | 0.46 ± 0.22 | 0.09 ± 0.01 | 0.14 ± 0.19 | 0.06 ± 0.01 | 0.33 ± 0.22 | < 0.33 | < 5.69 |
| AQU 02 | S | 12.5 ± 3.3 | 7.1 ± 0.6 | 7.9 | 0.03 ± 0.00 | 0.97 ± 0.00 | < 0.08 | < 2.57 | 0.11 ± 0.05 | 1.53 ± 0.75 | < 0.33 | < 10.23 |
| | C | 20.7 ± 0.9 | 6.9 ± 0.3 | 7.9 | 0.11 ± 0.01 | 0.97 ± 0.00 | 0.13 ± 0.01 | 2.57 ± 0.00 | 0.09 ± 0.05 | 1.53 ± 0.75 | 0.15 ± 0.03 | 10.23 ± 0.00 |
| AQU 05 | C | 9.7 ± 0.7 | 9.1 ± 0.3 | 7.4 | 0.06 ± 0.01 | 0.58 ± 0.09 | 0.11 ± 0.02 | 1.12 ± 0.24 | 0.10 ± 0.01 | 1.03 ± 0.13 | < 0.31 | < 7.44 |
| AQU 06 | C | 27.2 ± 7.6 | 13.3 ± 3.2 | 8.3 | 0.01 ± 0.00 | 0.28 ± 0.12 | < 0.07 | < 4.96 | < 0.06 | < 4.23 | < 0.32 | < 21.91 |
| CHA 01 | C | 16.2 ± 2.1 | 9.5 ± 0.9 | 4.9 | 0.02 ± 0.00 | 0.38 ± 0.09 | < 0.07 | < 2.84 | 0.05 ± 0.01 | 0.82 ± 0.18 | < 0.30 | < 12.15 |
| CRA 01 | C | 14.2 ± 2.4 | 7.3 ± 0.9 | 5.6 | 0.02 ± 0.00 | 0.31 ± 0.09 | 0.05 ± 0.01 | 0.69 ± 0.25 | 0.01 ± 0.01 | 0.18 ± 0.19 | < 0.30 | < 10.59 |
| OPH 02 | C | 14.5 ± 0.5 | 2.9 ± 0.2 | 4.2 | 0.09 ± 0.00 | 1.36 ± 0.08 | 0.19 ± 0.01 | 2.87 ± 0.21 | 0.17 ± 0.01 | 2.58 ± 0.16 | 0.18 ± 0.04 | 2.82 ± 0.63 |
| PER 01 | S | 6.0 ± 1.2 | 5.3 ± 0.5 | 4.1 | 0.03 ± 0.00 | 0.39 ± 0.00 | < 0.07 | < 1.10 | 0.10 ± 0.02 | 0.66 ± 0.18 | < 0.31 | < 4.68 |
| | C | 39.0 ± 1.9 | -1.8 ± 0.8 | 4.1 | 0.05 ± 0.00 | 0.39 ± 0.00 | 0.09 ± 0.01 | 1.10 ± 0.00 | 0.06 ± 0.01 | 0.66 ± 0.18 | < 0.31 | < 4.68 |
| PER 03 | S | 25.2 ± 0.9 | 59.1 ± 0.4 | 5.2 | 0.17 ± 0.01 | 4.62 ± 0.25 | 0.39 ± 0.01 | 10.36 ± 0.44 | 0.32 ± 0.01 | 8.46 ± 0.40 | 0.20 ± 0.03 | 5.26 ± 0.76 |
| | C | 31.7 ± 0.9 | 22.0 ± 0.3 | 5.2 | 0.32 ± 0.01 | 4.62 ± 0.25 | 0.62 ± 0.01 | 10.36 ± 0.44 | 0.49 ± 0.01 | 8.46 ± 0.40 | 0.19 ± 0.03 | 5.26 ± 0.76 |
| | S | 59.7 ± 6.6 | -27.8 ± 3.0 | 5.2 | 0.08 ± 0.01 | 4.62 ± 0.25 | 0.39 ± 0.01 | 10.36 ± 0.44 | 0.32 ± 0.01 | 8.46 ± 0.40 | 0.20 ± 0.03 | 5.26 ± 0.76 |
| PER 05 | C | 13.4 ± 0.7 | 9.0 ± 0.3 | 7.2 | 0.06 ± 0.01 | 0.82 ± 0.09 | 0.15 ± 0.02 | 2.18 ± 0.27 | 0.17 ± 0.01 | 2.38 ± 0.20 | < 0.37 | < 12.57 |
| PER 06 | S | 7.2 ± 1.1 | 9.3 ± 0.3 | 7.3 | 0.08 ± 0.01 | 0.60 ± 0.14 | < 0.08 | < 1.40 | < 0.07 | < 1.28 | < 0.34 | < 6.12 |
| | C | 34.1 ± 2.6 | 5.9 ± 1.0 | 7.3 | 0.05 ± 0.01 | 0.60 ± 0.14 | < 0.08 | < 1.40 | 0.04 ± 0.01 | 1.28 ± 0.00 | < 0.34 | < 6.12 |
| PER 08 | S | 6.5 ± 0.5 | 9.0 ± 0.2 | 7.7 | 0.11 ± 0.01 | 0.76 ± 0.09 | 0.10 ± 0.03 | 0.68 ± 0.22 | 0.13 ± 0.02 | 0.90 ± 0.17 | 0.34 ± 0.11 | 2.31 ± 0.78 |
| | C | 21.5 ± 1.1 | 5.7 ± 0.5 | 7.7 | 0.08 ± 0.01 | 0.76 ± 0.09 | 0.08 ± 0.01 | 0.68 ± 0.22 | 0.08 ± 0.01 | 0.90 ± 0.17 | < 0.37 | < 2.31 |
| PER 09 | E | 4.3 ± 1.3 | 7.2 ± 0.5 | 7.5 | 0.03 ± 0.00 | 0.36 ± 0.00 | < 0.08 | < 0.87 | 0.10 ± 0.03 | 0.45 ± 0.18 | < 0.36 | < 3.81 |
| | C | 19.1 ± 1.5 | 6.8 ± 0.6 | 7.5 | 0.05 ± 0.01 | 0.36 ± 0.00 | 0.09 ± 0.01 | 0.87 ± 0.00 | 0.05 ± 0.01 | 0.45 ± 0.18 | < 0.36 | < 3.81 |
| PER 10 | S | 12.2 ± 3.2 | 7.0 ± 0.7 | 8.6 | 0.05 ± 0.02 | 0.69 ± 0.28 | < 0.08 | < 2.36 | < 0.07 | < 2.04 | < 0.31 | < 9.47 |
| | C | 27.5 ± 3.3 | 6.6 ± 1.0 | 8.6 | 0.05 ± 0.02 | 0.69 ± 0.28 | 0.04 ± 0.01 | 2.36 ± 0.00 | 0.04 ± 0.01 | 2.04 ± 0.00 | < 0.31 | < 9.47 |
| PER 11 | S | 5.0 ± 0.2 | 8.7 ± 0.1 | 7.4 | 0.29 ± 0.02 | 1.56 ± 0.11 | 0.37 ± 0.06 | 1.98 ± 0.31 | 0.72 ± 0.03 | 3.84 ± 0.23 | 0.40 ± 0.16 | 2.12 ± 0.87 |
| | C | 21.8 ± 0.2 | 4.5 ± 0.1 | 7.4 | 0.47 ± 0.01 | 1.56 ± 0.11 | 0.70 ± 0.02 | 1.98 ± 0.31 | 0.76 ± 0.02 | 3.84 ± 0.23 | 1.04 ± 0.08 | 2.12 ± 0.87 |
| PER 12 | C | 8.9 ± 1.5 | 9.7 ± 0.6 | 7.8 | 0.02 ± 0.00 | 0.47 ± 0.00 | 0.08 ± 0.02 | 0.80 ± 0.24 | 0.09 ± 0.02 | 0.82 ± 0.23 | < 0.37 | < 8.23 |
| | O | 19.5 ± 0.4 | 14.4 ± 0.2 | 7.8 | 0.16 ± 0.00 | 0.47 ± 0.00 | < 0.09 | < 0.80 | < 0.08 | < 0.82 | < 0.37 | < 8.23 |
| PER 13 | E | 3.5 ± 0.7 | 8.5 ± 0.3 | 7.9 | 0.05 ± 0.01 | 0.17 ± 0.06 | 0.06 ± 0.03 | 0.21 ± 0.12 | 0.09 ± 0.02 | 0.33 ± 0.10 | < 0.34 | < 2.92 |
| | C | 9.5 ± 0.8 | 11.2 ± 0.6 | 7.9 | 0.05 ± 0.01 | 0.17 ± 0.06 | < 0.08 | < 0.21 | < 0.08 | < 0.33 | < 0.34 | < 2.92 |

**Notes.** [a] The types of components are: C = cavity shock; E = envelope emission; S = spot shock; A = envelope absorption; O = a component generated from another source only detected in the 557 GHz line due to the size of the beam. [b] Integrated intensity of each velocity component approximated to the gaussian fit.

Table 5.17: Gaussian decomposition results for the WILL $H_2O$ spectra (continuation).

| Source | Comp.[a] | $FWHM$ | $v_{peak}$ | $v_{LSR}$ | $H_2O$ $1_{10}$-$1_{01}$ | | $H_2O$ $1_{11}$-$0_{00}$ | | $H_2O$ $2_{02}$-$1_{11}$ | | $H_2O$ $3_{12}$-$2_{21}$ | |
|---|---|---|---|---|---|---|---|---|---|---|---|---|
| | | | | | $T_{MB}^{peak}$ | $\int T_{MB} dv^b$ | $T_{MB}^{peak}$ | $\int T_{MB} dv^b$ | $T_{MB}^{peak}$ | $\int T_{MB} dv^b$ | $T_{MB}^{peak}$ | $\int T_{MB} dv^b$ |
| | | (km s$^{-1}$) | (km s$^{-1}$) | (km s$^{-1}$) | (K) | (K km s$^{-1}$) | (K) | (K km s$^{-1}$) | (K) | (K km s$^{-1}$) | (K) | (K km s$^{-1}$) |
| PER 14 | S | 3.5 ± 2.2 | 3.5 ± 0.9 | 6.2 | 0.02 ± 0.01 | 0.06 ± 0.05 | < 0.06 | < 0.56 | < 0.07 | < 0.62 | < 0.31 | < 2.73 |
| | C | 30.9 ± 2.3 | 8.3 ± 1.1 | 6.2 | 0.02 ± 0.01 | 0.06 ± 0.05 | 0.04 ± 0.01 | 0.56 ± 0.00 | 0.06 ± 0.01 | 0.62 ± 0.00 | < 0.31 | < 2.73 |
| PER 15 | S | 12.8 ± 3.1 | 11.8 ± 1.4 | 6.8 | 0.03 ± 0.01 | 0.44 ± 0.14 | < 0.08 | < 2.47 | < 0.22 | < 7.14 | < 0.32 | < 10.18 |
| | S | 19.3 ± 4.2 | 65.3 ± 1.2 | 6.8 | 0.03 ± 0.01 | 0.44 ± 0.14 | < 0.08 | < 2.47 | < 0.22 | < 7.14 | < 0.32 | < 10.18 |
| | C | 59.7 ± 8.9 | 27.2 ± 4.5 | 6.8 | 0.03 ± 0.00 | 0.44 ± 0.14 | 0.03 ± 0.00 | 2.47 ± 0.00 | 0.04 ± 0.00 | 7.14 ± 0.00 | < 0.32 | < 10.18 |
| PER 16 | S | 10.9 ± 4.2 | 5.0 ± 1.8 | 7.1 | 0.02 ± 0.00 | 0.47 ± 0.00 | < 0.07 | < 1.93 | 0.04 ± 0.01 | 0.42 ± 0.21 | < 0.30 | < 8.34 |
| | C | 59.2 ± 13.5 | 13.6 ± 5.7 | 7.1 | 0.01 ± 0.00 | 0.47 ± 0.00 | < 0.07 | < 1.93 | < 0.07 | < 0.42 | < 0.30 | < 8.34 |
| PER 17 | C | 24.7 ± 3.9 | 10.5 ± 1.6 | 6.4 | 0.02 ± 0.00 | 0.49 ± 0.12 | < 0.08 | < 5.24 | < 0.07 | < 4.56 | < 0.36 | < 22.29 |
| PER 18 | S | 17.5 ± 7.4 | 16.1 ± 2.3 | 6.7 | 0.02 ± 0.01 | 0.32 ± 0.17 | < 0.07 | < 3.17 | < 0.07 | < 3.19 | < 0.30 | < 13.14 |
| | C | 63.2 ± 12.5 | 19.9 ± 3.9 | 6.7 | 0.02 ± 0.01 | 0.32 ± 0.17 | < 0.07 | < 3.17 | < 0.07 | < 3.19 | < 0.30 | < 13.14 |
| PER 19 | C | 13.2 ± 1.9 | 6.5 ± 0.7 | 6.9 | 0.01 ± 0.00 | 0.20 ± 0.06 | 0.08 ± 0.02 | 1.18 ± 0.29 | 0.05 ± 0.01 | 0.68 ± 0.22 | < 0.35 | < 11.64 |
| PER 20 | S | 21.2 ± 0.5 | 27.0 ± 0.3 | 8.9 | 0.17 ± 0.00 | 3.84 ± 0.13 | 0.32 ± 0.01 | 7.29 ± 0.27 | 0.31 ± 0.01 | 6.98 ± 0.28 | 0.27 ± 0.04 | 6.21 ± 1.02 |
| | C | 26.0 ± 1.6 | 0.6 ± 0.9 | 8.9 | 0.09 ± 0.00 | 3.84 ± 0.13 | 0.09 ± 0.01 | 7.29 ± 0.27 | 0.13 ± 0.01 | 6.98 ± 0.28 | 0.12 ± 0.04 | 6.21 ± 1.02 |
| PER 21 | S | 5.2 ± 1.0 | 23.9 ± 0.4 | 8.7 | 0.02 ± 0.01 | 0.12 ± 0.04 | 0.06 ± 0.02 | 0.36 ± 0.12 | 0.04 ± 0.02 | 0.23 ± 0.10 | 0.36 ± 0.11 | 1.97 ± 0.71 |
| | C | 24.1 ± 0.9 | 7.6 ± 0.3 | 8.7 | 0.09 ± 0.00 | 0.12 ± 0.04 | 0.12 ± 0.01 | 0.36 ± 0.12 | 0.11 ± 0.01 | 0.23 ± 0.10 | < 0.50 | < 1.97 |
| PER 22 | C | 15.5 ± 1.3 | 11.4 ± 0.5 | 9.8 | 0.05 ± 0.01 | 0.80 ± 0.12 | 0.07 ± 0.01 | 1.19 ± 0.24 | 0.06 ± 0.01 | 1.03 ± 0.16 | < 0.31 | < 12.18 |
| | C | 42.4 ± 9.3 | 10.5 ± 3.9 | 8.2 | 0.01 ± 0.00 | 1.06 ± 0.00 | < 0.07 | < 3.78 | < 0.06 | < 3.24 | < 0.33 | < 17.73 |
| SERS 02 | C | 16.8 ± 0.2 | 11.1 ± 0.1 | 7.8 | 0.68 ± 0.01 | 12.23 ± 0.24 | 0.68 ± 0.02 | 12.13 ± 0.44 | 0.78 ± 0.02 | 14.05 ± 0.33 | 0.63 ± 0.09 | 11.22 ± 1.62 |
| TAU 01 | C | 18.7 ± 1.6 | 4.5 ± 0.7 | 6.8 | 0.04 ± 0.00 | 0.82 ± 0.10 | 0.04 ± 0.01 | 0.75 ± 0.20 | < 0.07 | < 3.33 | < 0.30 | < 14.16 |
| TAU 02 | C | 7.6 ± 1.5 | 8.1 ± 0.6 | 7.1 | 0.02 ± 0.01 | 0.18 ± 0.06 | < 0.07 | < 1.26 | 0.05 ± 0.01 | 0.36 ± 0.13 | < 0.31 | < 5.86 |
| TAU 03 | C | 18.1 ± 4.7 | 8.2 ± 1.9 | 7.4 | 0.01 ± 0.00 | 0.25 ± 0.10 | < 0.07 | < 3.03 | < 0.07 | < 3.16 | < 0.31 | < 14.01 |
| TAU 04 | C | 10.6 ± 3.9 | 7.1 ± 1.5 | 6.4 | 0.01 ± 0.00 | 0.12 ± 0.06 | < 0.08 | < 2.18 | < 0.08 | < 2.08 | < 0.34 | < 9.14 |
| TAU 06 | C | 6.2 ± 1.2 | 6.8 ± 0.4 | 7.0 | 0.03 ± 0.01 | 0.19 ± 0.06 | < 0.08 | < 1.26 | < 0.08 | < 1.24 | < 0.35 | < 5.47 |
| TAU 09 | E | 5.3 ± 1.3 | 6.2 ± 0.6 | 5.6 | 0.02 ± 0.00 | 0.12 ± 0.04 | < 0.07 | < 0.92 | < 0.07 | < 0.87 | < 0.32 | < 4.24 |
| W40 02 | C | 22.3 ± 2.3 | 6.2 ± 0.9 | 4.8 | 0.03 ± 0.00 | 0.78 ± 0.13 | 0.05 ± 0.01 | 1.17 ± 0.27 | < 0.07 | < 3.77 | < 0.31 | < 17.42 |

**Notes.** ([a]) The types of components are: C = cavity shock; E = envelope emission; S = spot shock; A = envelope absorption; O = a component generated from another source only detected in the 557 GHz line due to the size of the beam. ([b]) Integrated intensity of each velocity component approximated to the gaussian fit.

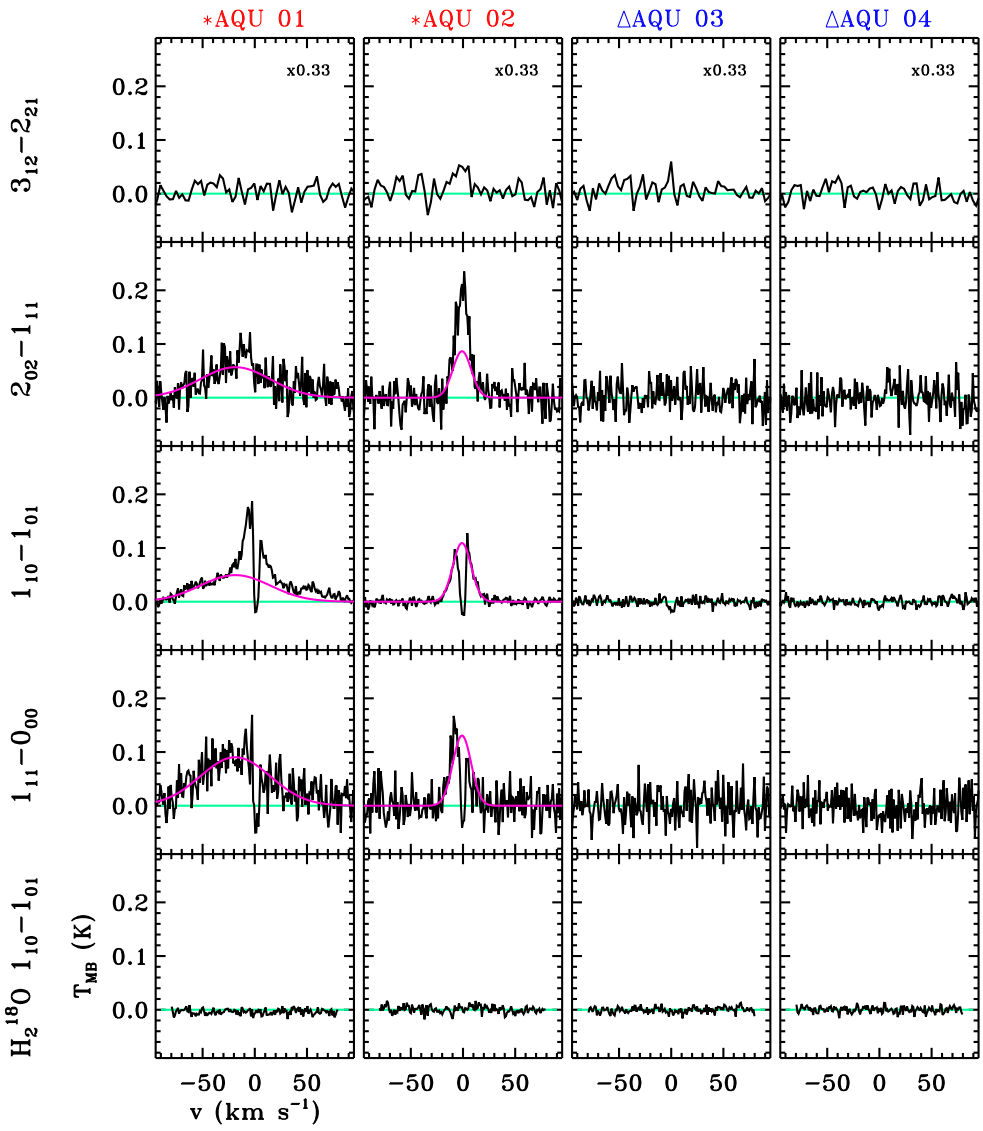


Figure 5.14: $H_2^{18}O$ $1_{10}$-$1_{01}$, $H_2O$ $1_{11}$-$0_{00}$ (1113 GHz), $1_{10}$-$1_{01}$ (557 GHz), $2_{02}$-$1_{11}$ (988 GHz) and $3_{12}$-$2_{21}$ (1157 GHz) data observed for the WILL protostars. The Class 0 objects are indicated in red with an asterisk symbol and the Class I sources in blue with a triangle symbol. The baseline is plotted with a green line and the broad velocity component is shown in pink.

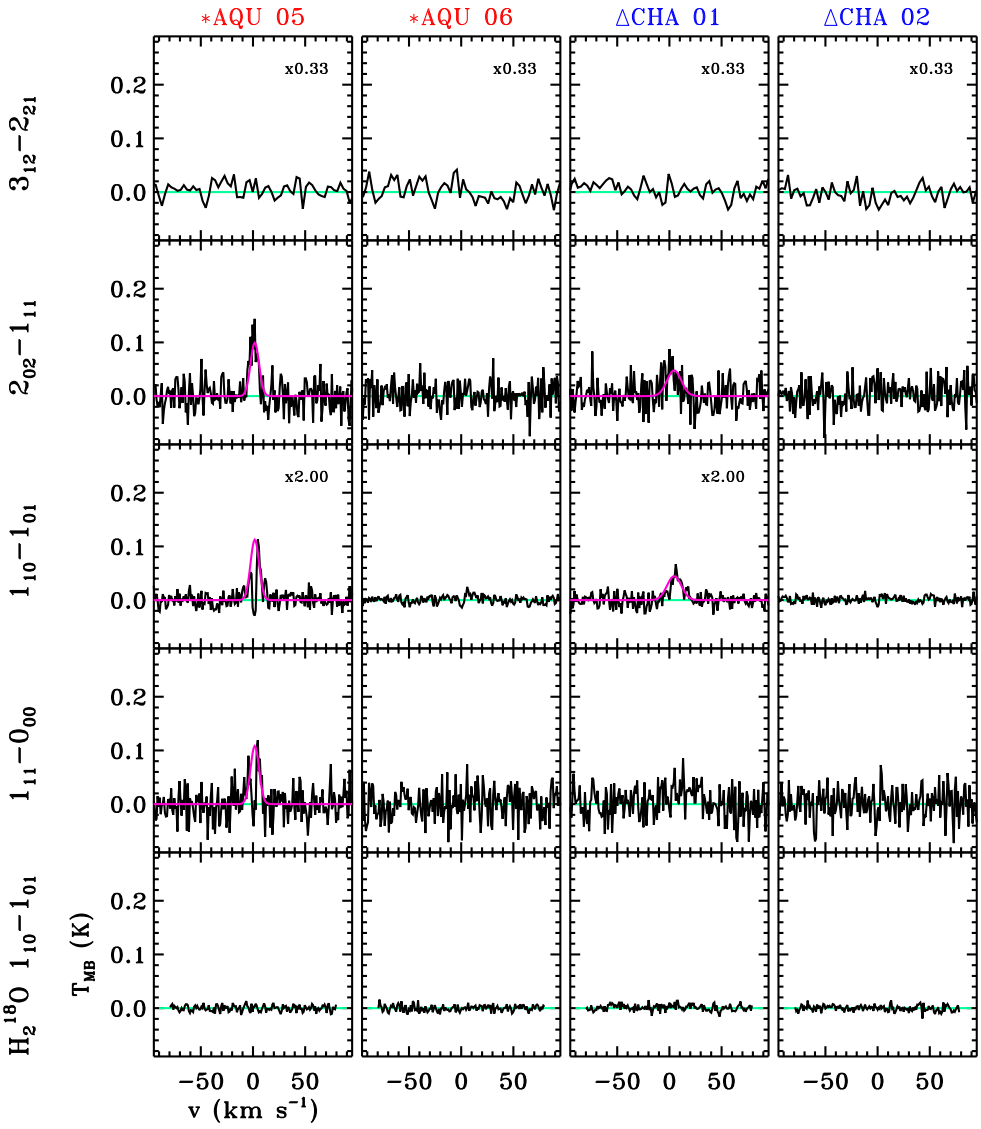


Figure 5.15: Same as Fig. 5.14.

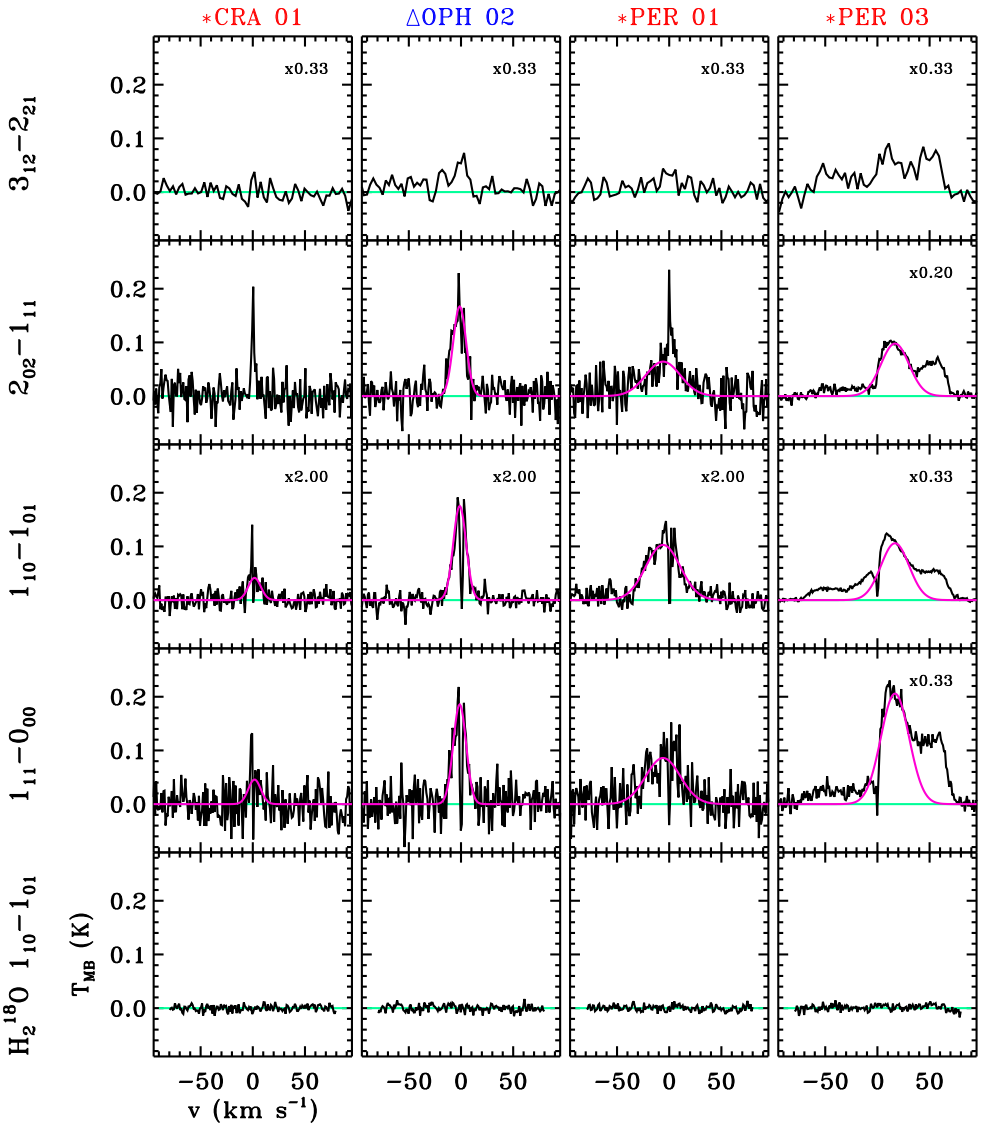


Figure 5.16: Same as Fig. 5.14.

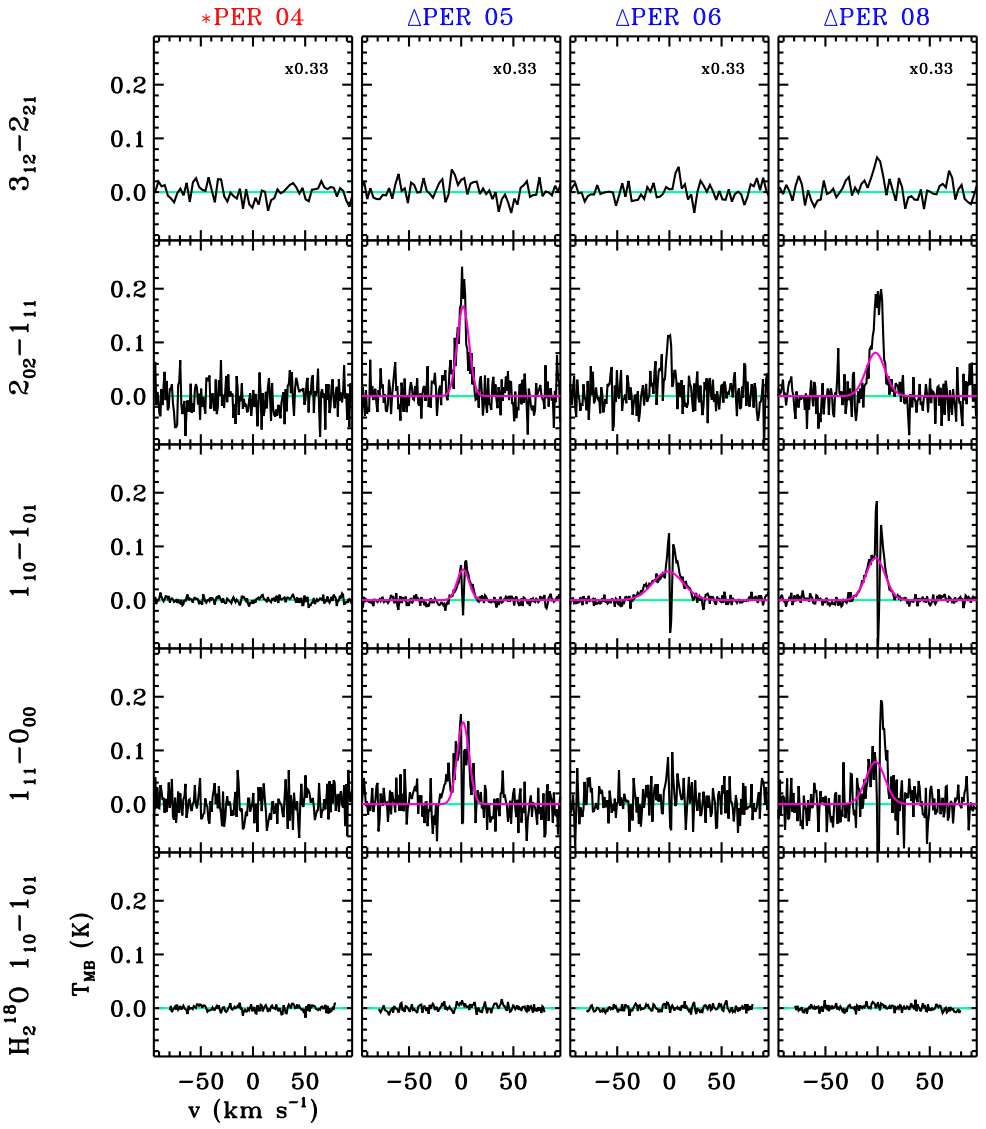


Figure 5.17: Same as Fig. 5.14.

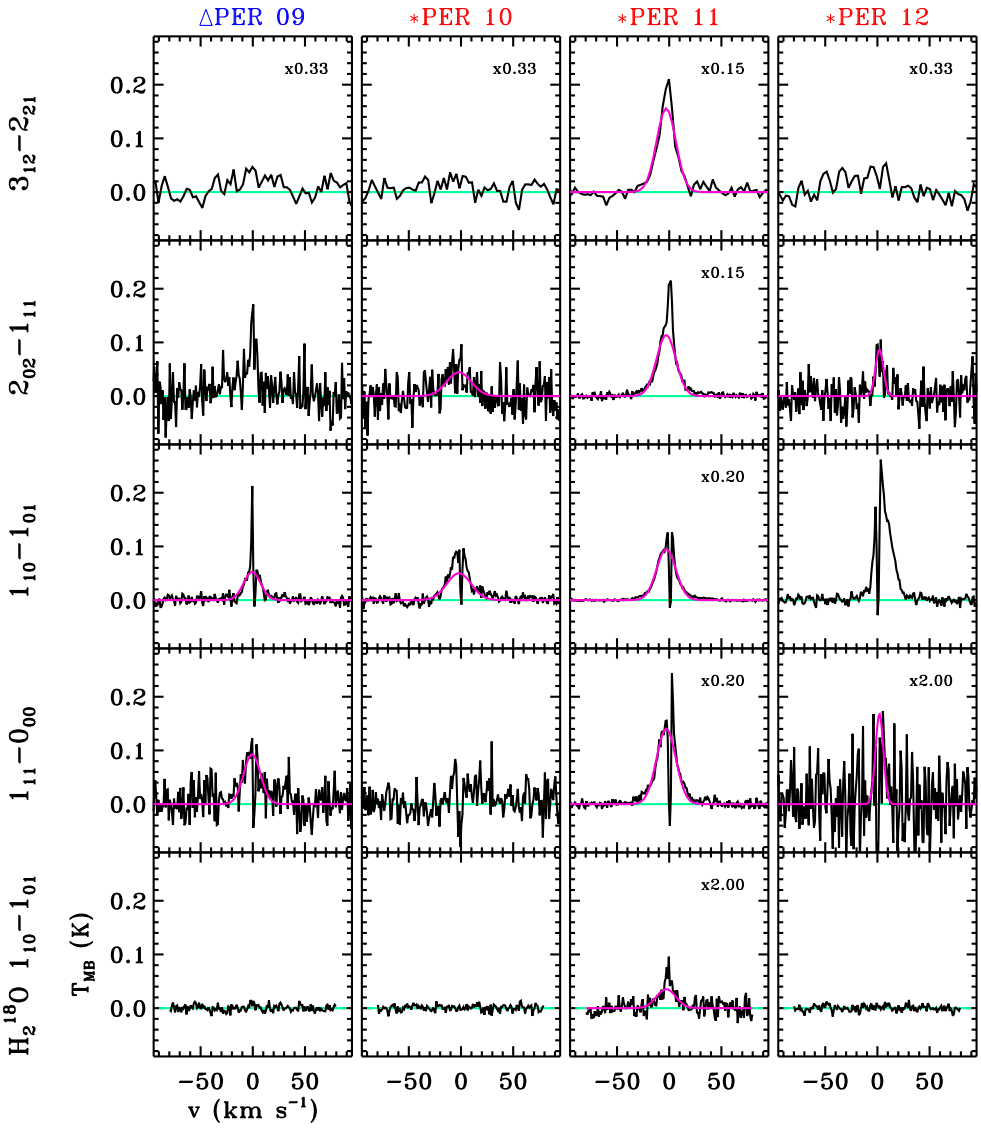


Figure 5.18: Same as Fig. 5.14.

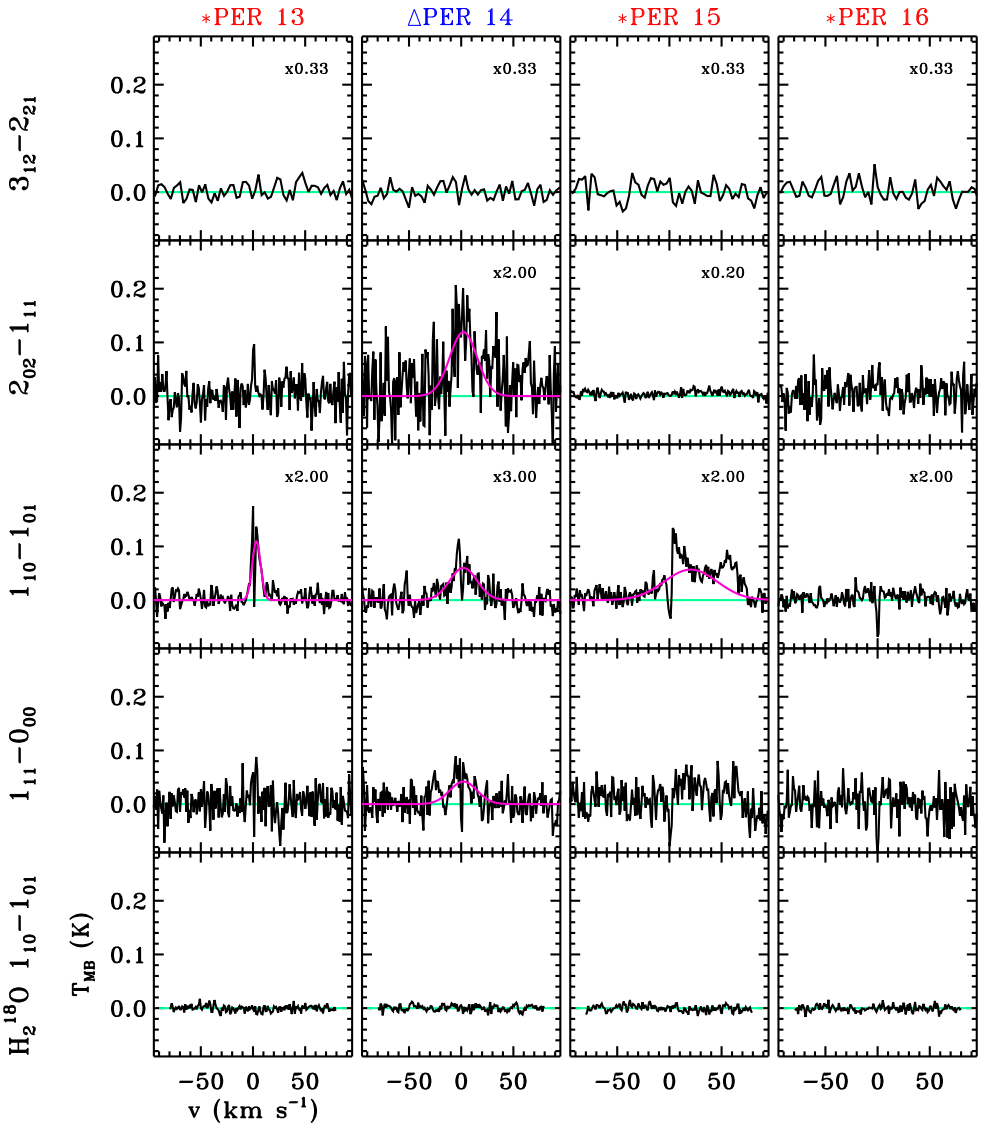


Figure 5.19: Same as Fig. 5.14.

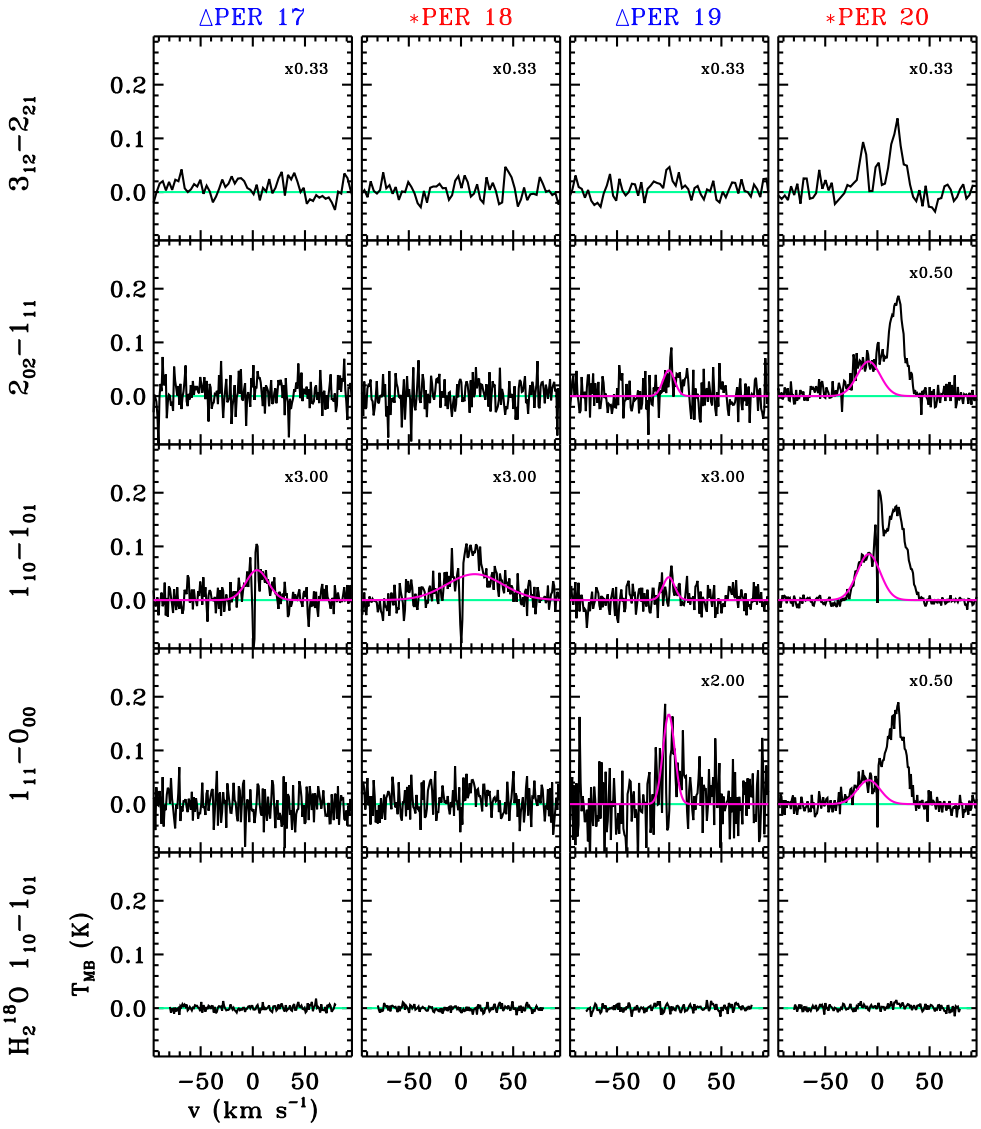


Figure 5.20: Same as Fig. 5.14.

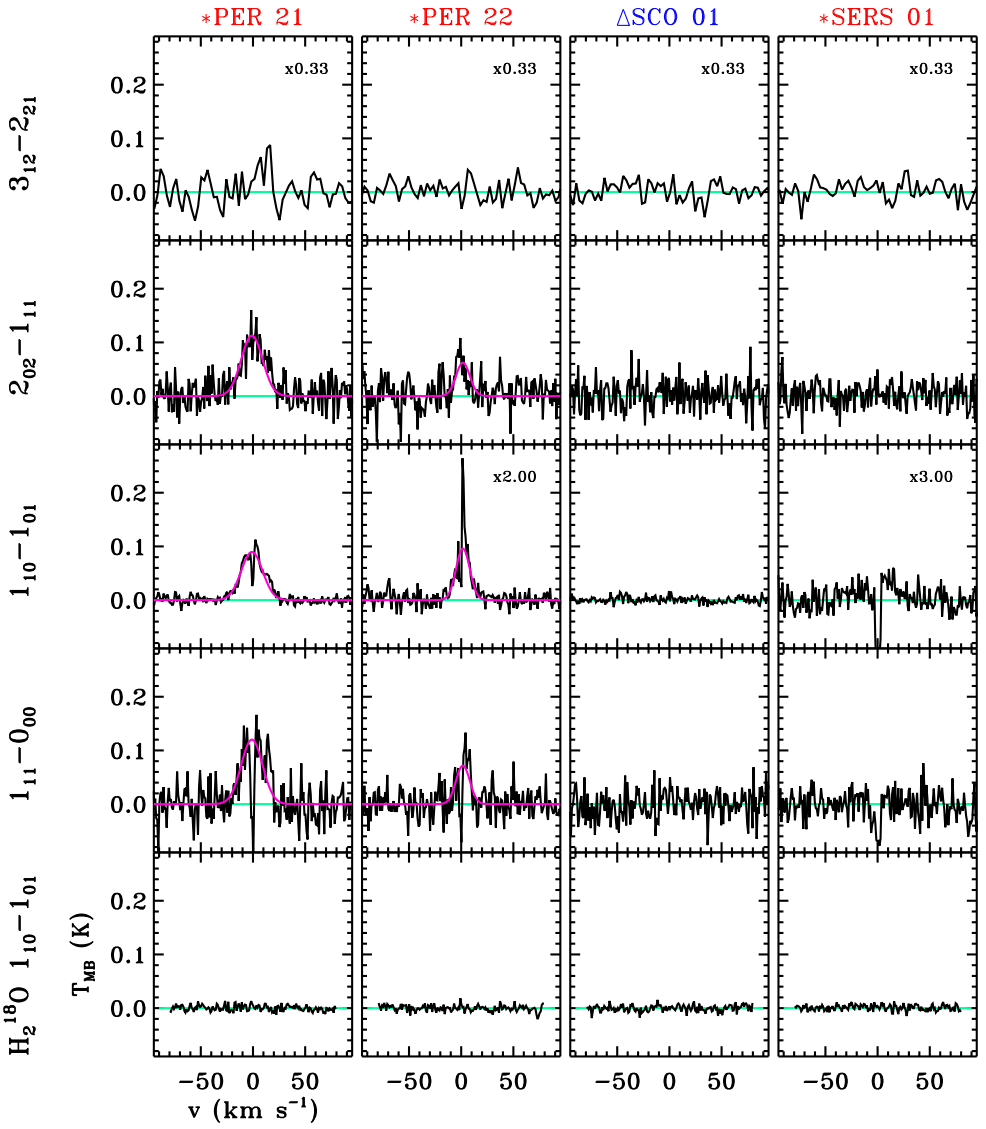


Figure 5.21: Same as Fig. 5.14.

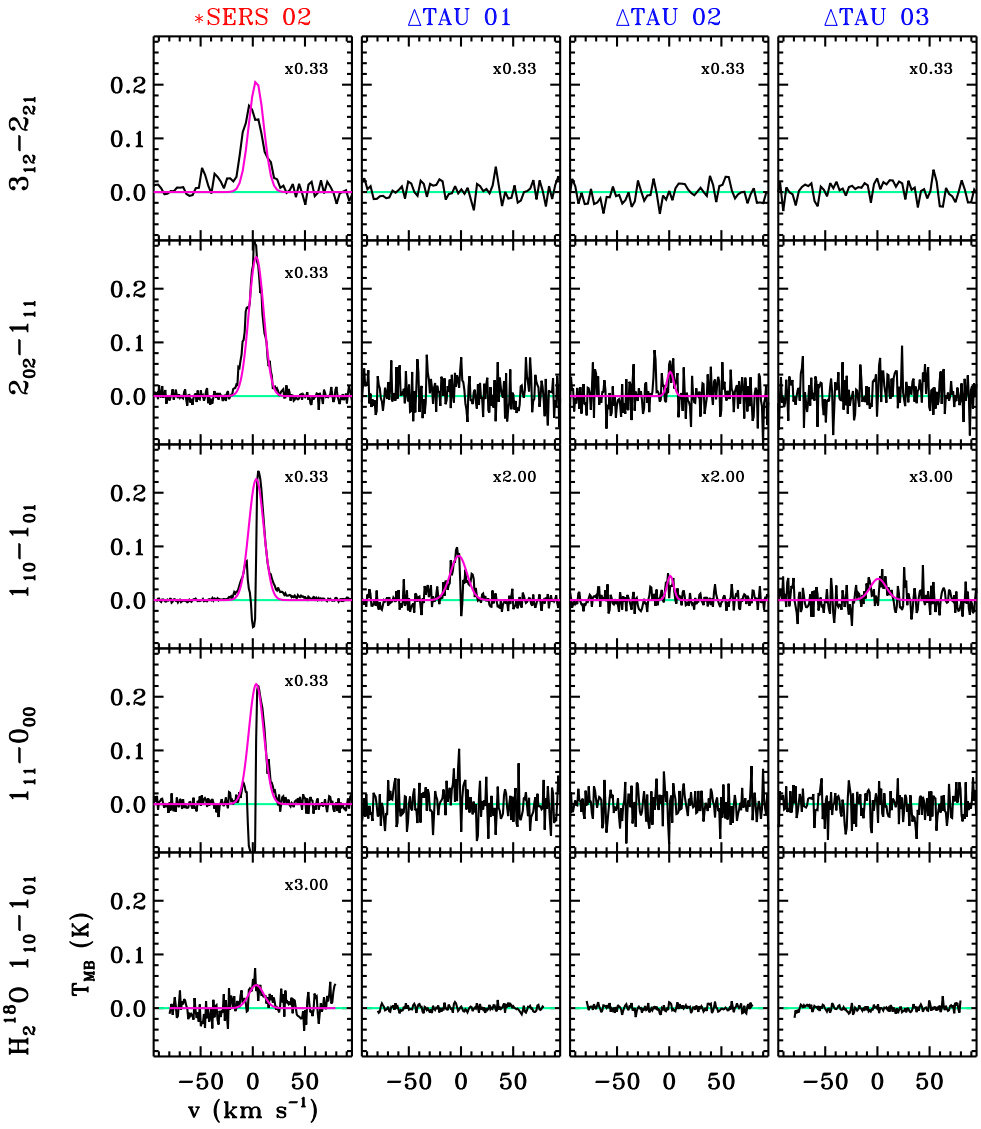


Figure 5.22: Same as Fig. 5.14.

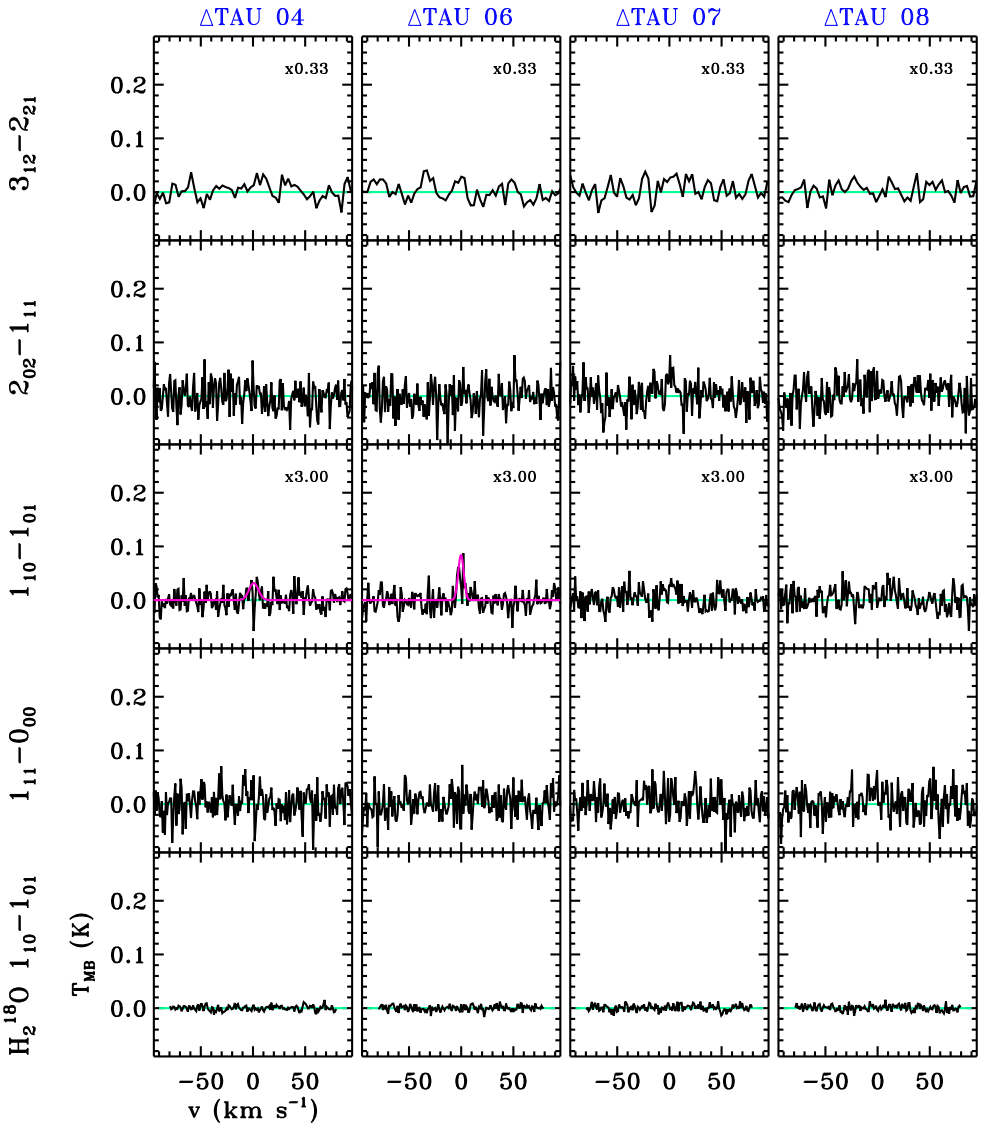


Figure 5.23: Same as Fig. 5.14.

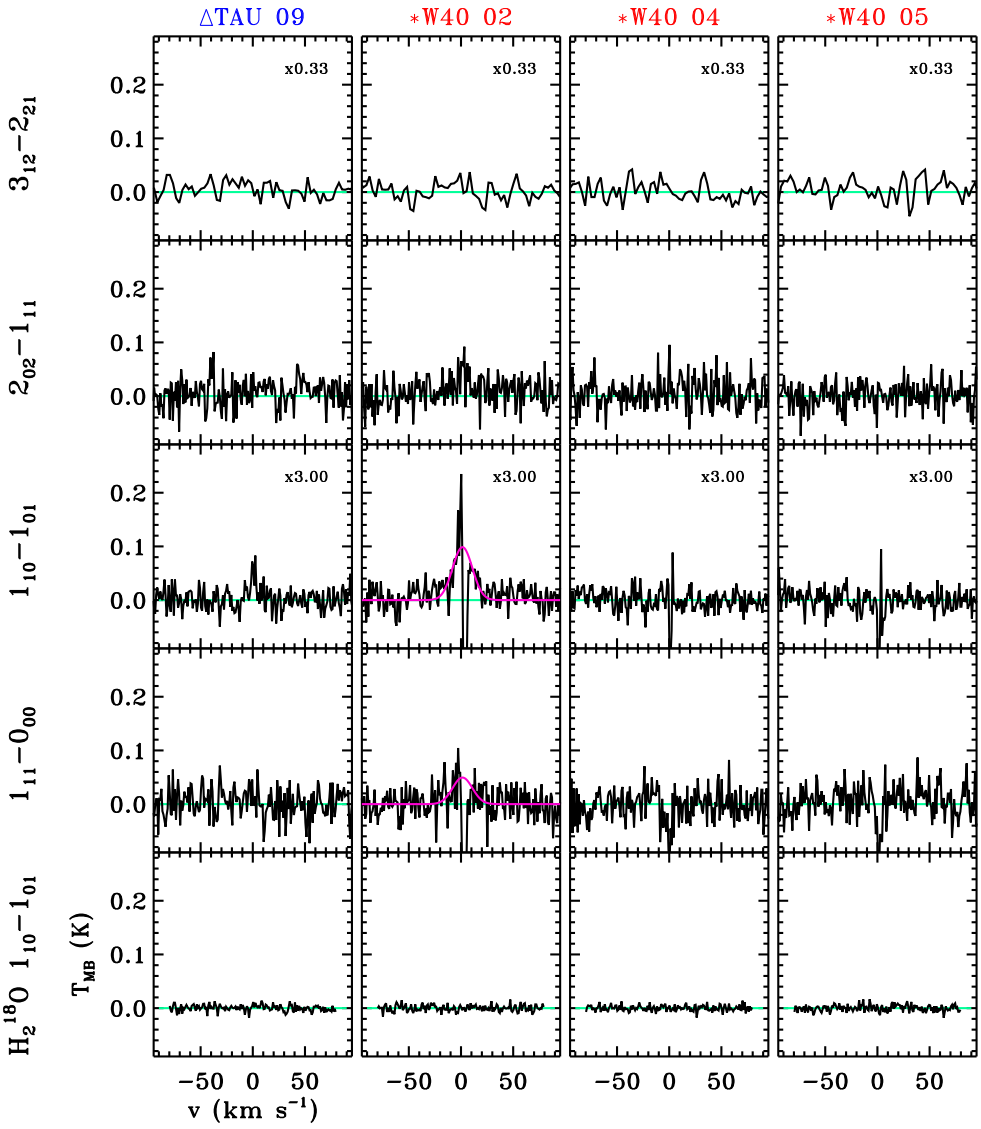


Figure 5.24: Same as Fig. 5.14.

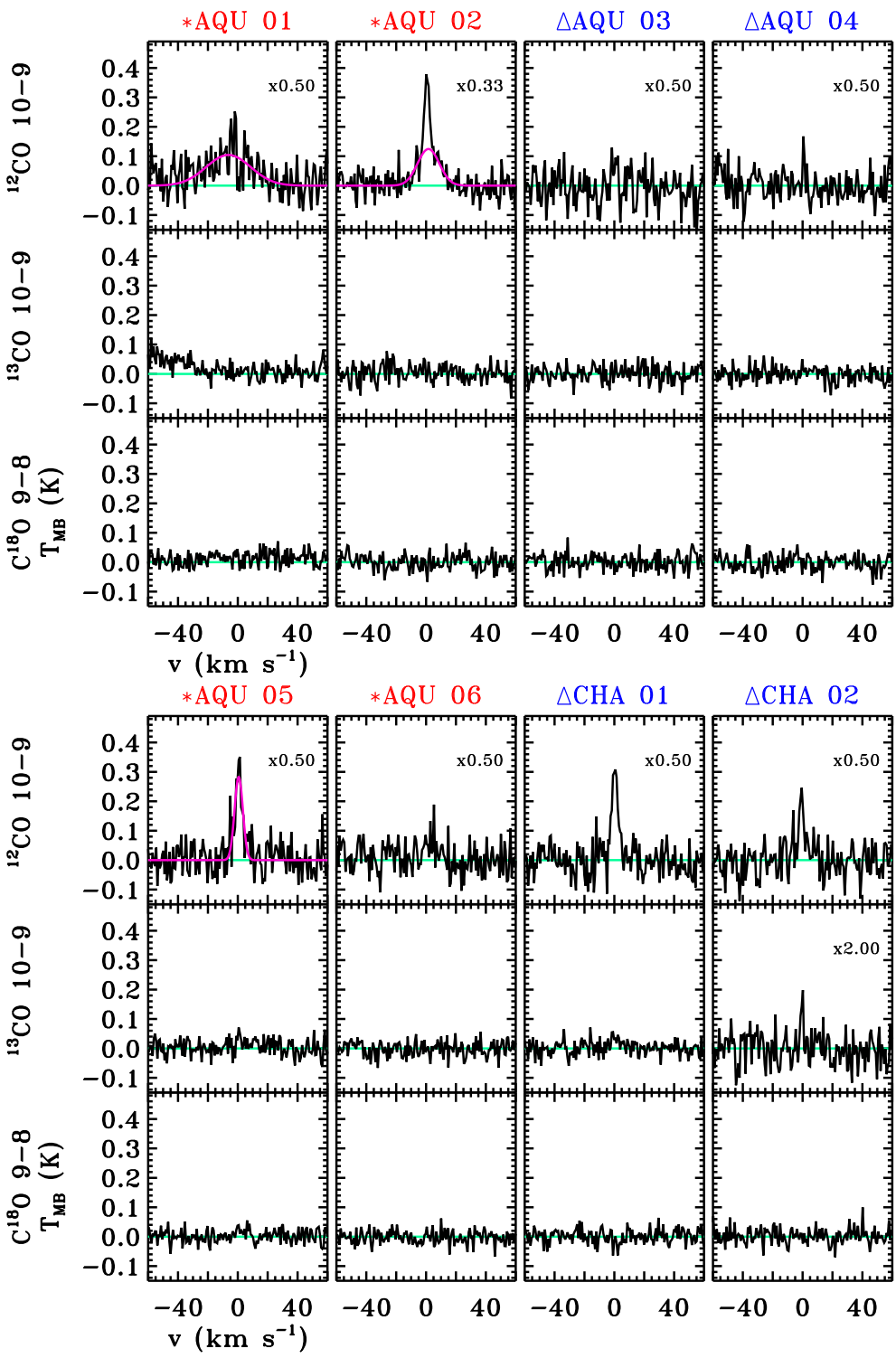


Figure 5.25: $C^{18}O$ $J = 9$–8, $^{13}CO$ $J = 10$–9 and $^{12}CO$ $J = 10$–9 spectra of the WILL protostars. The Class 0 objects are indicated with a red asterisk symbol next to the source name and the Class I with a blue triangle symbol. The baseline is plotted with a green line and the broad velocity component is shown in pink.

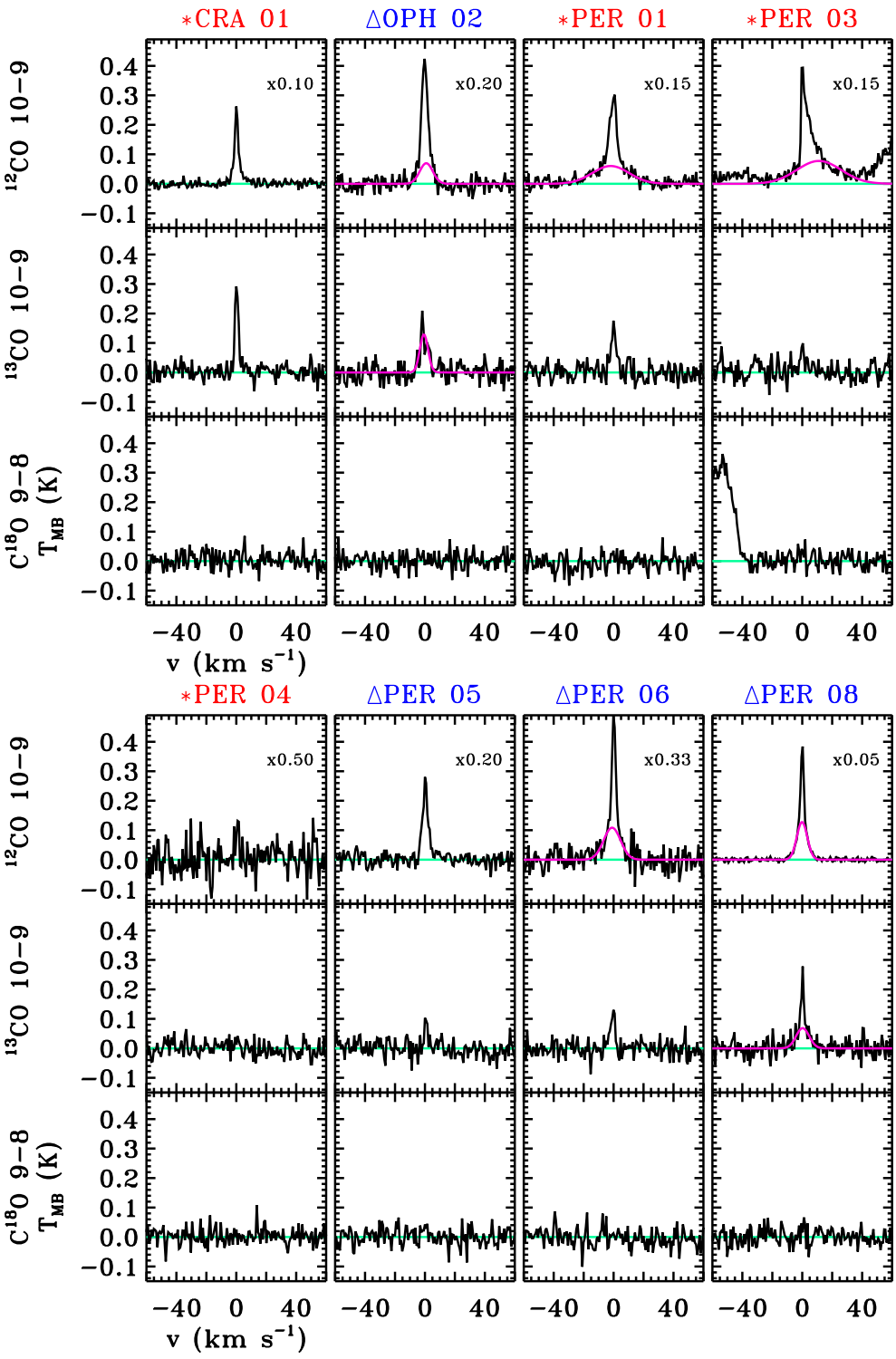


Figure 5.26: Same as Fig. 5.25.

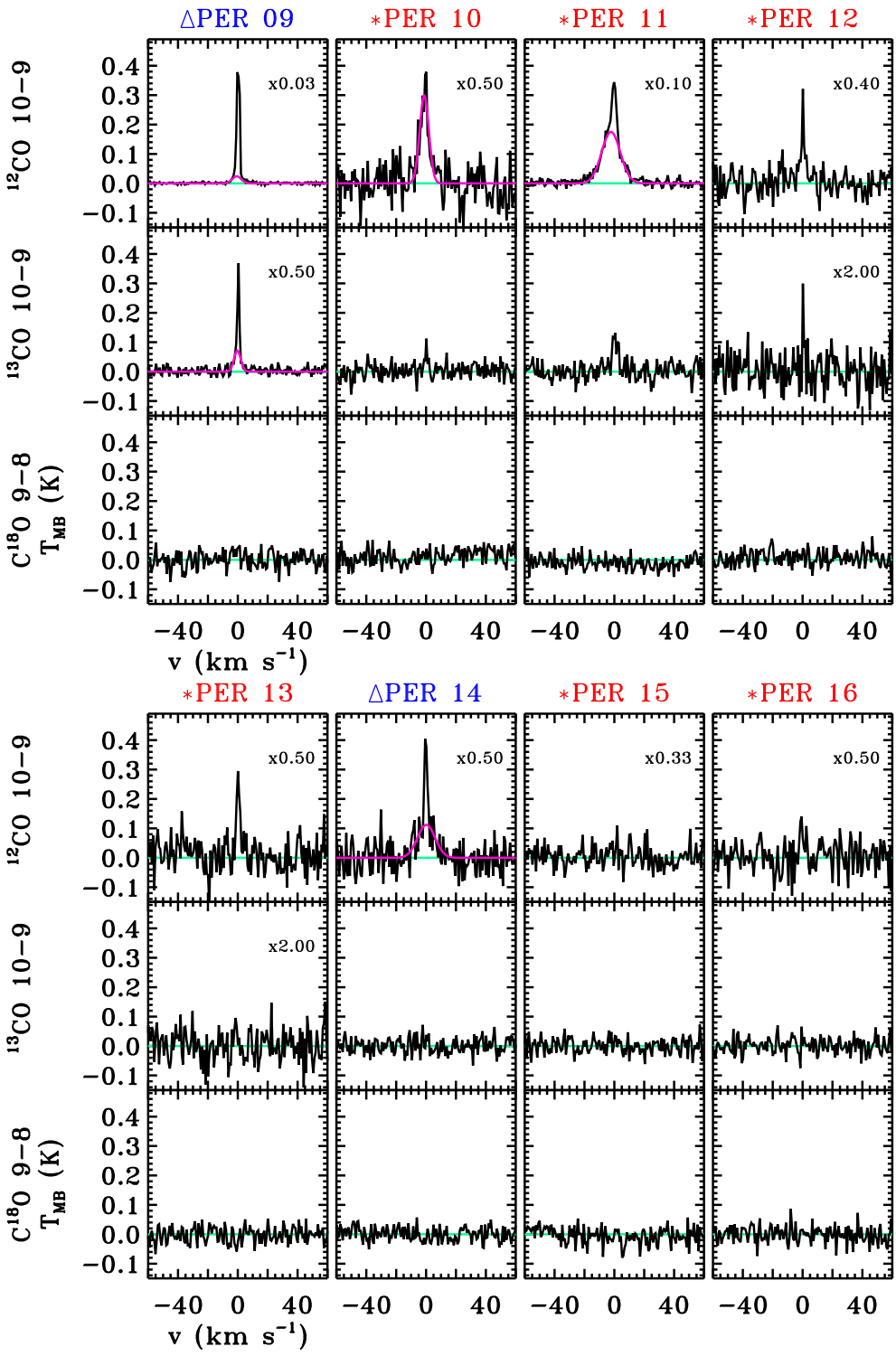


Figure 5.27: Same as Fig. 5.25.

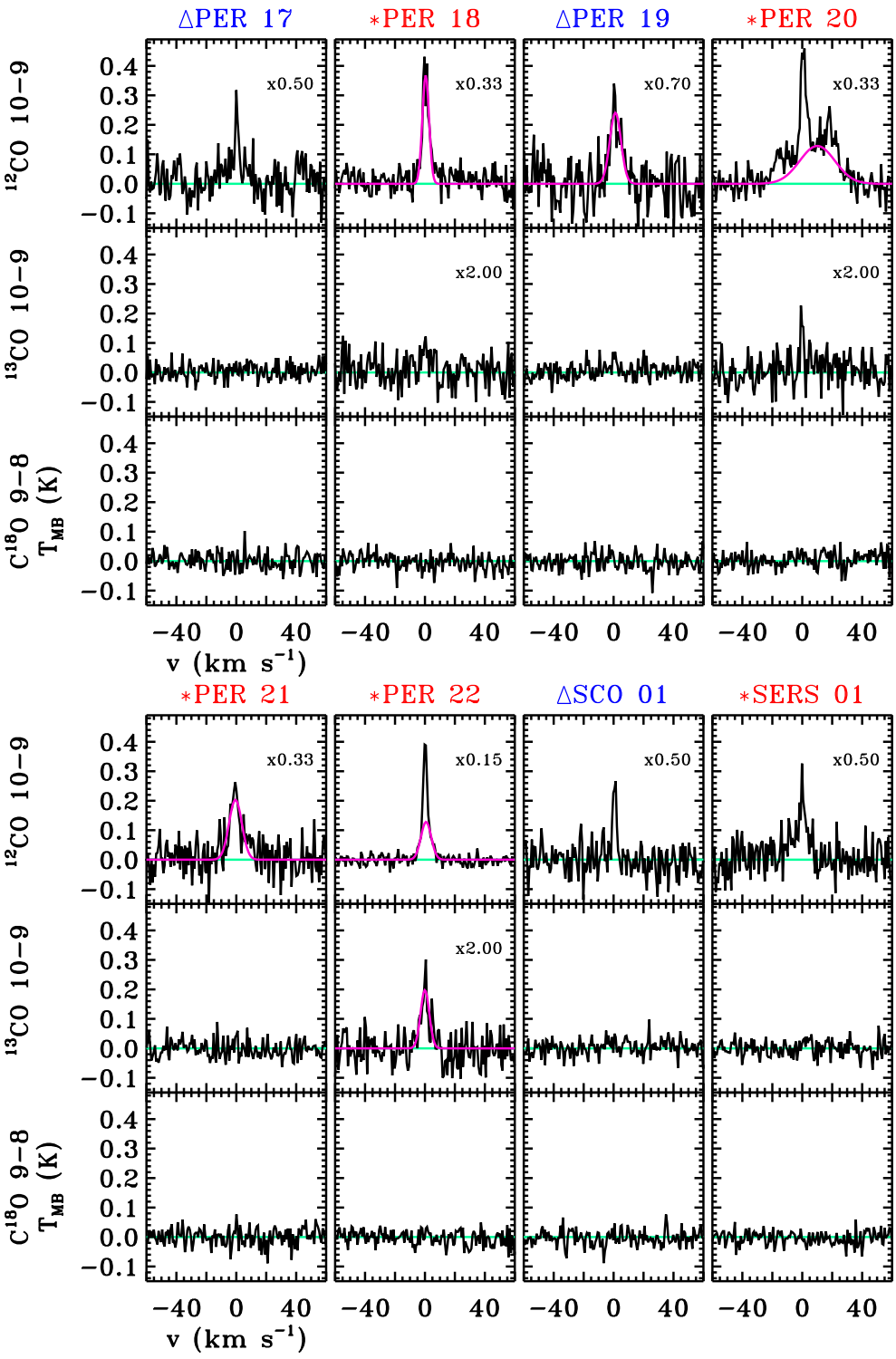


Figure 5.28: Same as Fig. 5.25.

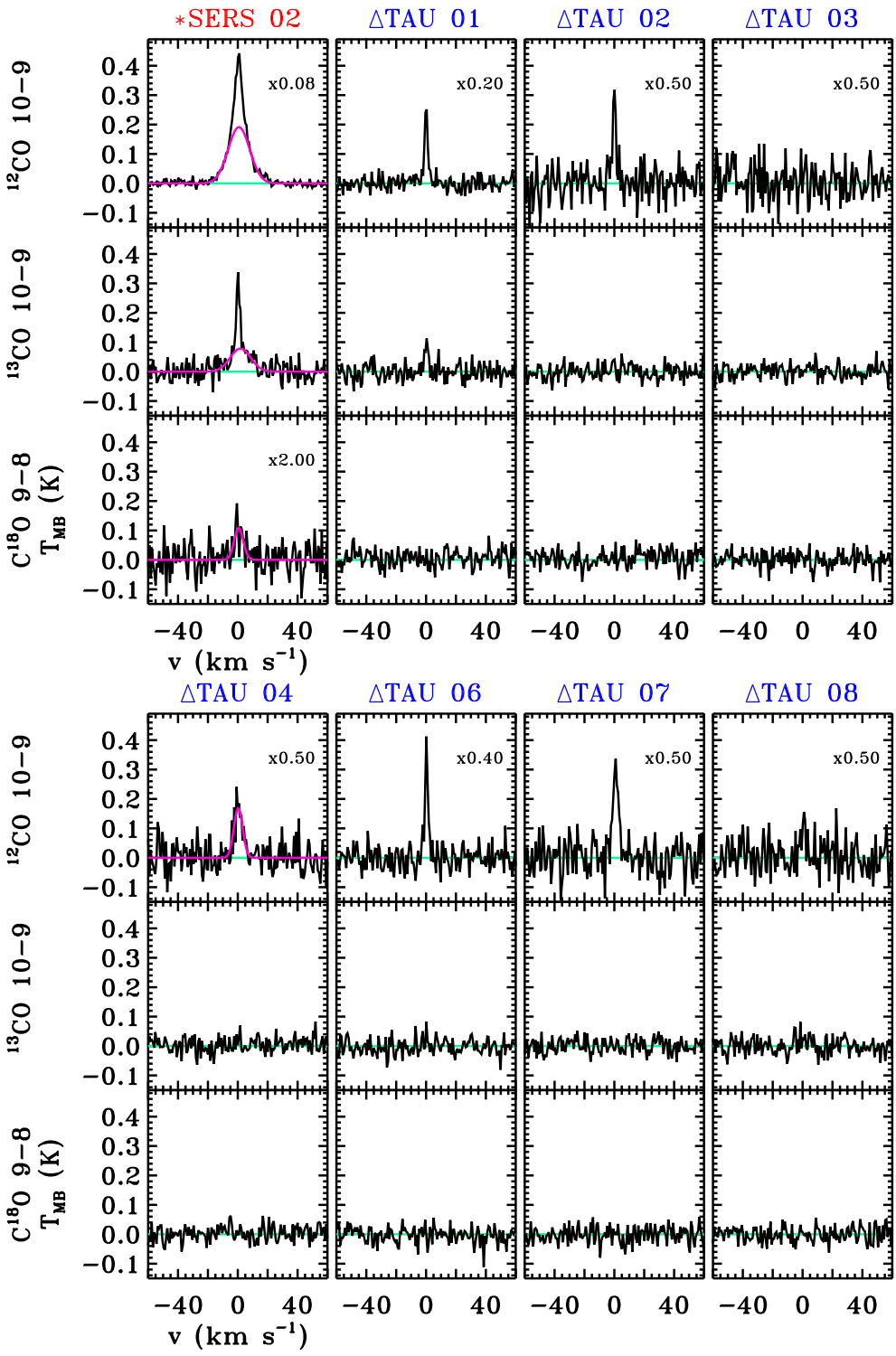


Figure 5.29: Same as Fig. 5.25.

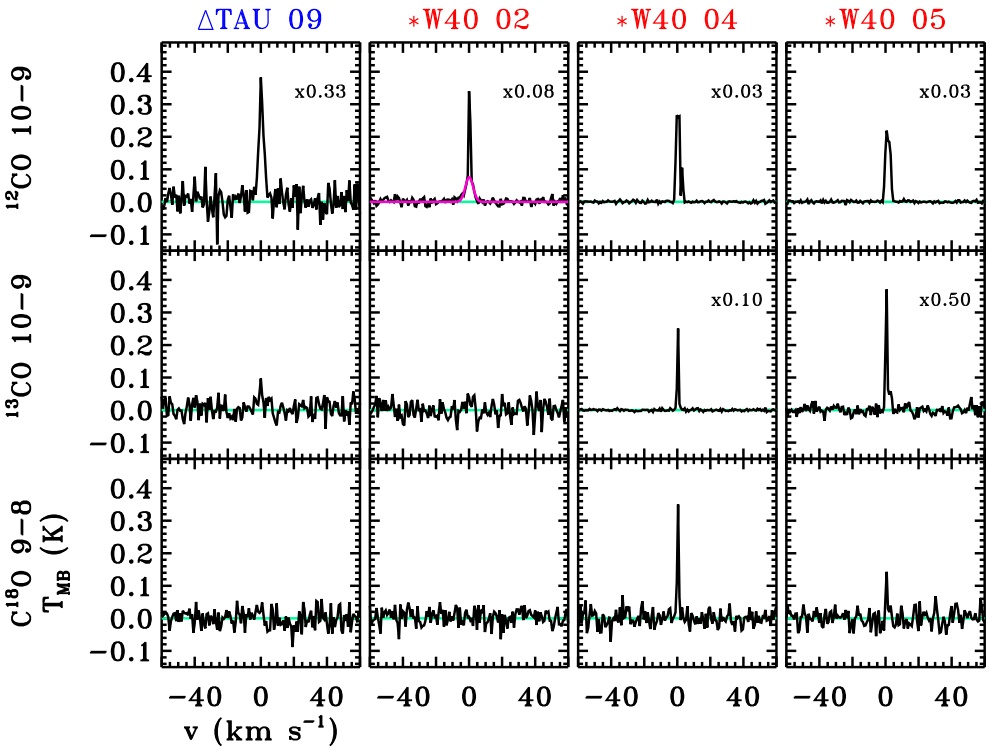


Figure 5.30: Same as Fig. 5.25.

# 5.C. Cygnus data

Table 5.18: Coordenates, distance, source velocity and bolometric luminosity values for the Cygnus YSOs.

| Name | RA | DEC | D | $v_{LSR}$ | $L_{bol}$ | Name | RA | DEC | D | $v_{LSR}$ | $L_{bol}$ |
|---|---|---|---|---|---|---|---|---|---|---|---|
| | (h m s) | (° ′ ″) | (kpc) | (km s$^{-1}$) | ($L_\odot$) | | (h m s) | (° ′ ″) | (kpc) | (km s$^{-1}$) | ($L_\odot$) |
| GR08 01 | 20:24:20.0 | 42:16: 2.0 | 1.4 | – | 398.1 | GR01 31 | 20:39: 3.7 | 42:25:29.0 | 1.4 | -4.7 | 738.0 |
| GR08 02 | 20:24:21.4 | 42:15: 2.0 | 1.4 | – | 7.4 | GR01 32 | 20:39: 4.1 | 42:25:41.0 | 1.4 | -4.5 | 162.9 |
| GR08 03 | 20:24:30.5 | 42: 4: 9.0 | 1.4 | – | 74.3 | GR01 33 | 20:39: 7.3 | 42:15:35.0 | 1.4 | – | 86.9 |
| GR08 04 | 20:24:31.6 | 42: 4:21.0 | 1.4 | 5.4 | 522.4 | GR01 34 | 20:39:16.7 | 42:16: 9.0 | 1.4 | 19.0 | 243.8 |
| GR08 05 | 20:24:33.4 | 42:24:58.0 | 1.4 | – | 110.7 | GR02 01 | 20:36:52.2 | 41:36:24.0 | 1.4 | -2.9 | 6760.0 |
| GR06 02 | 20:29:31.8 | 39: 1:19.0 | 1.4 | -4.5 | 1600.0 | GR02 02 | 20:37: 0.9 | 41:34:55.0 | 1.4 | -1.9 | 1340.0 |
| GR06 03 | 20:29:36.7 | 39: 1:19.0 | 1.4 | -3.2 | 13900.0 | GR02 03 | 20:37: 2.6 | 41:34:41.0 | 1.4 | -0.5 | 52.2 |
| GR06 04 | 20:32:40.8 | 38:47: 6.0 | 1.4 | – | 15.7 | GR02 04 | 20:37:25.5 | 41:33:19.0 | 1.4 | – | 33.9 |
| GR06 05 | 20:32:41.8 | 38:45:56.0 | 1.4 | – | 31.0 | GR02 05 | 20:37:26.0 | 41:35:41.0 | 1.4 | – | 44.9 |
| GR06 06 | 20:32:42.1 | 38:46: 9.0 | 1.4 | – | 85.3 | GR02 06 | 20:39:54.1 | 42: 0:51.0 | 1.4 | – | 106.9 |
| GR03 01 | 20:32:21.1 | 41: 7:54.0 | 1.4 | – | 259.4 | GR02 07 | 20:39:57.8 | 41:59:14.0 | 1.4 | 7.4 | 791.0 |
| GR03 02 | 20:34:43.3 | 40:53:13.0 | 1.4 | 4.8 | 187.5 | GR02 08 | 20:40: 2.2 | 41:28:12.0 | 1.4 | -5.2 | 55.8 |
| GR03 03 | 20:35: 9.3 | 41:38:24.0 | 1.4 | -0.5 | 94.8 | GR02 09 | 20:40: 4.0 | 41:27:34.0 | 1.4 | -5.1 | 94.4 |
| GR03 04 | 20:35:10.1 | 41:13:36.0 | 1.4 | 8.7 | 152.1 | GR02 10 | 20:40: 5.5 | 41:32:13.0 | 1.4 | -4.7 | 450.0 |
| GR03 05 | 20:36: 7.2 | 41:39:55.0 | 1.4 | 11.4 | 6180.0 | GR02 11 | 20:40: 9.2 | 42: 1:18.0 | 1.4 | – | 106.0 |
| GR03 06 | 20:36:20.9 | 40:58:59.0 | 1.4 | – | 79.6 | GR02 12 | 20:40:28.5 | 41:57:12.0 | 1.4 | -6.9 | 140.0 |
| GR01 01 | 20:35: 5.6 | 42:20:16.0 | 1.4 | – | 49.4 | GR02 13 | 20:40:33.5 | 41:59: 0.0 | 1.4 | -6.1 | 150.0 |
| GR01 03 | 20:35:34.4 | 42:20: 7.0 | 1.4 | 14.2 | 227.0 | GR02 14 | 20:40:35.6 | 41:56: 7.0 | 1.4 | -5.2 | 68.5 |
| GR01 05 | 20:36:40.4 | 42:50:32.0 | 1.4 | – | 98.2 | GR02 15 | 20:40:38.4 | 41:53: 2.0 | 1.4 | – | 18.5 |
| GR01 06 | 20:36:56.0 | 42:21:51.0 | 1.4 | – | 61.2 | GR02 16 | 20:41:24.0 | 41:59:48.0 | 1.4 | – | 32.3 |
| GR01 07 | 20:36:57.1 | 42:13:23.0 | 1.4 | 15.4 | 666.0 | GR04 01 | 20:37:14.8 | 39:48:56.0 | 1.4 | 7.4 | 152.8 |
| GR01 08 | 20:36:57.6 | 42:11:30.0 | 1.4 | 15.2 | 1100.0 | GR04 02 | 20:37:42.1 | 39:51: 6.0 | 1.4 | 6.2 | – |
| GR01 09 | 20:37:17.7 | 42:16:37.0 | 1.4 | 17.2 | 290.4 | GR04 03 | 20:41:20.6 | 39:29:32.0 | 1.4 | – | 71.6 |
| GR01 10 | 20:37:23.6 | 42:14:45.0 | 1.4 | – | 8.3 | GR04 04 | 20:41:38.0 | 39:38:21.0 | 1.4 | – | 185.8 |
| GR01 11 | 20:37:27.7 | 42:14:13.0 | 1.4 | – | 78.7 | GR04 05 | 20:41:40.4 | 39:38: 1.0 | 1.4 | – | 218.3 |
| GR01 12 | 20:37:30.5 | 42:13:59.0 | 1.4 | – | 102.1 | GR04 06 | 20:41:50.3 | 39:40:40.0 | 1.4 | – | 148.3 |
| GR01 13 | 20:37:31.9 | 42:13: 2.0 | 1.4 | – | 119.1 | GR05 01 | 20:30:20.9 | 39:49:51.0 | 1.4 | – | 67.6 |
| GR01 14 | 20:37:55.4 | 42:40:47.0 | 1.4 | – | 203.7 | GR05 02 | 20:30:22.7 | 40: 9:23.0 | 1.4 | – | 69.7 |
| GR01 15 | 20:38: 3.9 | 42:39:31.0 | 1.4 | – | 29.8 | GR05 03 | 20:30:41.4 | 39:45:15.0 | 1.4 | – | 188.4 |
| GR01 16 | 20:38: 7.1 | 42:38:52.0 | 1.4 | -2.1 | 80.9 | GR05 04 | 20:31: 8.7 | 40: 3:48.0 | 1.4 | – | 88.1 |
| GR01 17 | 20:38:10.0 | 42:38: 9.0 | 1.4 | – | 37.7 | GR05 05 | 20:31:11.4 | 40: 3: 8.0 | 1.4 | 6.6 | 6800.0 |
| GR01 18 | 20:38:21.1 | 42:11:23.0 | 1.4 | – | 30.8 | GR05 06 | 20:31:37.0 | 40:19:39.0 | 1.4 | – | 7.4 |
| GR01 19 | 20:38:24.7 | 42:31:59.0 | 1.4 | – | 100.9 | GR05 08 | 20:31:58.2 | 40:18:36.0 | 1.4 | – | 11.5 |
| GR01 20 | 20:38:33.3 | 42:39:39.0 | 1.4 | – | 14.8 | GR05 09 | 20:32:22.1 | 40:20:17.0 | 1.4 | -0.2 | 128.5 |
| GR01 22 | 20:38:36.6 | 42:37:32.0 | 1.4 | 9.6 | 22600.0 | GR05 10 | 20:32:28.6 | 40:19:42.0 | 1.4 | – | 100.7 |
| GR01 23 | 20:38:37.3 | 42:39:33.0 | 1.4 | 11.7 | 254.1 | GR05 11 | 20:33:49.1 | 40: 8:41.0 | 1.4 | 7.9 | 4370.0 |
| GR01 24 | 20:38:46.4 | 42:24:40.0 | 1.4 | – | 122.7 | GR05 12 | 20:34:17.6 | 40:18:31.0 | 1.4 | – | 43.0 |
| GR01 25 | 20:38:59.1 | 42:22:26.0 | 1.4 | -2.6 | 300.0 | GR10 01 | 20:20:38.9 | 39:38:18.0 | 1.4 | 2.0 | 127.9 |
| GR01 26 | 20:39: 0.4 | 42:24:37.0 | 1.4 | -3.5 | 1620.0 | GR10 02 | 20:20:39.2 | 39:37:51.0 | 1.4 | 2.4 | 9900.0 |
| GR01 27 | 20:39: 1.3 | 42:22: 5.0 | 1.4 | -3.7 | 950.0 | GR10 03 | 20:20:44.6 | 39:35:21.0 | 1.4 | -1.1 | 32.3 |
| GR01 28 | 20:39: 1.9 | 42:18:37.0 | 1.4 | -3.8 | 130.2 | GR10 04 | 20:21:55.0 | 39:59:45.0 | 1.4 | – | 181.6 |
| GR01 29 | 20:39: 2.1 | 42:24:58.0 | 1.4 | -4.3 | 1803.0 | GR10 05 | 20:22:20.0 | 39:58:23.0 | 1.4 | -1.9 | 23.0 |
| GR01 30 | 20:39: 3.0 | 42:25:51.0 | 1.4 | -4.1 | 630.0 | GR10 06 | 20:22:24.7 | 40: 4:56.0 | 1.4 | – | 52.2 |

**Notes.** The bolometric luminosities, $L_{bol}$, are derived from the work of Kryukova et al. (2014). The source velocities, $v_{LSR}$, are calculated from the $^{13}$CO $J = 10$–9 and C$^{18}$O $J = 9$–8 line fitting for those source detected in either of these lines.

Table 5.19: Observed and fitted properties of the Cygnus $H_2O$ $1_{11}$-$0_{00}$ and $2_{02}$-$1_{11}$ spectra.

| Source | $H_2O$ $1_{11}$-$0_{00}$ | | | | $H_2O$ $2_{02}$-$1_{11}$ | | | |
|---|---|---|---|---|---|---|---|---|
| | rms[a] (mK) | $T_{MB}^{peak}$ (K) | $\int T_{MB} dv$[b] (K km s$^{-1}$) | *FWZI* (km s$^{-1}$) | rms[a] (mK) | $T_{MB}^{peak}$ (K) | $\int T_{MB} dv$[b] (K km s$^{-1}$) | *FWZI* (km s$^{-1}$) |
| GR08 01 | 46 | < 0.03 | – | – | 25 | < 0.01 | – | – |
| GR08 02 | 48 | < 0.03 | – | – | 24 | < 0.01 | – | – |
| GR08 03 | 48 | < 0.03 | – | – | 51 | < 0.03 | – | – |
| GR08 04 | 51 | 0.27 | 6.64 ± 0.06 | 56 | 19 | 0.31 | 4.45 ± 0.05 | 48 |
| GR08 05 | 48 | < 0.03 | – | – | 26 | < 0.01 | – | – |
| GR06 01 | 47 | < 0.03 | – | – | 35 | < 0.02 | – | – |
| GR06 02 | 50 | < 0.03 | – | – | 13 | < 0.01 | – | – |
| GR06 03 | 47 | 0.19 | 0.53 ± 0.05 | 4 | 23 | 0.32 | 0.61 ± 0.04 | 4 |
| GR06 04 | 48 | < 0.03 | – | – | 22 | < 0.01 | – | – |
| GR06 05 | 47 | < 0.03 | – | – | 25 | < 0.01 | – | – |
| GR06 06 | 49 | < 0.03 | – | – | 41 | < 0.02 | – | – |
| GR03 01 | 46 | < 0.03 | – | – | 23 | < 0.01 | – | – |
| GR03 02 | 51 | < 0.03 | – | – | 73 | < 0.04 | – | – |
| GR03 03 | 46 | < 0.03 | – | – | 48 | < 0.02 | – | – |
| GR03 04 | 48 | < 0.03 | – | – | 114 | < 0.06 | – | – |
| GR03 05 | 47 | 0.25 | 0.00 ± 0.07 | 8 | 39 | < 0.02 | – | – |
| GR03 06 | 48 | < 0.03 | – | – | 20 | < 0.01 | – | – |
| GR01 01 | 47 | < 0.03 | – | – | 21 | < 0.01 | – | – |
| GR01 02 | 49 | 0.46 | 1.25 ± 0.06 | 24 | 17 | 0.36 | 4.02 ± 0.05 | 30 |
| GR01 03 | 49 | 0.74 | 5.63 ± 0.06 | 28 | 11 | 0.53 | 8.10 ± 0.06 | 54 |
| GR01 04 | 47 | 0.75 | 6.37 ± 0.06 | 50 | 67 | 0.54 | 9.35 ± 0.07 | 42 |
| GR01 05 | 48 | < 0.03 | – | – | 108 | < 0.06 | – | – |
| GR01 06 | 47 | < 0.03 | – | – | 23 | < 0.01 | – | – |
| GR01 07 | 49 | 0.27 | 2.57 ± 0.06 | 22 | 23 | 0.31 | 2.50 ± 0.06 | 20 |
| GR01 08 | 47 | 0.50 | 10.46 ± 0.07 | 40 | 12 | 0.75 | 14.11 ± 0.05 | 68 |
| GR01 09 | 48 | < 0.03 | – | – | 24 | < 0.01 | – | – |
| GR01 10 | 46 | < 0.03 | – | – | 43 | < 0.02 | – | – |
| GR01 11 | 48 | < 0.03 | – | – | 24 | < 0.01 | – | – |
| GR01 12 | 48 | < 0.03 | – | – | 21 | < 0.01 | – | – |
| GR01 13 | 47 | < 0.03 | – | – | 33 | < 0.02 | – | – |
| GR01 14 | 51 | < 0.03 | – | – | 23 | < 0.01 | – | – |
| GR01 15 | 47 | < 0.03 | – | – | 26 | < 0.01 | – | – |
| GR01 16 | 46 | < 0.03 | – | – | 21 | < 0.01 | – | – |
| GR01 17 | 48 | < 0.03 | – | – | 34 | < 0.02 | – | – |
| GR01 18 | 49 | < 0.03 | – | – | 33 | < 0.02 | – | – |
| GR01 19 | 47 | < 0.03 | – | – | 18 | < 0.01 | – | – |
| GR01 20 | 51 | < 0.03 | – | – | 20 | < 0.01 | – | – |
| GR01 21 | 47 | 0.76 | 6.11 ± 0.05 | 30 | 17 | 1.57 | 22.76 ± 0.05 | 74 |
| GR01 22 | 62 | 3.74 | 21.15 ± 0.06 | 68 | 18 | 9.19 | 112.38 ± 0.05 | 84 |
| GR01 23 | 49 | < 0.03 | – | – | 21 | < 0.01 | – | – |
| GR01 24 | 48 | < 0.03 | – | – | 23 | < 0.01 | – | – |
| GR01 25 | 52 | 0.55 | -3.96 ± 0.05 | 28 | 28 | 0.90 | 10.47 ± 0.06 | 32 |
| GR01 26 | 49 | 0.42 | -1.05 ± 0.06 | 18 | 31 | 0.84 | 5.09 ± 0.04 | 20 |
| GR01 27 | 47 | 0.46 | -6.20 ± 0.06 | 48 | 20 | 1.37 | 16.24 ± 0.05 | 50 |
| GR01 28 | 48 | 0.39 | 2.89 ± 0.05 | 48 | 24 | 0.43 | 9.45 ± 0.06 | 40 |

**Notes.** *FWZI* has been calculated by binning the spectra to 3 km s$^{-1}$. Upper-limits are calculated assuming a *FWHM* of 20 km s$^{-1}$. ([a]) In 0.27 km s$^{-1}$ bin. ([b]) Integrated over the interval of velocities defined by the *FWZI*.

Table 5.20: Observed and fitted properties of the Cygnus $H_2O$ $1_{11}$-$0_{00}$ and $2_{02}$-$1_{11}$ spectra.

| Source | $H_2O$ $1_{11}$-$0_{00}$ | | | | $H_2O$ $2_{02}$-$1_{11}$ | | | |
|---|---|---|---|---|---|---|---|---|
| | rms[a] (mK) | $T_{MB}^{peak}$ (K) | $\int T_{MB} dv$[b] (K km s$^{-1}$) | *FWZI* (km s$^{-1}$) | rms[a] (mK) | $T_{MB}^{peak}$ (K) | $\int T_{MB} dv$[b] (K km s$^{-1}$) | *FWZI* (km s$^{-1}$) |
| GR01 29 | 49 | 0.14 | -9.09 ± 0.05 | 14 | 26 | 0.53 | 5.59 ± 0.05 | 28 |
| GR01 30 | 48 | 0.46 | 0.50 ± 0.06 | 24 | 23 | 0.87 | 19.68 ± 0.04 | 82 |
| GR01 31 | 55 | 0.36 | 0.14 ± 0.05 | 54 | 15 | 0.44 | 8.22 ± 0.04 | 66 |
| GR01 32 | 50 | 0.31 | 3.17 ± 0.06 | 31 | 23 | 0.41 | 7.86 ± 0.06 | 40 |
| GR01 33 | 49 | < 0.03 | – | – | 25 | < 0.01 | – | – |
| GR01 34 | 51 | 0.42 | 5.45 ± 0.05 | 58 | 24 | 0.34 | 5.33 ± 0.05 | 46 |
| GR02 01 | 47 | 0.14 | -5.05 ± 0.06 | 6 | 28 | 0.89 | 6.02 ± 0.07 | 12 |
| GR02 02 | 52 | 0.12 | -1.17 ± 0.06 | 26 | 55 | 0.76 | 6.36 ± 0.06 | 40 |
| GR02 03 | 48 | < 0.03 | – | – | 24 | < 0.01 | – | – |
| GR02 04 | 47 | < 0.03 | – | – | 24 | < 0.01 | – | – |
| GR02 05 | 48 | < 0.03 | – | – | 26 | < 0.01 | – | – |
| GR02 06 | 47 | < 0.03 | – | – | 24 | < 0.01 | – | – |
| GR02 07 | 50 | < 0.03 | – | – | 23 | < 0.01 | – | – |
| GR02 08 | 48 | < 0.03 | – | – | 38 | < 0.02 | – | – |
| GR02 09 | 47 | < 0.03 | – | – | 26 | < 0.02 | – | – |
| GR02 10 | 54 | 0.51 | 6.92 ± 0.05 | 128 | 19 | 0.78 | 12.19 ± 0.05 | 80 |
| GR02 11 | 48 | < 0.03 | – | – | 34 | < 0.02 | – | – |
| GR02 12 | 52 | 0.23 | 2.16 ± 0.05 | 28 | 20 | 0.48 | 5.27 ± 0.05 | 20 |
| GR02 13 | 48 | 0.51 | 6.11 ± 0.06 | 76 | 64 | 0.61 | 7.80 ± 0.06 | 58 |
| GR02 14 | 47 | < 0.03 | – | – | 39 | < 0.02 | – | – |
| GR02 15 | 48 | < 0.03 | – | – | 61 | < 0.04 | – | – |
| GR02 16 | 47 | < 0.03 | – | – | 36 | < 0.02 | – | – |
| GR04 01 | 48 | < 0.03 | – | – | 26 | < 0.02 | – | – |
| GR04 02 | 47 | 0.33 | -0.71 ± 0.05 | 6 | 26 | 0.54 | 3.03 ± 0.05 | 10 |
| GR04 03 | 46 | < 0.03 | – | – | 39 | < 0.02 | – | – |
| GR04 04 | 46 | < 0.03 | – | – | 22 | < 0.01 | – | – |
| GR04 05 | 49 | < 0.03 | – | – | 32 | < 0.02 | – | – |
| GR04 06 | 47 | < 0.03 | – | – | 26 | < 0.02 | – | – |
| GR05 01 | 47 | < 0.03 | – | – | 26 | < 0.01 | – | – |
| GR05 02 | 48 | < 0.03 | – | – | 21 | < 0.01 | – | – |
| GR05 03 | 49 | < 0.03 | – | – | 22 | < 0.01 | – | – |
| GR05 04 | 46 | < 0.03 | – | – | 30 | < 0.02 | – | – |
| GR05 05 | 53 | 0.40 | 0.96 ± 0.05 | 14 | 21 | 0.49 | 2.34 ± 0.05 | 44 |
| GR05 06 | 49 | < 0.03 | – | – | 32 | < 0.02 | – | – |
| GR05 07 | 49 | < 0.03 | – | – | 25 | < 0.01 | – | – |
| GR05 08 | 48 | < 0.03 | – | – | 25 | < 0.01 | – | – |
| GR05 09 | 47 | < 0.03 | – | – | 50 | < 0.03 | – | – |
| GR05 10 | 47 | < 0.03 | – | – | 26 | < 0.02 | – | – |
| GR05 11 | 45 | 0.17 | 0.30 ± 0.05 | 5 | 32 | 0.37 | 1.18 ± 0.06 | 4 |
| GR05 12 | 50 | < 0.03 | – | – | 25 | < 0.01 | – | – |
| GR05 13 | 47 | < 0.03 | – | – | 24 | < 0.01 | – | – |
| GR10 01 | 53 | 0.78 | 7.42 ± 0.06 | 60 | 21 | 0.68 | 11.97 ± 0.05 | 60 |
| GR10 02 | 39 | 0.83 | 0.87 ± 0.07 | 35 | 25 | 1.29 | 8.81 ± 0.05 | 30 |
| GR10 03 | 51 | < 0.03 | – | – | 24 | < 0.01 | – | – |
| GR10 04 | 49 | < 0.03 | – | – | 25 | < 0.02 | – | – |
| GR10 05 | 47 | < 0.03 | – | – | 24 | < 0.01 | – | – |
| GR10 06 | 47 | < 0.03 | – | – | 35 | < 0.02 | – | – |

**Notes.** *FWZI* has been calculated by binning the spectra to 3 km s$^{-1}$. Upper-limits are calculated assuming a *FWHM* of 20 km s$^{-1}$. ([a]) In 0.27 km s$^{-1}$ bin. ([b]) Integrated over the interval of velocities defined by the *FWZI*.

Table 5.21: Observed and fitted properties of the Cygnus $^{13}$CO $J = 10$–9 and C$^{18}$O $J = 9$–8 data.

| Source | $^{13}$CO $J = 10$–9 | | | | C$^{18}$O $J = 9$–8 | | | |
|---|---|---|---|---|---|---|---|---|
| | rms$^a$ (mK) | $T_{\rm MB}^{\rm peak}$ (K) | $\int T_{\rm MB} {\rm d}v^b$ (K km s$^{-1}$) | *FWZI* (km s$^{-1}$) | rms$^a$ (mK) | $T_{\rm MB}^{\rm peak}$ (K) | $\int T_{\rm MB} {\rm d}v^b$ (K km s$^{-1}$) | *FWZI* (km s$^{-1}$) |
| GR08 01 | 38 | < 0.05 | – | – | 44 | < 0.06 | – | – |
| GR08 02 | 33 | < 0.05 | – | – | 48 | < 0.07 | – | – |
| GR08 03 | 55 | < 0.07 | – | – | 51 | < 0.07 | – | – |
| GR08 04 | 53 | 0.39 | 1.95 ± 0.06 | 10 | 59 | < 0.09 | – | – |
| GR08 05 | 50 | < 0.07 | – | – | 57 | < 0.08 | – | – |
| GR06 01 | 53 | < 0.07 | – | – | 59 | < 0.09 | – | – |
| GR06 02 | 51 | 1.08 | 3.23 ± 0.06 | 6 | 55 | < 0.08 | – | – |
| GR06 03 | 46 | 3.94 | 8.40 ± 0.05 | 5 | 51 | 0.50 | 0.83 ± 0.06 | 3 |
| GR06 04 | 46 | < 0.06 | – | – | 51 | < 0.07 | – | – |
| GR06 05 | 45 | < 0.06 | – | – | 49 | < 0.07 | – | – |
| GR06 06 | 50 | < 0.07 | – | – | 64 | < 0.09 | – | – |
| GR03 01 | 54 | < 0.07 | – | – | 56 | < 0.08 | – | – |
| GR03 02 | 51 | 0.26 | 1.06 ± 0.05 | 3 | 47 | < 0.07 | – | – |
| GR03 03 | 39 | 0.27 | 0.24 ± 0.04 | 2 | 52 | < 0.08 | – | – |
| GR03 04 | 41 | 1.82 | 2.37 ± 0.05 | 4 | 57 | < 0.08 | – | – |
| GR03 05 | 54 | 2.10 | 4.09 ± 0.06 | 3 | 55 | < 0.08 | – | – |
| GR03 06 | 51 | < 0.07 | – | – | 58 | < 0.08 | – | – |
| GR01 01 | 52 | < 0.07 | – | – | 63 | < 0.09 | – | – |
| GR01 02 | 54 | 0.40 | 1.93 ± 0.06 | 8 | 57 | < 0.08 | – | – |
| GR01 03 | 55 | 0.38 | 1.13 ± 0.06 | 7 | 54 | < 0.08 | – | – |
| GR01 04 | 52 | 0.37 | 0.50 ± 0.06 | 5 | 51 | < 0.07 | – | – |
| GR01 05 | 54 | < 0.07 | – | – | 47 | < 0.07 | – | – |
| GR01 06 | 42 | < 0.06 | – | – | 41 | < 0.06 | – | – |
| GR01 07 | 47 | < 0.07 | – | – | 44 | < 0.06 | – | – |
| GR01 08 | 59 | 0.34 | 1.54 ± 0.06 | 7 | 45 | < 0.06 | – | – |
| GR01 09 | 48 | 0.77 | 1.18 ± 0.06 | 2 | 67 | < 0.10 | – | – |
| GR01 10 | 45 | < 0.06 | – | – | 54 | < 0.08 | – | – |
| GR01 11 | 41 | < 0.06 | – | – | 66 | < 0.09 | – | – |
| GR01 12 | 49 | < 0.07 | – | – | 63 | < 0.09 | – | – |
| GR01 13 | 46 | < 0.07 | – | – | 49 | < 0.07 | – | – |
| GR01 14 | 49 | < 0.07 | – | – | 53 | < 0.07 | – | – |
| GR01 15 | 44 | < 0.06 | – | – | 55 | < 0.08 | – | – |
| GR01 16 | 48 | 0.59 | 0.57 ± 0.05 | 2 | 48 | < 0.07 | – | – |
| GR01 17 | 46 | < 0.07 | – | – | 58 | < 0.08 | – | – |
| GR01 18 | 54 | < 0.08 | – | – | 50 | < 0.07 | – | – |
| GR01 19 | 50 | < 0.07 | – | – | 47 | < 0.07 | – | – |
| GR01 20 | 44 | < 0.07 | – | – | 44 | < 0.06 | – | – |
| GR01 21 | 56 | 1.29 | 7.12 ± 0.06 | 12 | 49 | 0.27 | 5.27 ± 0.05 | 8 |
| GR01 22 | 60 | 9.15 | 62.43 ± 0.07 | 31 | 43 | 2.49 | 9.45 ± 0.05 | 14 |
| GR01 23 | 52 | 0.68 | 0.12 ± 0.06 | 2 | 55 | < 0.08 | – | – |
| GR01 24 | 49 | < 0.07 | – | – | 54 | < 0.08 | – | – |
| GR01 25 | 47 | 0.42 | 0.81 ± 0.05 | 10 | 44 | 0.18 | 0.54 ± 0.05 | 6 |
| GR01 26 | 44 | 1.27 | 5.27 ± 0.05 | 10 | 51 | 0.25 | 0.05 ± 0.05 | 3 |
| GR01 27 | 50 | 2.39 | 6.21 ± 0.05 | 9 | 51 | 0.39 | 0.12 ± 0.06 | 2 |
| GR01 28 | 52 | 0.19 | 4.79 ± 0.06 | 11 | 47 | < 0.07 | – | – |

**Notes.** *FWZI* has been calculated by binning the spectra to 3 km s$^{-1}$. Upper-limits are calculated assuming a *FWHM* of 3 km s$^{-1}$. $(^a)$ In 0.27 km s$^{-1}$ bin. $(^b)$ Integrated over the interval of velocities defined by the *FWZI*.

Table 5.22: Observed and fitted properties of the Cygnus $^{13}$CO $J = 10$–9 and C$^{18}$O $J = 9$–8 data.

| Source | $^{13}$CO $J = 10$–9 | | | | C$^{18}$O $J = 9$–8 | | | |
|---|---|---|---|---|---|---|---|---|
| | rms[a] (mK) | $T_{\rm MB}^{\rm peak}$ (K) | $\int T_{\rm MB} {\rm d}v$[b] (K km s$^{-1}$) | *FWZI* (km s$^{-1}$) | rms[a] (mK) | $T_{\rm MB}^{\rm peak}$ (K) | $\int T_{\rm MB} {\rm d}v$[b] (K km s$^{-1}$) | *FWZI* (km s$^{-1}$) |
| GR01 29 | 56 | 0.77 | 4.28 ± 0.06 | 7 | 49 | 0.25 | 0.39 ± 0.05 | 3 |
| GR01 30 | 60 | 0.36 | 3.96 ± 0.06 | 11 | 49 | < 0.07 | – | – |
| GR01 31 | 52 | 0.93 | 2.71 ± 0.06 | 4 | 60 | < 0.08 | – | – |
| GR01 32 | 48 | 0.27 | 2.17 ± 0.05 | 5 | 49 | < 0.07 | – | – |
| GR01 33 | 51 | < 0.07 | – | – | 55 | < 0.08 | – | – |
| GR01 34 | 60 | 0.19 | 0.77 ± 0.07 | 7 | 44 | < 0.06 | – | – |
| GR02 01 | 55 | 2.49 | 10.09 ± 0.06 | 9 | 47 | 0.45 | 1.67 ± 0.05 | 6 |
| GR02 02 | 57 | 1.01 | 3.09 ± 0.06 | 8 | 51 | 0.24 | 2.18 ± 0.06 | 1 |
| GR02 03 | 50 | 0.45 | 0.74 ± 0.05 | 1 | 53 | < 0.07 | – | – |
| GR02 04 | 48 | < 0.07 | – | – | 47 | < 0.07 | – | – |
| GR02 05 | 46 | < 0.07 | – | – | 48 | < 0.07 | – | – |
| GR02 06 | 46 | < 0.07 | – | – | 59 | < 0.08 | – | – |
| GR02 07 | 52 | 0.15 | 0.31 ± 0.06 | 4 | 49 | < 0.07 | – | – |
| GR02 08 | 47 | 0.76 | 1.16 ± 0.05 | 2 | 53 | < 0.07 | – | – |
| GR02 09 | 52 | 0.20 | 0.35 ± 0.06 | 2 | 50 | < 0.07 | – | – |
| GR02 10 | 60 | 0.29 | 0.32 ± 0.07 | 7 | 46 | < 0.06 | – | – |
| GR02 11 | 49 | < 0.07 | – | – | 52 | < 0.07 | – | – |
| GR02 12 | 50 | 0.31 | 1.90 ± 0.06 | 8 | 51 | < 0.07 | – | – |
| GR02 13 | 54 | 0.19 | 1.08 ± 0.06 | 5 | 57 | < 0.08 | – | – |
| GR02 14 | 50 | 0.25 | 0.05 ± 0.06 | 1 | 52 | < 0.07 | – | – |
| GR02 15 | 46 | < 0.07 | – | – | 47 | < 0.07 | – | – |
| GR02 16 | 46 | < 0.07 | – | – | 49 | < 0.07 | – | – |
| GR04 01 | 49 | 1.44 | 2.23 ± 0.05 | 3 | 51 | < 0.07 | – | – |
| GR04 02 | 50 | 0.45 | 1.97 ± 0.06 | 9 | 56 | < 0.08 | – | – |
| GR04 03 | 52 | < 0.07 | – | – | 54 | < 0.08 | – | – |
| GR04 04 | 44 | < 0.06 | – | – | 54 | < 0.08 | – | – |
| GR04 05 | 50 | < 0.07 | – | – | 49 | < 0.07 | – | – |
| GR04 06 | 41 | < 0.06 | – | – | 53 | < 0.07 | – | – |
| GR05 01 | 49 | < 0.07 | – | – | 53 | < 0.07 | – | – |
| GR05 02 | 48 | < 0.07 | – | – | 50 | < 0.07 | – | – |
| GR05 03 | 45 | < 0.07 | – | – | 54 | < 0.08 | – | – |
| GR05 04 | 54 | < 0.08 | – | – | 40 | < 0.06 | – | – |
| GR05 05 | 60 | 3.88 | 8.99 ± 0.07 | 8 | 45 | 0.39 | 2.12 ± 0.05 | 4 |
| GR05 06 | 44 | < 0.06 | – | – | 51 | < 0.07 | – | – |
| GR05 07 | 46 | < 0.07 | – | – | 51 | < 0.07 | – | – |
| GR05 08 | 55 | < 0.08 | – | – | 47 | < 0.07 | – | – |
| GR05 09 | 38 | 0.20 | 0.40 ± 0.04 | 3 | 45 | < 0.06 | – | – |
| GR05 10 | 43 | < 0.06 | – | – | 51 | < 0.07 | – | – |
| GR05 11 | 65 | 3.03 | 7.12 ± 0.07 | 7 | 42 | 0.27 | 1.27 ± 0.05 | 3 |
| GR05 12 | 49 | < 0.07 | – | – | 49 | < 0.07 | – | – |
| GR05 13 | 52 | < 0.07 | – | – | 54 | < 0.08 | – | – |
| GR10 01 | 51 | 0.24 | 3.18 ± 0.06 | 9 | 49 | < 0.07 | – | – |
| GR10 02 | 44 | 2.93 | 12.84 ± 0.05 | 14 | 55 | 0.45 | 1.55 ± 0.06 | 6 |
| GR10 03 | 47 | 0.15 | 0.85 ± 0.05 | 4 | 52 | < 0.07 | – | – |
| GR10 04 | 51 | < 0.07 | – | – | 49 | < 0.07 | – | – |
| GR10 05 | 49 | 0.57 | 0.96 ± 0.06 | 1 | 41 | < 0.06 | – | – |
| GR10 06 | 49 | < 0.07 | – | – | 51 | < 0.07 | – | – |

**Notes.** *FWZI* has been calculated by binning the spectra to 3 km s$^{-1}$. Upper-limits are calculated assuming a *FWHM* of 3 km s$^{-1}$. ([a]) In 0.27 km s$^{-1}$ bin. ([b]) Integrated over the interval of velocities defined by the *FWZI*.

Table 5.23: Gaussian decomposition results for the Cygnus water data.

| Source | Comp.[a] | $FWHM$ | $v_{\rm peak}$ | $v_{\rm LSR}$ | $H_2O$ $1_{11}$-$0_{00}$ | | $H_2O$ $2_{02}$-$1_{11}$ | |
|---|---|---|---|---|---|---|---|---|
| | | | | | $T_{\rm MB}^{\rm peak}$ | $\int T_{\rm MB} {\rm d}v^b$ | $T_{\rm MB}^{\rm peak}$ | $\int T_{\rm MB} {\rm d}v^b$ |
| | | (km s$^{-1}$) | (km s$^{-1}$) | (km s$^{-1}$) | (K) | (K km s$^{-1}$) | (K) | (K km s$^{-1}$) |
| GR08 04 | C | 38.6 ± 3.6 | 5.9 ± 1.5 | 5.4 | 0.13 ± 0.03 | 5.19 ± 1.21 | 0.13 ± 0.01 | 5.37 ± 0.68 |
| GR06 03 | E | 2.0 ± 1.5 | -3.3 ± 0.7 | -3.2 | 0.11 ± 0.34 | 0.25 ± 0.76 | 0.31 ± 0.21 | 0.68 ± 0.68 |
| GR01 02 | E | 5.0 ± 1.0 | 16.1 ± 0.4 | 14.9 | 0.30 ± 0.09 | 1.60 ± 0.58 | 0.19 ± 0.03 | 1.01 ± 0.26 |
| | C | 30.8 ± 3.5 | 18.7 ± 1.3 | 14.9 | 0.10 ± 0.04 | 1.60 ± 0.58 | 0.13 ± 0.02 | 1.01 ± 0.26 |
| GR01 03 | E | 5.1 ± 1.1 | 15.8 ± 0.4 | 14.2 | 0.48 ± 0.26 | 2.60 ± 1.51 | 0.29 ± 0.05 | 1.56 ± 0.44 |
| | C | 30.3 ± 3.7 | 15.1 ± 1.3 | 14.2 | 0.19 ± 0.11 | 2.60 ± 1.51 | 0.21 ± 0.03 | 1.56 ± 0.44 |
| GR01 04 | E | 6.2 ± 0.6 | 15.7 ± 0.2 | 14.8 | 0.45 ± 0.04 | 2.95 ± 0.36 | 0.28 ± 0.03 | 1.82 ± 0.28 |
| | C | 30.2 ± 1.8 | 16.0 ± 0.6 | 14.8 | 0.24 ± 0.02 | 2.95 ± 0.36 | 0.19 ± 0.02 | 1.82 ± 0.28 |
| GR01 07 | C | 13.5 ± 1.2 | 15.7 ± 0.5 | -4.5 | 0.16 ± 0.03 | 2.34 ± 0.47 | 0.19 ± 0.02 | 2.67 ± 0.33 |
| GR01 08 | E | 4.1 ± 0.4 | 16.9 ± 0.2 | 15.2 | 0.32 ± 0.32 | 1.39 ± 1.41 | 0.44 ± 0.04 | 1.88 ± 0.25 |
| | C | 36.6 ± 1.8 | 11.9 ± 0.7 | 15.2 | 0.19 ± 0.05 | 1.39 ± 1.41 | 0.29 ± 0.01 | 1.88 ± 0.25 |
| GR01 21 | E | 7.8 ± 0.4 | 11.1 ± 0.1 | 9.0 | 0.81 ± 0.19 | 6.72 ± 1.61 | 1.16 ± 0.05 | 9.57 ± 0.59 |
| | C | 31.7 ± 2.3 | 2.7 ± 1.3 | 9.0 | 0.14 ± 0.07 | 6.72 ± 1.61 | 0.32 ± 0.03 | 9.57 ± 0.59 |
| GR01 22 | E | 5.3 ± 0.1 | 11.1 ± 0.0 | 7.4 | 2.75 ± 0.60 | 15.59 ± 3.41 | 6.59 ± 0.11 | 37.35 ± 1.02 |
| | C | 30.2 ± 0.8 | 8.1 ± 0.3 | 7.4 | 1.75 ± 0.21 | 15.59 ± 3.41 | 2.14 ± 0.07 | 37.35 ± 1.02 |
| GR01 25 | C | 12.4 ± 0.2 | -3.0 ± 0.1 | -2.6 | 0.51 ± 0.04 | 6.79 ± 0.57 | 0.77 ± 0.01 | 10.17 ± 0.27 |
| GR01 26 | E | 3.6 ± 0.5 | -3.3 ± 0.2 | -3.0 | <0.15 | <1.33 | 0.46 ± 0.06 | 1.74 ± 0.33 |
| | C | 12.6 ± 1.4 | -3.4 ± 0.4 | -3.0 | 0.22 ± 0.05 | 1.33 ± 0.00 | 0.29 ± 0.05 | 1.74 ± 0.33 |
| GR01 27 | E | 7.1 ± 0.3 | -4.6 ± 0.1 | -3.7 | <0.14 | <2.52 | 0.78 ± 0.03 | 5.90 ± 0.37 |
| | C | 27.9 ± 1.3 | -6.0 ± 0.5 | -3.7 | 0.31 ± 0.04 | 2.52 ± 0.00 | 0.37 ± 0.03 | 5.90 ± 0.37 |
| GR01 28 | C | 24.8 ± 0.9 | -6.9 ± 0.4 | -3.8 | 0.25 ± 0.02 | 6.72 ± 0.66 | 0.29 ± 0.01 | 7.66 ± 0.36 |
| GR01 29 | C | 10.5 ± 0.5 | -3.8 ± 0.2 | -4.5 | <0.15 | <3.87 | 0.41 ± 0.02 | 4.54 ± 0.29 |
| GR01 30 | E | 8.8 ± 0.6 | -1.4 ± 0.2 | -5.0 | 0.36 ± 0.07 | 3.34 ± 0.73 | 0.44 ± 0.03 | 4.12 ± 0.39 |
| | C | 43.4 ± 1.9 | -1.5 ± 0.6 | -5.0 | 0.06 ± 0.03 | 3.34 ± 0.73 | 0.34 ± 0.02 | 4.12 ± 0.39 |
| GR01 31 | C | 34.5 ± 1.6 | 5.9 ± 0.7 | -4.7 | 0.13 ± 0.04 | 4.75 ± 1.65 | 0.32 ± 0.01 | 11.70 ± 0.74 |
| GR01 32 | C | 23.7 ± 1.6 | 3.2 ± 0.7 | -4.5 | 0.18 ± 0.04 | 4.57 ± 0.95 | 0.29 ± 0.02 | 7.24 ± 0.65 |
| GR01 34 | C | 28.5 ± 0.9 | 18.5 ± 0.4 | 19.0 | 0.22 ± 0.01 | 6.60 ± 0.45 | 0.24 ± 0.01 | 7.14 ± 0.30 |
| GR02 01 | E | 5.2 ± 0.6 | -3.1 ± 0.2 | -3.1 | <0.14 | <1.86 | 0.77 ± 0.07 | 4.25 ± 0.61 |
| GR02 02 | E | 6.3 ± 0.6 | -0.8 ± 0.2 | -1.5 | <0.16 | <2.52 | 0.46 ± 0.04 | 3.12 ± 0.40 |
| | C | 38.3 ± 5.9 | -3.3 ± 2.2 | -1.5 | <0.16 | <2.52 | 0.12 ± 0.02 | 3.12 ± 0.40 |
| GR02 07 | C | 18.0 ± 2.4 | 5.6 ± 1.0 | 7.4 | <0.15 | < 6.78 | 0.13 ± 0.02 | 2.57 ± 0.45 |
| GR02 10 | E | 9.8 ± 0.5 | -1.9 ± 0.2 | -4.7 | <0.16 | < 3.97 | 0.37 ± 0.01 | 3.80 ± 0.25 |
| | C | 51.7 ± 1.4 | 0.0 ± 0.5 | -4.7 | 0.19 ± 0.01 | 3.97 ± 0.00 | 0.28 ± 0.01 | 3.80 ± 0.25 |
| GR02 12 | C | 12.0 ± 0.8 | -7.5 ± 0.4 | -6.9 | 0.21 ± 0.09 | 2.67 ± 1.14 | 0.30 ± 0.02 | 3.82 ± 0.36 |
| GR02 13 | E | 6.0 ± 0.6 | -3.6 ± 0.2 | -6.1 | 0.26 ± 0.02 | 1.66 ± 0.23 | 0.21 ± 0.03 | 1.31 ± 0.24 |
| | C | 45.8 ± 2.5 | -7.1 ± 1.0 | -6.1 | 0.14 ± 0.01 | 1.66 ± 0.23 | 0.20 ± 0.01 | 1.31 ± 0.24 |
| GR04 02 | E | 5.6 ± 0.4 | 6.3 ± 0.2 | 6.2 | 0.09 ± 0.13 | 0.53 ± 0.76 | 0.47 ± 0.03 | 2.80 ± 0.26 |
| GR05 05 | E | 3.1 ± 0.5 | 6.9 ± 0.2 | 6.4 | <0.16 | <1.23 | 0.32 ± 0.04 | 1.04 ± 0.22 |
| | C | 51.7 ± 5.4 | 7.3 ± 2.2 | 6.4 | <0.16 | <1.23 | 0.12 ± 0.01 | 1.04 ± 0.22 |
| GR05 11 | E | 2.6 ± 1.6 | 7.7 ± 0.7 | 7.9 | 0.04 ± 0.18 | 0.12 ± 0.51 | 0.30 ± 0.16 | 0.82 ± 0.67 |
| GR10 01 | E | 9.9 ± 0.4 | 3.7 ± 0.1 | 2.0 | 0.32 ± 0.04 | 3.40 ± 0.44 | 0.45 ± 0.02 | 4.77 ± 0.26 |
| | C | 41.2 ± 2.0 | 5.1 ± 0.6 | 2.0 | 0.23 ± 0.02 | 3.40 ± 0.44 | 0.18 ± 0.01 | 4.77 ± 0.26 |
| GR10 02 | E | 4.6 ± 0.4 | 2.3 ± 0.1 | 2.5 | 0.87 ± 0.10 | 4.28 ± 0.58 | 0.88 ± 0.06 | 4.34 ± 0.45 |
| | C | 21.9 ± 2.8 | -1.2 ± 1.2 | 2.5 | <0.12 | <4.28 | 0.25 ± 0.04 | 4.34 ± 0.45 |

**Notes.** $^{(a)}$ The types of components are: C = cavity shock; E = envelope emission; S = spot shock; A = envelope absorption. $^{(b)}$ Integrated intensity of each velocity component approximated to the gaussian fit.

Table 5.24: Gaussian decomposition results for the Cygnus $^{13}$CO $J = 10$–9 data.

| Source | Comp.[a] | *FWHM* | $v_{\rm peak}$ | $v_{\rm LSR}$ | $^{13}$CO $J = 10$–9 | |
|---|---|---|---|---|---|---|
| | | | | | $T_{\rm MB}^{\rm peak}$ | $\int T_{\rm MB}\,{\rm d}v^b$ |
| | | (km s$^{-1}$) | (km s$^{-1}$) | (km s$^{-1}$) | (K) | (K km s$^{-1}$) |
| GR08 04 | E | 3.0 ± 0.7 | 5.4 ± 0.3 | 5.4 | 0.32 ± 0.06 | 1.03 ± 0.31 |
| GR06 02 | E | 3.0 ± 0.2 | -4.5 ± 0.1 | -4.5 | 1.07 ± 0.06 | 3.43 ± 0.31 |
| GR06 03 | E | 1.9 ± 0.0 | -3.2 ± 0.0 | -3.2 | 3.96 ± 0.08 | 8.14 ± 0.25 |
| GR03 02 | E | 1.8 ± 0.7 | 4.8 ± 0.3 | 4.8 | 0.26 ± 0.08 | 0.50 ± 0.24 |
| GR03 03 | E | 1.6 ± 0.6 | -0.5 ± 0.2 | -0.5 | 0.28 ± 0.09 | 0.47 ± 0.23 |
| GR03 04 | E | 1.2 ± 0.1 | 8.7 ± 0.0 | 8.7 | 1.84 ± 0.10 | 2.41 ± 0.20 |
| GR03 05 | E | 1.7 ± 0.1 | 11.4 ± 0.0 | 11.4 | 2.07 ± 0.08 | 3.78 ± 0.23 |
| GR01 02 | E | 3.7 ± 0.9 | 14.9 ± 0.4 | 14.9 | 0.28 ± 0.06 | 1.10 ± 0.34 |
| GR01 03 | E | 4.8 ± 1.0 | 14.2 ± 0.4 | 14.2 | 0.29 ± 0.05 | 1.47 ± 0.39 |
| GR01 04 | E | 3.9 ± 0.8 | 14.8 ± 0.3 | 14.8 | 0.31 ± 0.06 | 1.29 ± 0.35 |
| GR01 08 | E | 5.5 ± 1.1 | 15.2 ± 0.5 | 15.2 | 0.26 ± 0.05 | 1.55 ± 0.42 |
| GR01 09 | E | 1.3 ± 0.2 | 17.2 ± 0.1 | 17.2 | 0.79 ± 0.10 | 1.07 ± 0.20 |
| GR01 16 | E | 1.1 ± 0.2 | -2.1 ± 0.1 | -2.1 | 0.55 ± 0.10 | 0.67 ± 0.19 |
| GR01 21 | E | 4.1 ± 0.2 | 9.0 ± 0.1 | 9.0 | 1.16 ± 0.05 | 5.03 ± 0.36 |
| GR01 22 | C | 11.2 ± 0.2 | 7.4 ± 0.1 | 7.4 | 2.35 ± 0.09 | 28.18 ± 1.25 |
| | E | 4.1 ± 0.1 | 9.9 ± 0.0 | 7.4 | 6.92 ± 0.00 | 30.22 ± 0.64 |
| GR01 23 | E | 1.2 ± 0.2 | 11.7 ± 0.1 | 11.7 | 0.66 ± 0.10 | 0.83 ± 0.19 |
| GR01 25 | E | 5.0 ± 0.8 | -2.6 ± 0.3 | -2.6 | 0.35 ± 0.05 | 1.86 ± 0.40 |
| GR01 26 | E | 4.3 ± 0.2 | -3.0 ± 0.1 | -3.0 | 1.23 ± 0.05 | 5.63 ± 0.37 |
| GR01 27 | E | 2.5 ± 0.1 | -3.7 ± 0.0 | -3.7 | 2.28 ± 0.07 | 5.98 ± 0.28 |
| GR01 28 | C | 11.3 ± 3.7 | -3.8 ± 1.6 | -3.8 | 0.12 ± 0.03 | 1.40 ± 0.60 |
| GR01 29 | E | 4.1 ± 0.4 | -4.5 ± 0.2 | -4.5 | 0.70 ± 0.05 | 3.07 ± 0.36 |
| GR01 30 | C | 8.0 ± 4.3 | -5.0 ± 1.5 | -5.0 | 0.10 ± 0.06 | 0.85 ± 0.66 |
| | E | 1.0 ± 0.6 | -5.0 ± 0.2 | -5.0 | 0.30 ± 0.00 | 0.32 ± 0.24 |
| GR01 30 | E | 1.0 ± 0.6 | -5.0 ± 0.2 | -5.0 | 0.30 ± 0.00 | 0.32 ± 0.24 |
| GR01 31 | E | 2.0 ± 0.2 | -4.7 ± 0.1 | -4.7 | 0.94 ± 0.08 | 1.97 ± 0.25 |
| GR01 32 | E | 2.8 ± 0.9 | -4.5 ± 0.4 | -4.5 | 0.23 ± 0.07 | 0.70 ± 0.30 |
| GR02 01 | E | 3.5 ± 0.1 | -3.1 ± 0.0 | -3.1 | 2.52 ± 0.06 | 9.29 ± 0.33 |
| GR02 02 | E | 3.3 ± 0.2 | -1.5 ± 0.1 | -1.5 | 0.97 ± 0.06 | 3.36 ± 0.32 |
| GR02 03 | E | 1.8 ± 0.4 | -0.5 ± 0.2 | -0.5 | 0.47 ± 0.08 | 0.90 ± 0.24 |
| GR02 07 | E | 4.6 ± 2.2 | 7.4 ± 0.9 | 7.4 | 0.12 ± 0.05 | 0.61 ± 0.39 |
| GR02 08 | E | 1.2 ± 0.2 | -5.2 ± 0.1 | -5.2 | 0.76 ± 0.10 | 0.98 ± 0.20 |
| GR02 09 | E | 3.0 ± 1.3 | -5.1 ± 0.5 | -5.1 | 0.17 ± 0.06 | 0.55 ± 0.31 |
| GR02 10 | E | 4.7 ± 1.1 | -4.7 ± 0.5 | -4.7 | 0.25 ± 0.05 | 1.26 ± 0.39 |
| GR02 12 | E | 4.2 ± 1.1 | -6.9 ± 0.5 | -6.9 | 0.24 ± 0.05 | 1.09 ± 0.37 |
| GR02 13 | E | 5.9 ± 2.2 | -6.1 ± 0.9 | -6.1 | 0.14 ± 0.05 | 0.90 ± 0.44 |
| GR02 14 | E | 1.5 ± 0.7 | -5.2 ± 0.3 | -5.2 | 0.24 ± 0.09 | 0.37 ± 0.22 |
| GR04 01 | E | 1.5 ± 0.1 | 7.4 ± 0.0 | 7.4 | 1.45 ± 0.09 | 2.28 ± 0.22 |
| GR04 02 | E | 4.0 ± 0.6 | 6.2 ± 0.3 | 6.2 | 0.39 ± 0.06 | 1.66 ± 0.36 |
| GR05 05 | E | 2.1 ± 0.0 | 6.4 ± 0.0 | 6.4 | 3.70 ± 0.08 | 8.12 ± 0.26 |
| GR05 09 | E | 3.4 ± 1.9 | -0.2 ± 0.8 | -0.2 | 0.12 ± 0.06 | 0.44 ± 0.33 |
| GR05 11 | E | 2.2 ± 0.1 | 7.9 ± 0.0 | 7.9 | 2.93 ± 0.07 | 6.92 ± 0.27 |
| GR10 01 | E | 6.0 ± 1.7 | 2.0 ± 0.7 | 2.0 | 0.18 ± 0.04 | 1.15 ± 0.44 |
| GR10 02 | E | 3.8 ± 0.1 | 2.5 ± 0.0 | 2.5 | 2.77 ± 0.06 | 11.31 ± 0.35 |
| GR10 03 | E | 3.4 ± 1.8 | -1.1 ± 0.7 | -1.1 | 0.13 ± 0.06 | 0.48 ± 0.33 |
| GR10 05 | E | 1.2 ± 0.2 | -1.9 ± 0.1 | -1.9 | 0.60 ± 0.10 | 0.74 ± 0.19 |

**Notes.** $(^a)$ The types of components are: C = cavity shock; E = envelope emission; S = spot shock; A = envelope absorption. $(^b)$ Integrated intensity of each velocity component approximated to the gaussian fit.

Table 5.25: Gaussian decomposition results for the Cygnus $C^{18}O$ $J = 9$–8 data.

| Source | Comp.[a] | *FWHM* | $v_{peak}$ | $v_{LSR}$ | $C^{18}O$ $J = 9$–8 | |
|---|---|---|---|---|---|---|
| | | | | | $T_{MB}^{peak}$ | $\int T_{MB} dv^b$ |
| | | km s$^{-1}$ | km s$^{-1}$ | km s$^{-1}$ | (K) | K km s$^{-1}$ |
| GR06 03 | E | 2.2 ± 0.4 | -3.2 ± 0.2 | -3.2 | 0.45 ± 0.07 | 1.03 ± 0.26 |
| GR01 21 | E | 7.8 ± 1.9 | 9.2 ± 0.8 | 9.0 | 0.19 ± 0.04 | 1.55 ± 0.50 |
| GR01 22 | E | 4.6 ± 0.1 | 9.6 ± 0.0 | 7.4 | 2.37 ± 0.05 | 11.73 ± 0.39 |
| GR01 26 | E | 3.4 ± 1.0 | -3.5 ± 0.4 | -3.0 | 0.25 ± 0.06 | 0.89 ± 0.33 |
| GR01 27 | E | 1.8 ± 0.4 | -3.7 ± 0.2 | -3.7 | 0.41 ± 0.08 | 0.77 ± 0.24 |
| GR01 29 | E | 2.0 ± 0.8 | -4.3 ± 0.3 | -4.5 | 0.22 ± 0.08 | 0.46 ± 0.25 |
| GR02 01 | E | 3.6 ± 0.6 | -2.9 ± 0.3 | -3.1 | 0.39 ± 0.06 | 1.51 ± 0.34 |
| GR02 02 | E | 1.4 ± 0.7 | -1.9 ± 0.3 | -1.5 | 0.23 ± 0.09 | 0.34 ± 0.21 |
| GR05 05 | E | 2.7 ± 0.6 | 6.6 ± 0.3 | 6.4 | 0.33 ± 0.07 | 0.93 ± 0.29 |
| GR05 11 | E | 2.6 ± 0.9 | 7.9 ± 0.4 | 7.9 | 0.23 ± 0.07 | 0.66 ± 0.29 |
| GR10 02 | E | 3.9 ± 0.7 | 2.4 ± 0.3 | 2.5 | 0.37 ± 0.06 | 1.50 ± 0.35 |

**Notes.** $(^a)$ The types of components are: C = cavity shock; E = envelope emission; S = spot shock; A = envelope absorption. $(^b)$ Integrated intensity of each velocity component approximated to the gaussian fit.

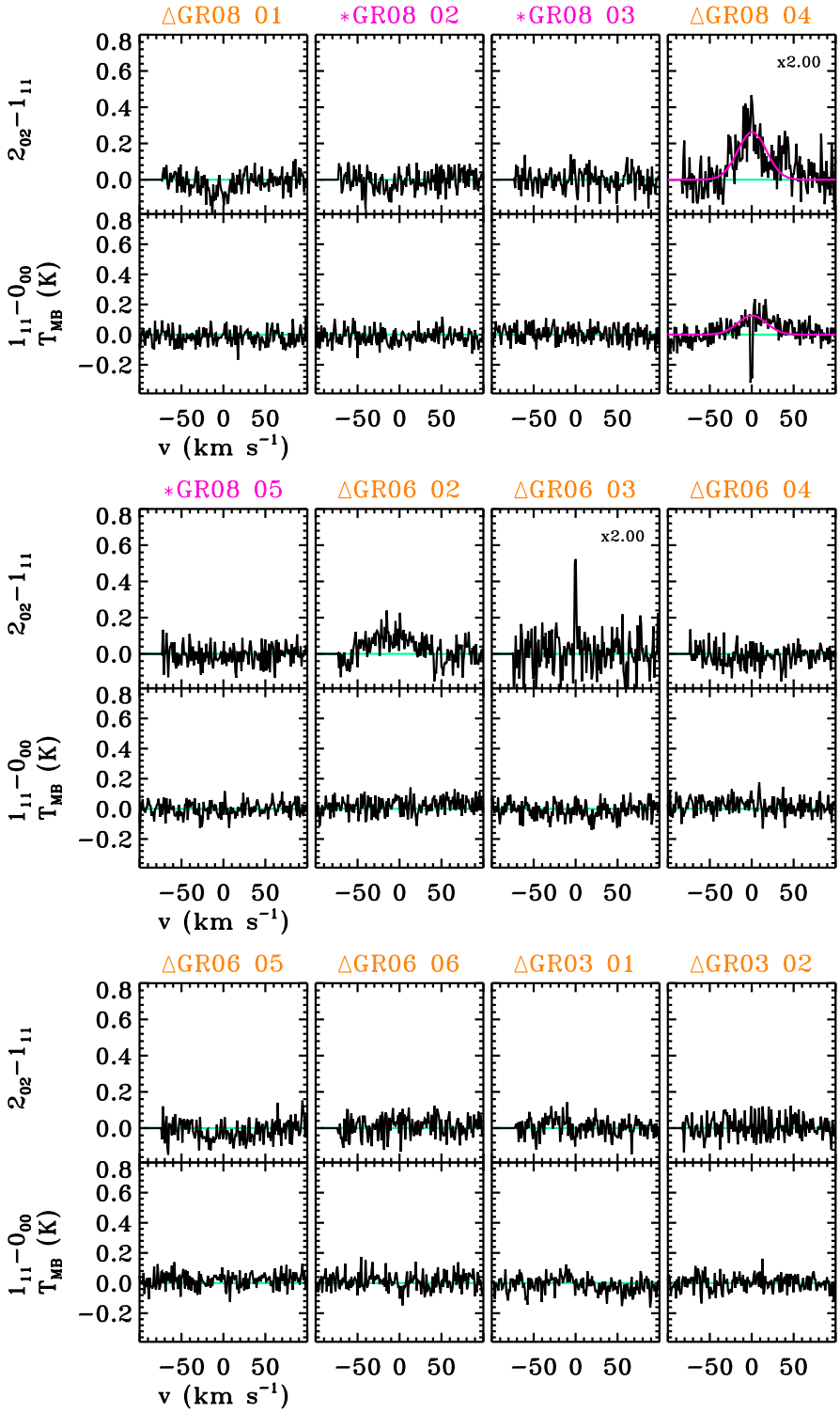


Figure 5.31: (*Bottom*) $H_2O$ $1_{11}$-$0_{00}$ (1113 GHz) and (*top*) $H_2O$ $2_{02}$-$1_{11}$ spectra observed for the Cygnus YSOs. The name of the Class 0 type sources is written in pink and with an asterisk symbol next to it and that of the Class I objects in orange with a triangle symbol. The baseline is plotted with a green line and the broad velocity component indicated in pink.

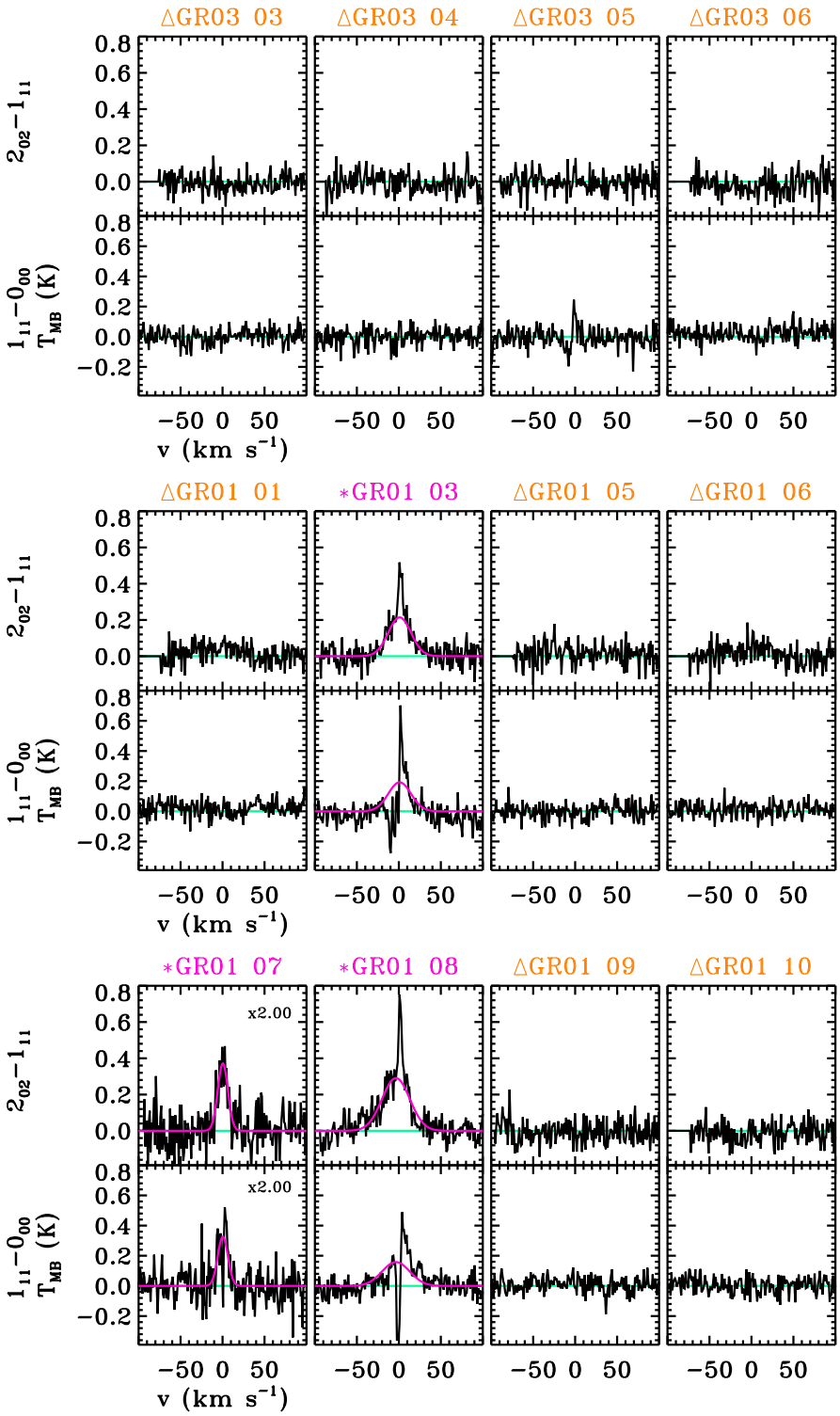


Figure 5.32: Same as Fig 5.31.

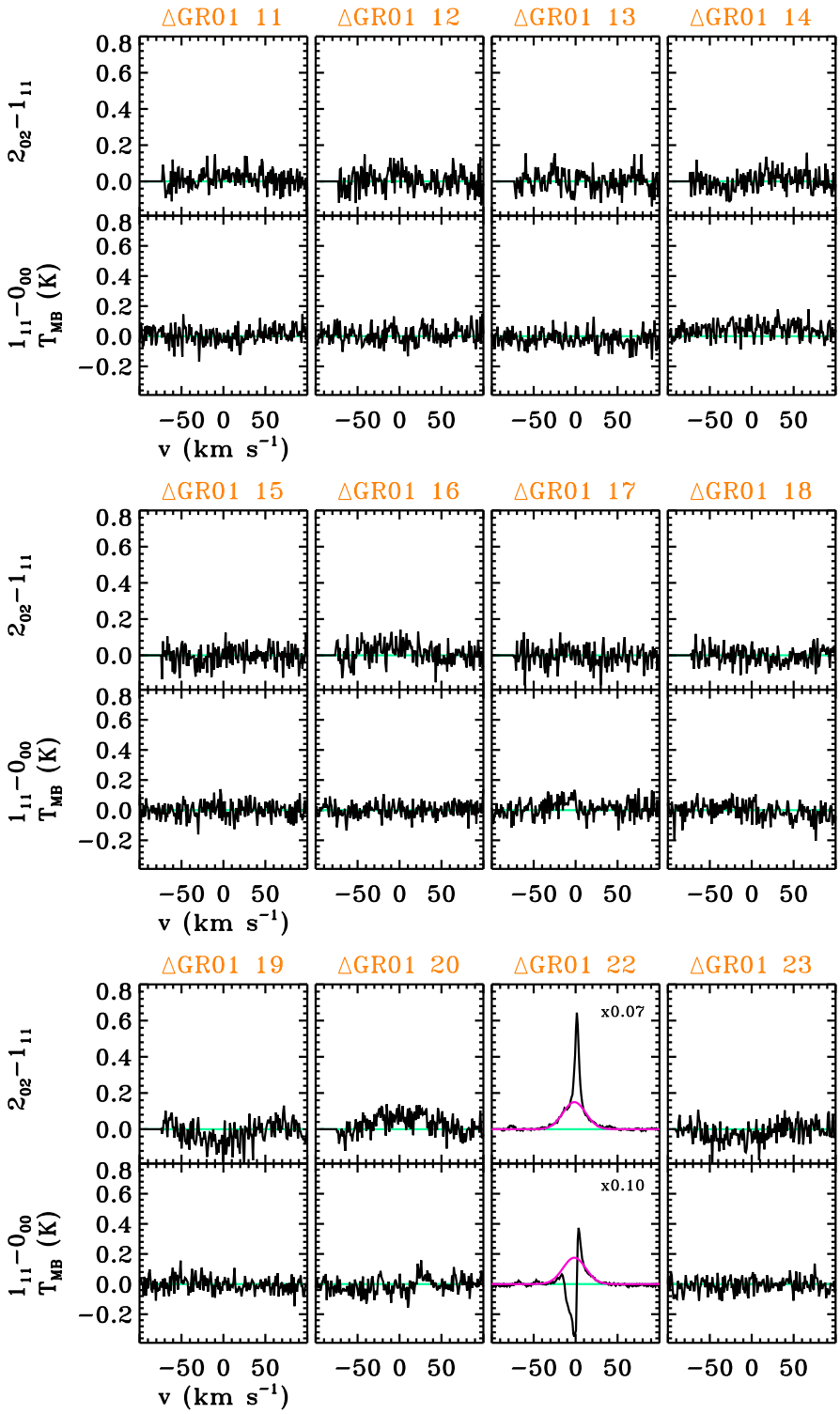


Figure 5.33: Same as Fig 5.31.

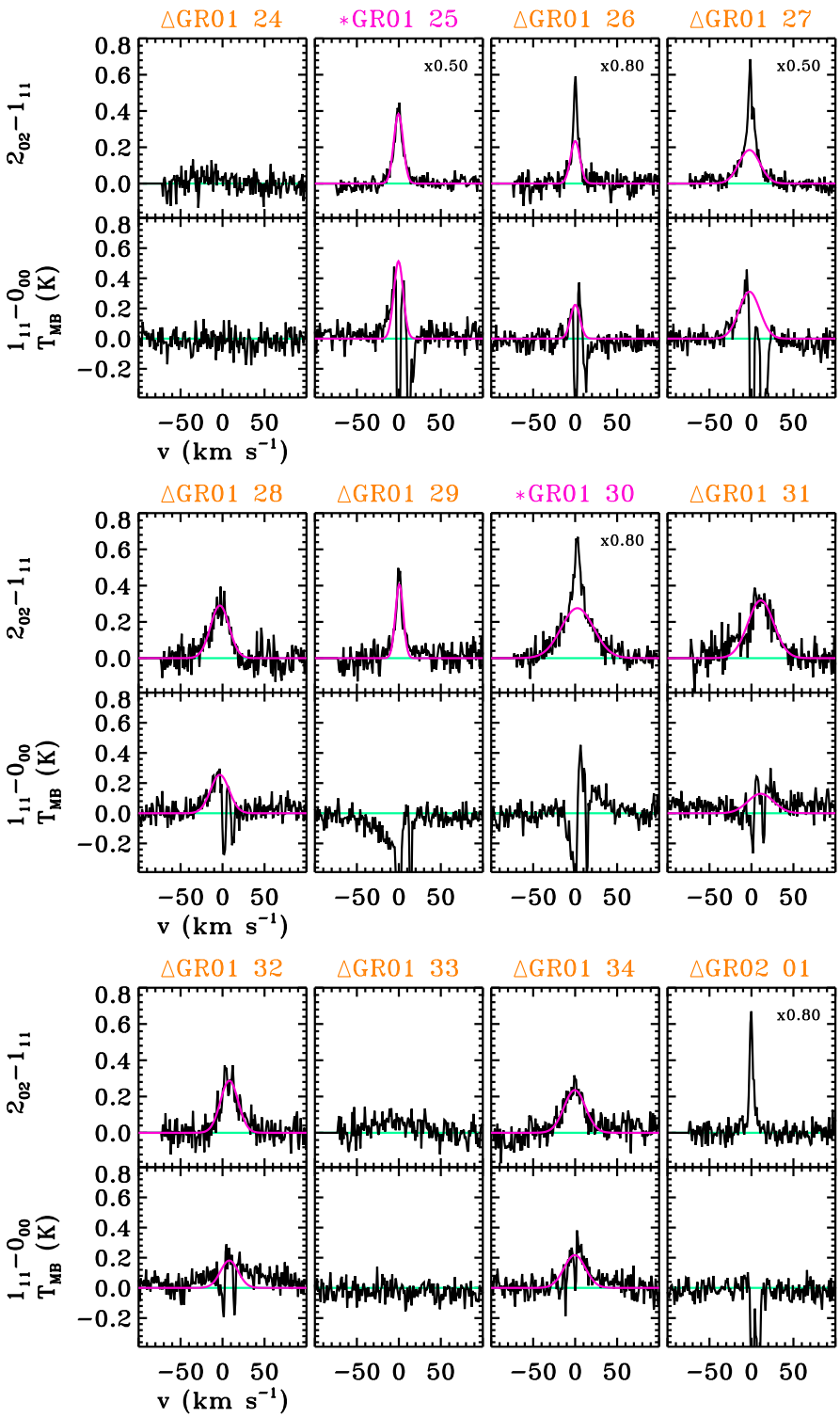


Figure 5.34: Same as Fig 5.31.

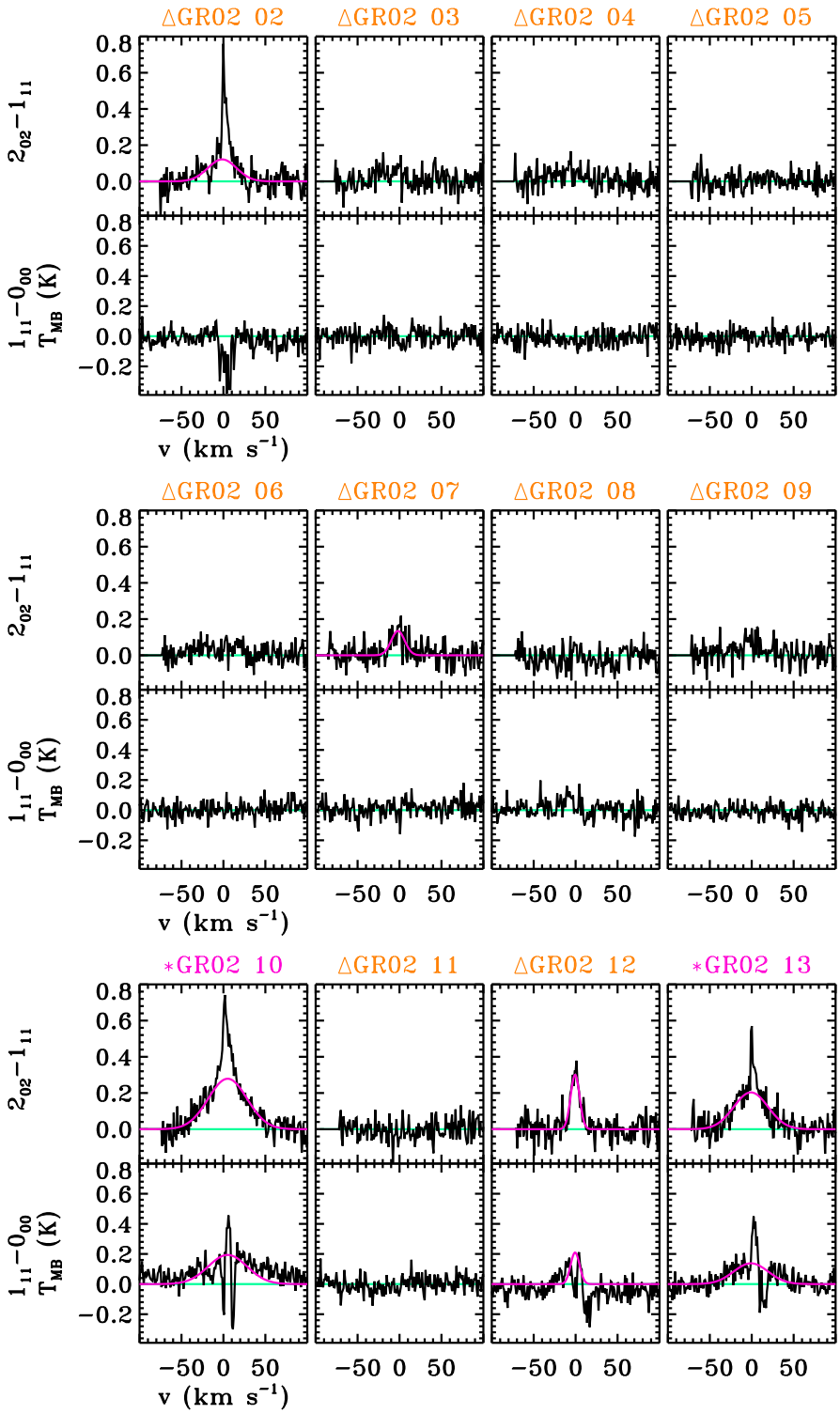


Figure 5.35: Same as Fig 5.31.

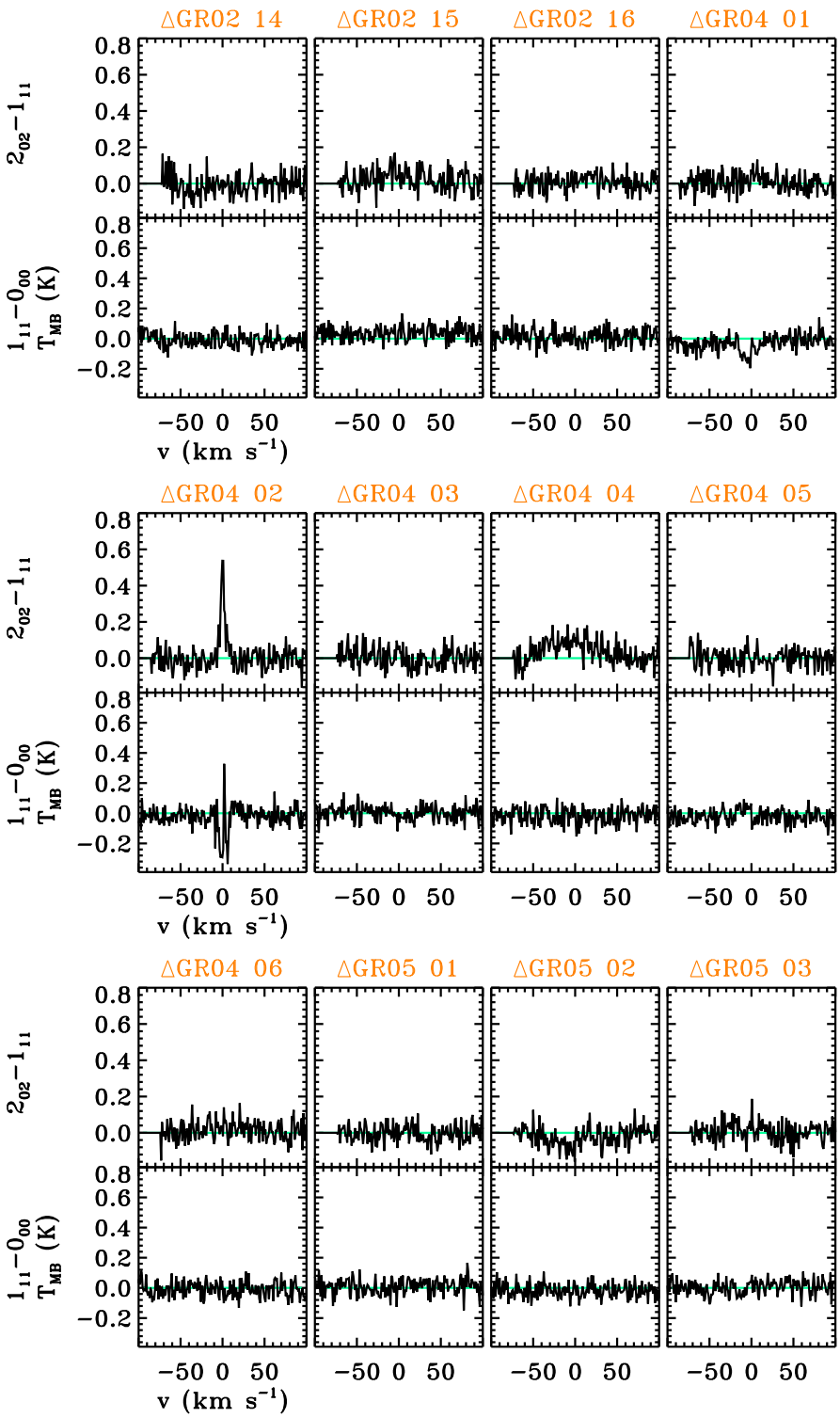


Figure 5.36: Same as Fig 5.31.

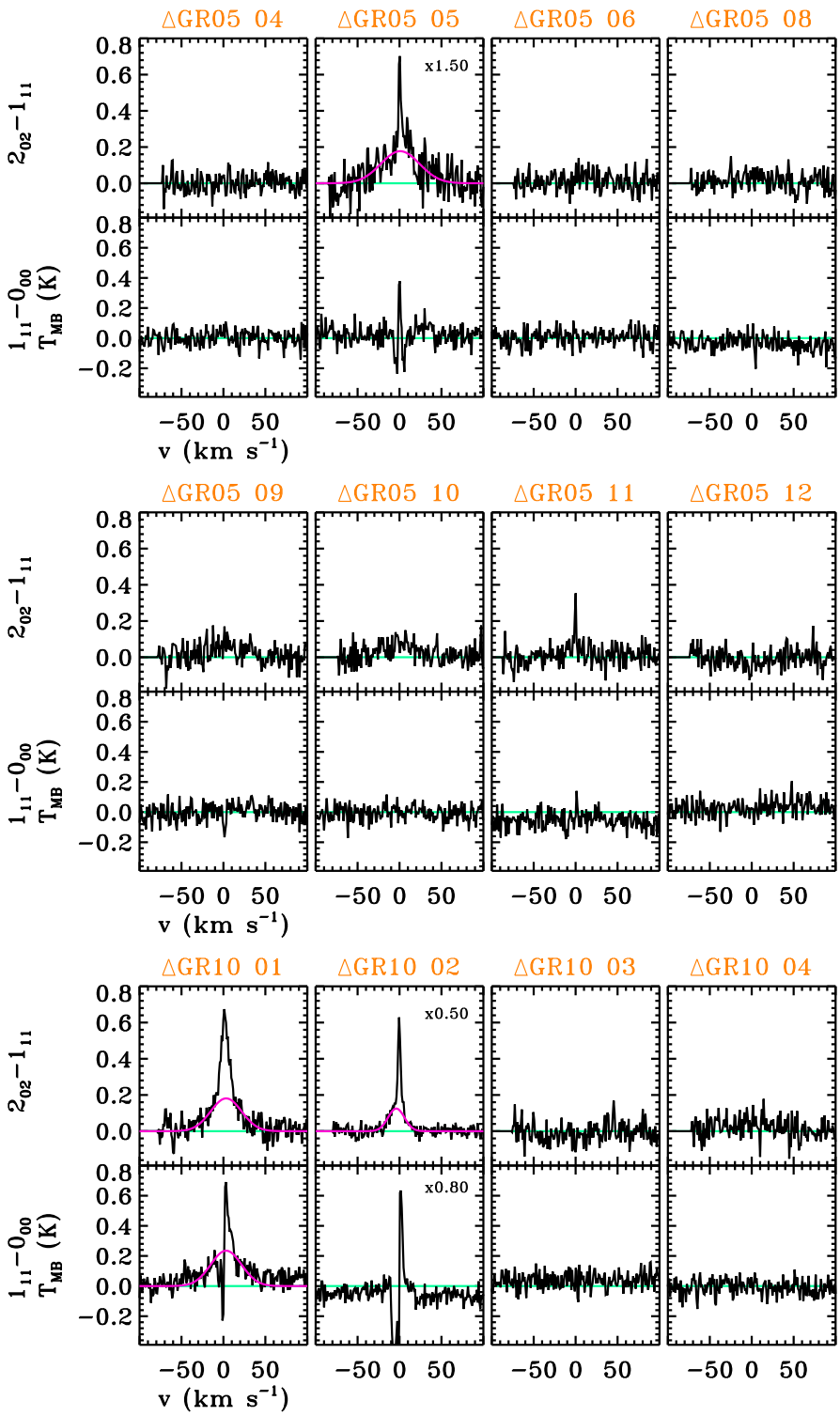


Figure 5.37: Same as Fig 5.31.

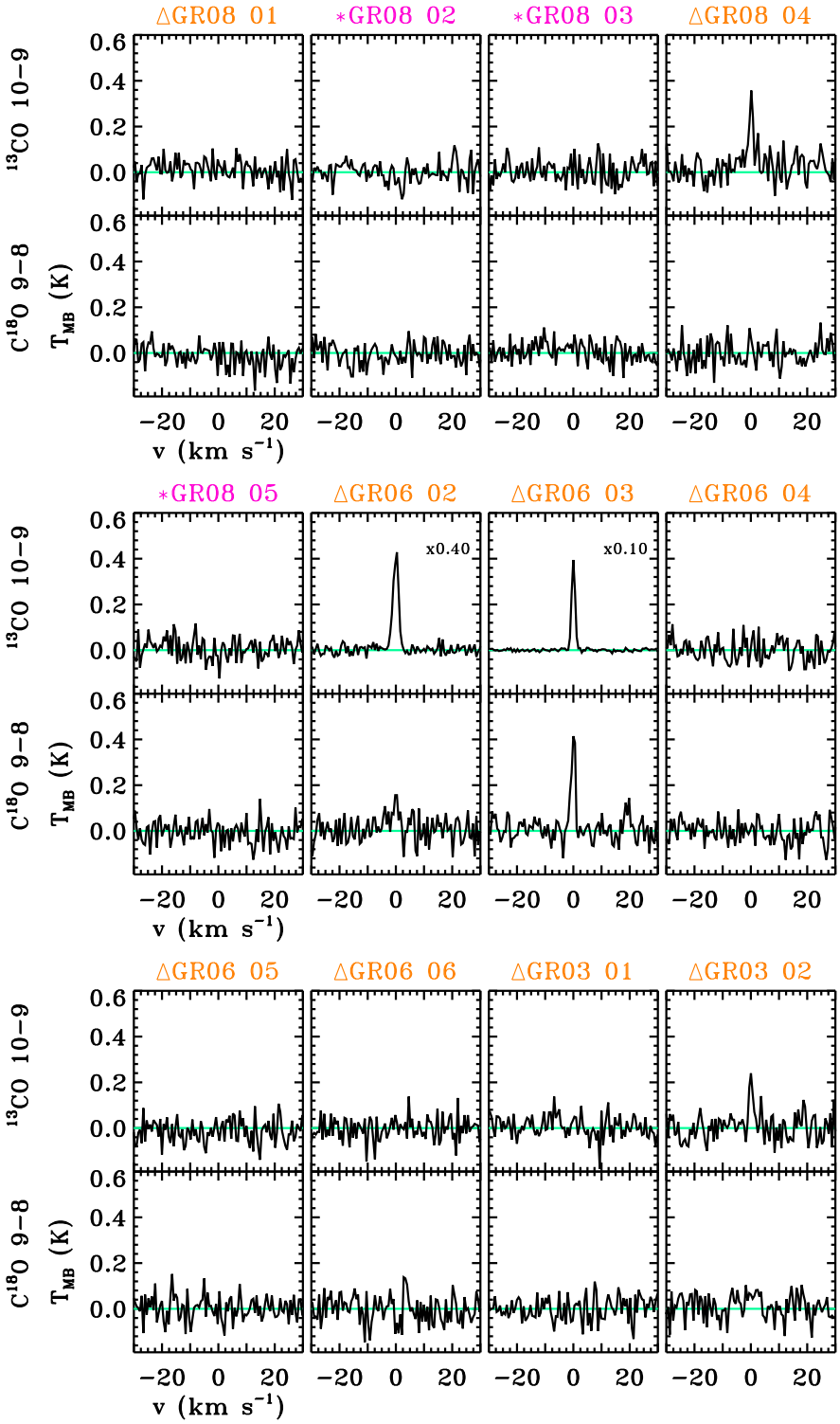


Figure 5.38: (*Bottom*) $C^{18}O$ $J = 9$–8 and (*top*) $^{13}CO$ $J = 10$–9 spectra observed for the Cygnus YSOs. The name of the Class 0 YSOs is written in pink (with an asterisk symbol next to it) and that of the Class I type objects in orange (and with a triangle symbol). The baseline is plotted with a green line and the broad velocity component indicated in pink.

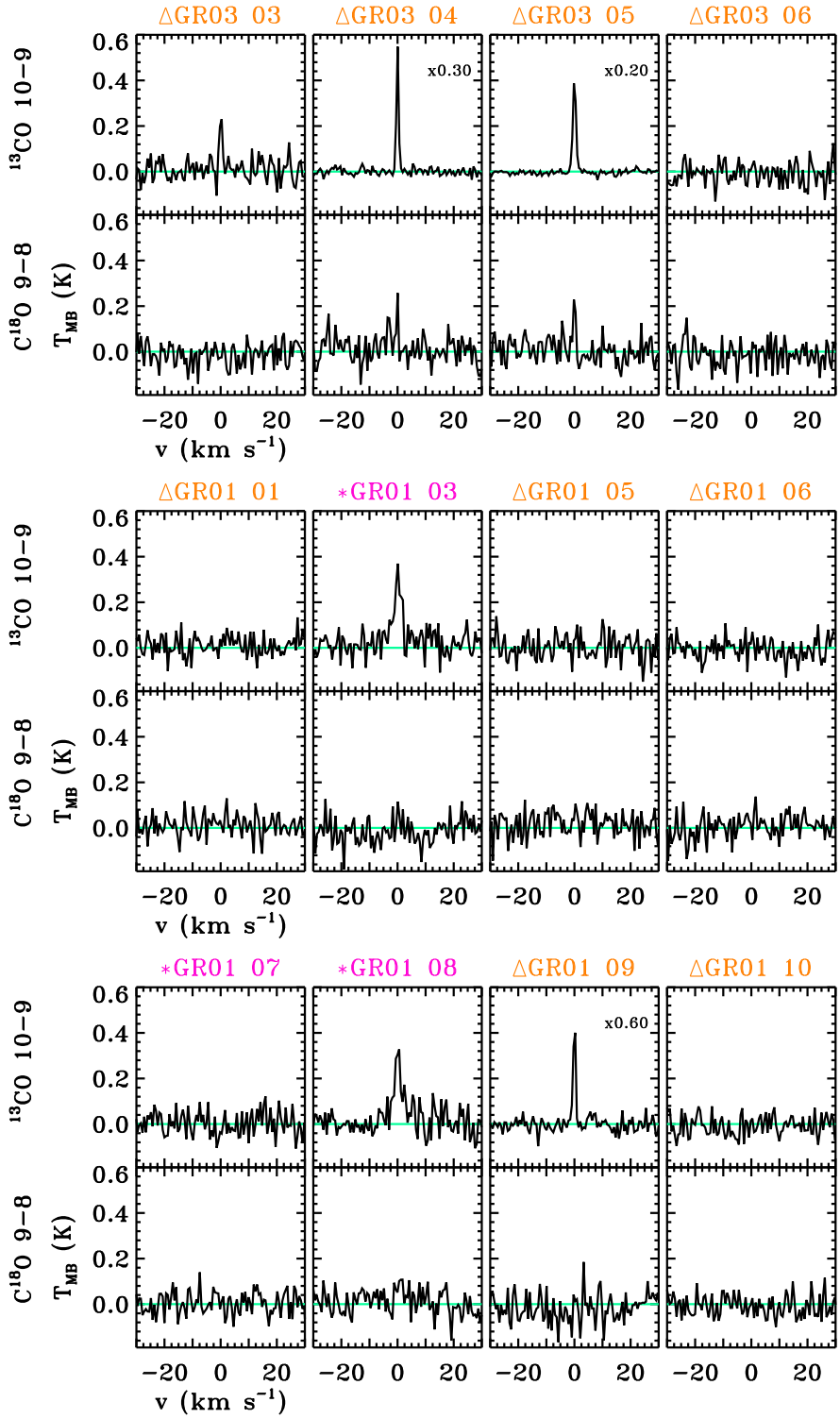


Figure 5.39: Same as Fig 5.38.

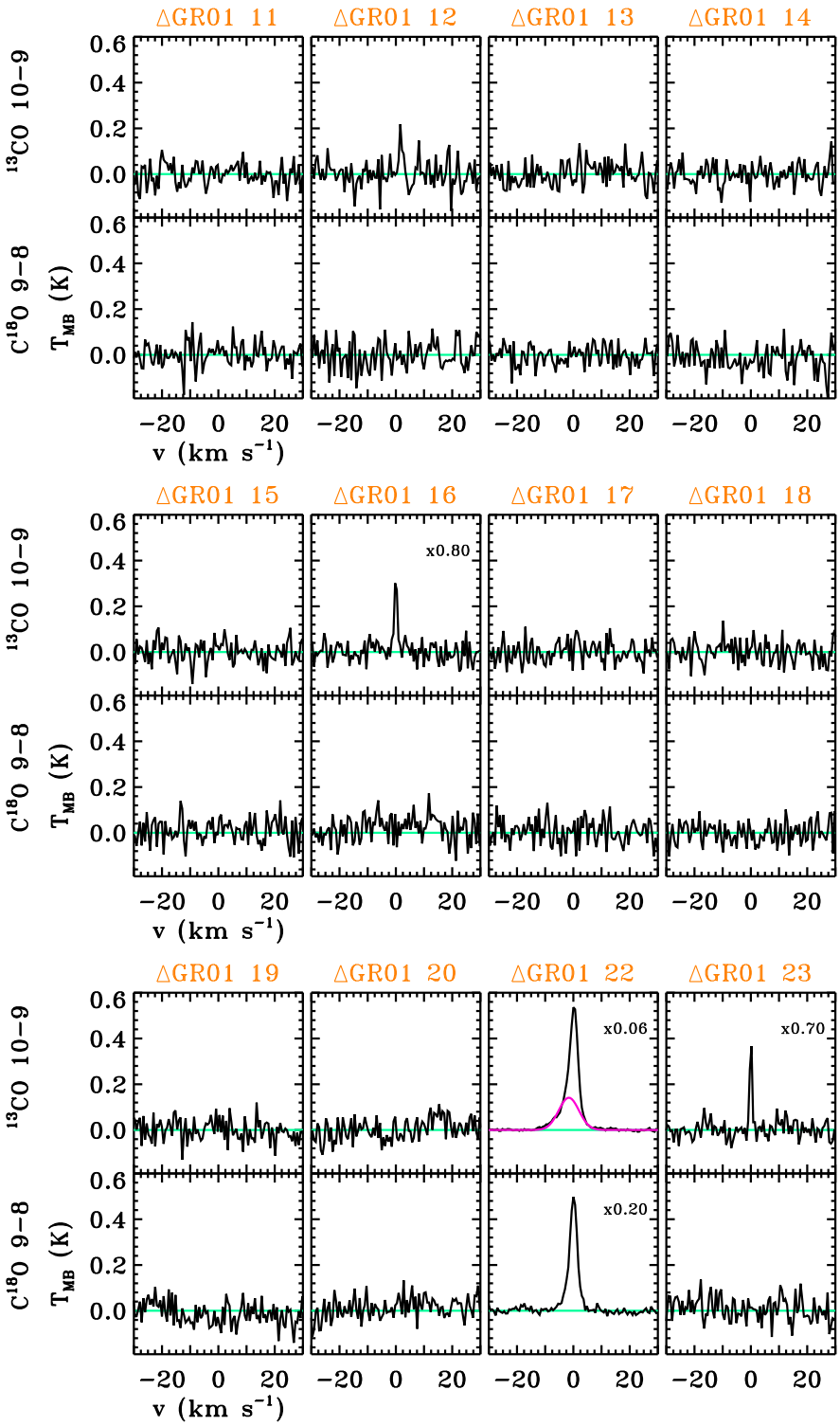


Figure 5.40: Same as Fig 5.38.

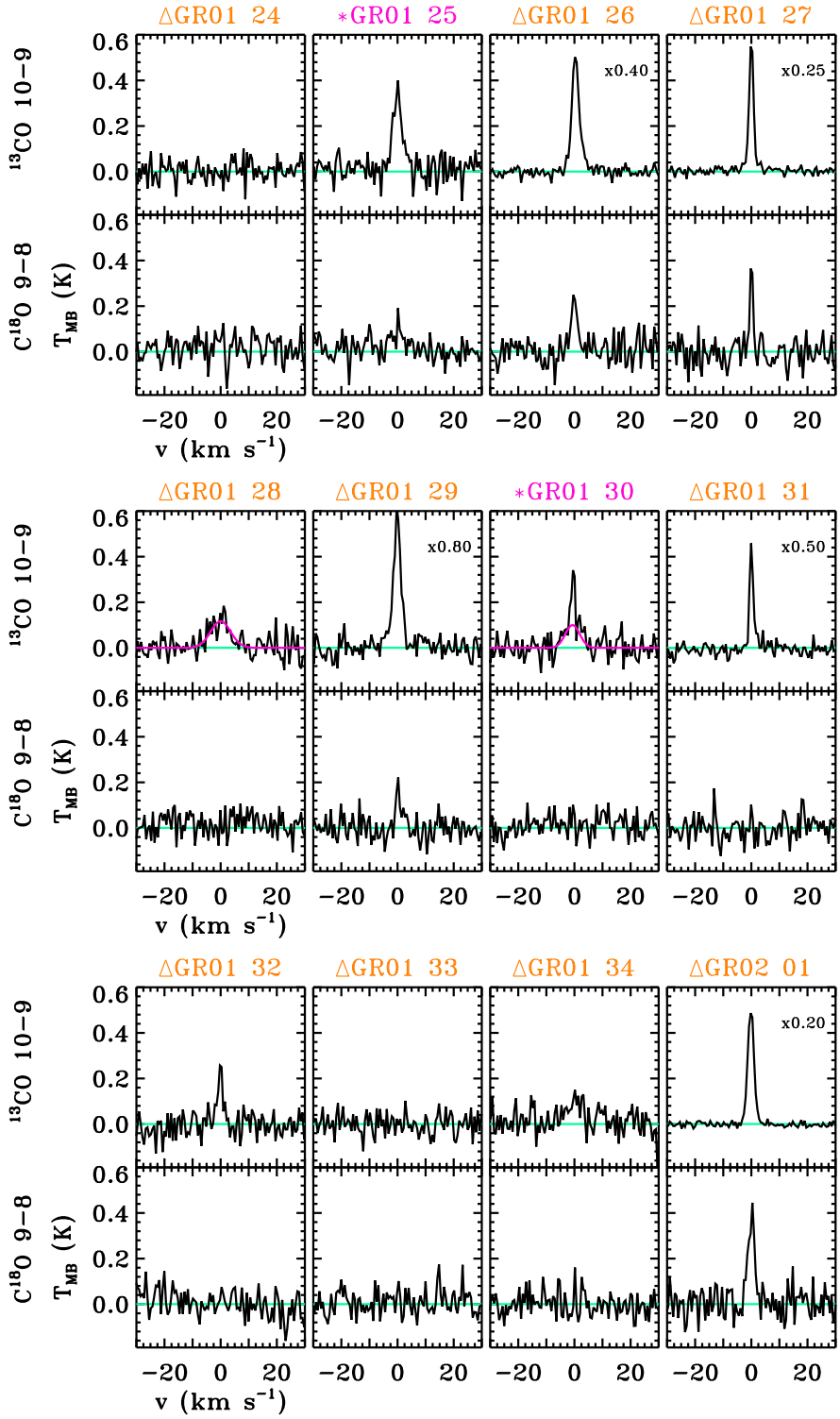


Figure 5.41: Same as Fig 5.38.

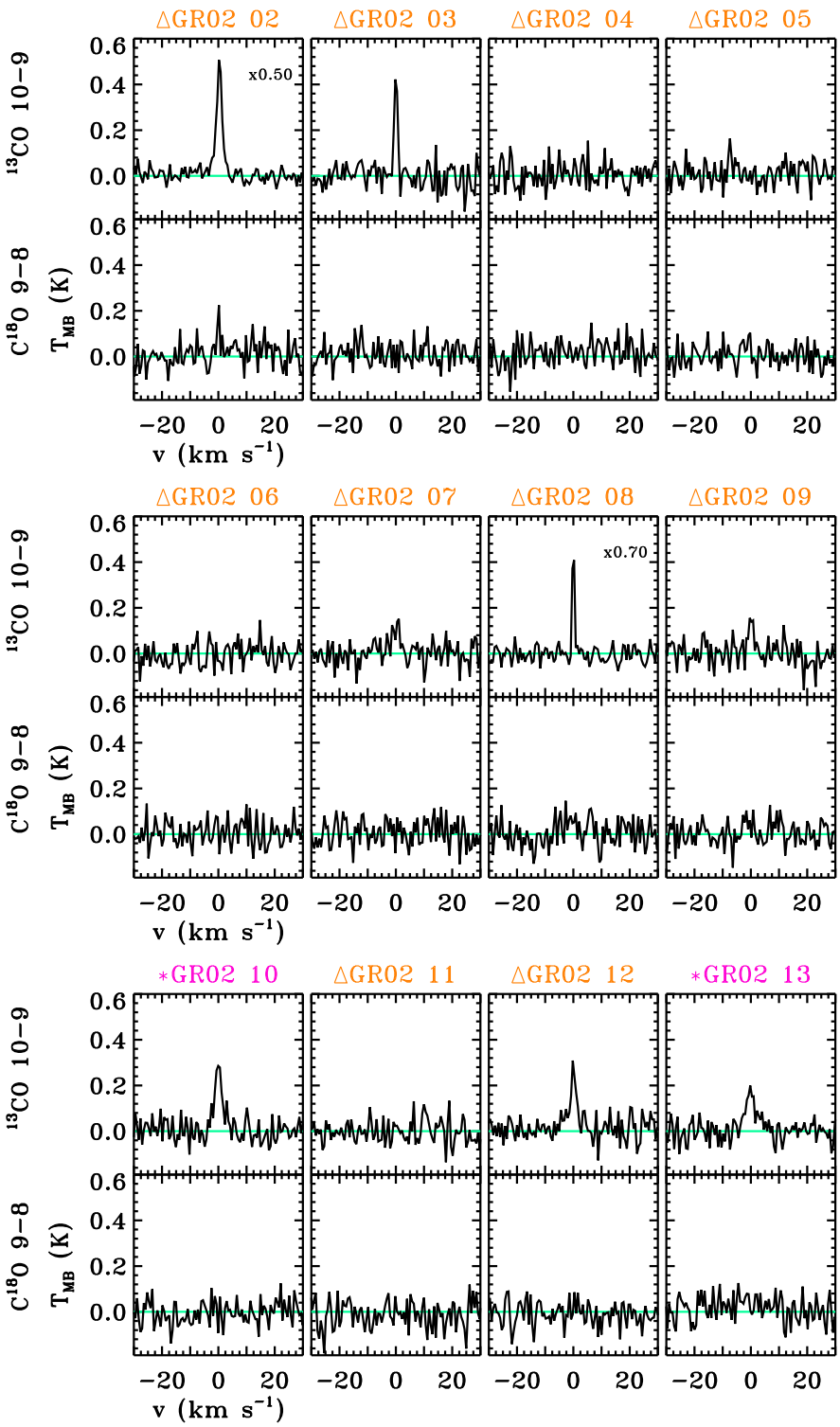


Figure 5.42: Same as Fig 5.38.

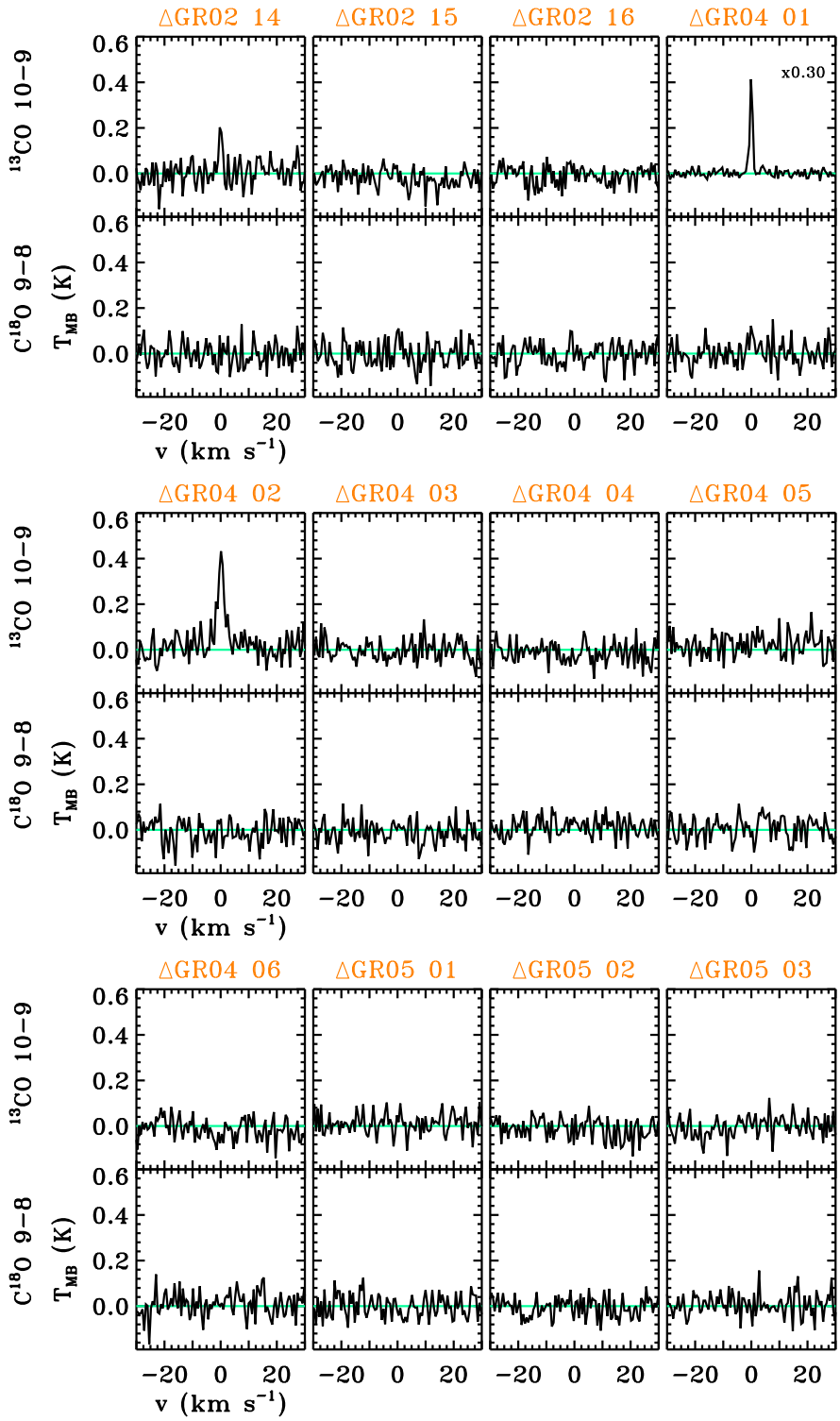


Figure 5.43: Same as Fig 5.38.

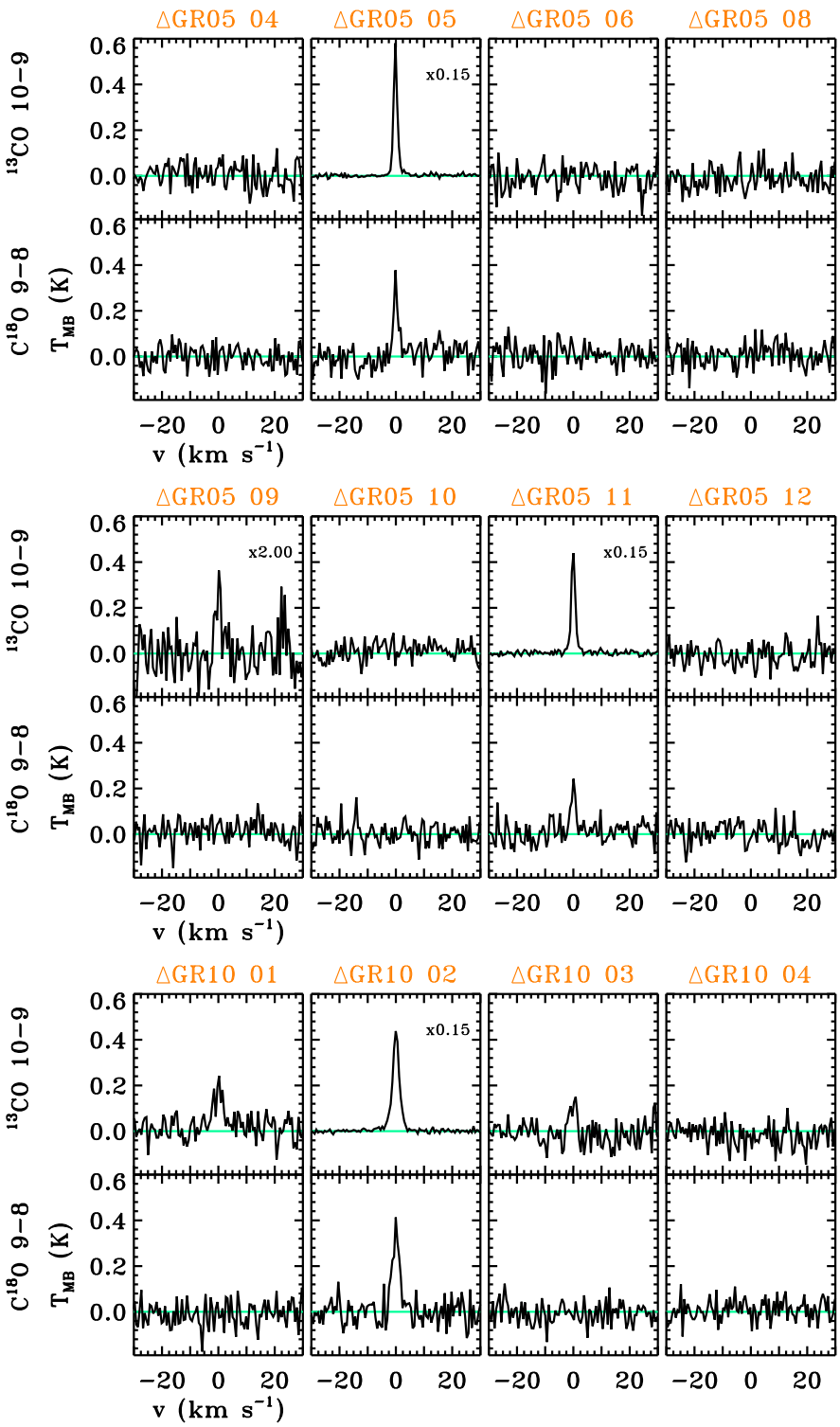


Figure 5.44: Same as Fig 5.38.